FAILURE BEHAVIOR OF UNDULATED SANDWICH PLATES UNDER OUT-OF-PLANE LOADING

by

Anıl Uzal

B.S., Mechanical Engineering, Istanbul Technical University, 2011

Submitted to the Institute for Graduate Studies in
Science and Engineering in partial fulfillment of
the requirements for the degree of
Master of Science

Graduate Program in Mechanical Engineering
Boğaziçi University

2014

ACKNOWLEDGEMENTS

I would like to express gratitude to my thesis advisor Prof. Fazıl Önder Sönmez and my thesis co-advisor Assoc. Prof. Nuri Ersoy for their guidance and helpfulness throughout my thesis study. Additionally, I would like to thank the research assistants Kenan Çınar and Fatih Öz for their support throughout the study, but especially for their great guidance and patience.

I would also like to thank my family for their invaluable support.

Finally, I would like to thank TUBITAK for supporting me financially throughout my thesis study.

ABSTRACT

FAILURE BEHAVIOR OF UNDULATED SANDWICH PLATES UNDER OUT-OF-PLANE LOADING

The goal of this thesis study is to understand the failure behavior of an undulated sandwich structure with a particular core design under out-of-plane loading conditions. For this purpose, three-point bending tests are performed. E-glass fiber-reinforced epoxy resin is selected as the material for both core and face sheets. Acoustic emission method is used to detect failure load levels. By carrying out fast Fourier transform technique, failure mechanism originated acoustic waves are investigated in frequency domain in order to identify activated failure modes. The mechanical properties of the composite material required for finite element calculations are obtained by conducting tension tests under real-time acoustic emission monitoring. Besides, theoretical calculations based on micromechanics are performed to determine composite properties and the values provided in the literature are also used. A finite element model of the sandwich structure with obtained mechanical properties is developed to predict the failure behavior and the analytical results are compared with the computational results. By following secant algorithm, critical load level is found. A promising agreement between the finite element model and the experimental results is observed. The successful correlation between the deflection and measured reaction force is obtained. The model succeeds to predict the region of failure accurately.

ÖZET

KIVRIMLI SANDVİÇ PLAKALARIN DÜZLEM DIŞI YÜKLEME KOŞULLARINDAKİ KIRILMA DAVRANIŞI

Bu tezin amacı, özgün bir kor dizaynına sahip bir kıvrımlı sandviç yapının düzlem dışı yükleme koşullarındaki kırılma davranışını anlamaktır. Bu amaçla, üç-nokta eğilme testleri gerçekleştirilmiştir. Gerek kor, gerekse yüzey plakaları için seçilen malzeme e-cam elyaf takviyeli epoksi reçinedir. Kırılma yükü seviyesi ve modlarını tespit etmek için akustik emisyon yöntemi kullanılmıştır. Aktif kırılma modlarını tanımlamak için hızlı Fourier dönüşümü tekniği ile kırılma mekanizması temelli akustik dalgalar frekans temelinde incelenmiştir. Sonlu elemanlar hesaplamaları için gerekli olan kompozit malzeme mekanik özellikleri, gerçek-zamanlı akustik emisyon görüntülemesi altında gerçekleştirilen çekme testleriyle elde edilmiştir. Bunun yanısıra, kompozit özelliklerini belirlemek için yapılan mikromekanik temelli teorik hesaplamalar ve literatürün sağladığı değerler de kullanılmıştır. Sandviç plakanın kırılma davranışını tahmin etmek üzere elde edilen mekanik özelliklere sahip bir sonlu elemanlar modeli geliştirilmiş, analitik sonuçlar numerik sonuçlarla karşılaştırılmıştır. Sekant algoritması kullanılarak kritik yük seviyesi bulunmuştur. Sonlu elemanlar yöntemiyle deneysel sonuçlar arasında başarılı bir uyum gözlenmiştir. Eğilme miktarıyla ölçülen reaksiyon kuvveti arasında başarılı bir korelasyon sağlanmıştır. Kırılma bölgesi, model tarafından isabetli bir şekilde tahmin edilmiştir.

TABLE OF CONTENTS

LIST OF FIGURES

LIST OF TABLES

LIST OF SYMBOLS

α	Tsai-Hill failure index
$[Q]$	Reduced stiffness matrix of the lamina
$[\bar{Q}]$	Transformed reduced stiffness matrix
$[A]$	Extensional stiffness matrix
$[B]$	Coupling stiffness matrix
$[D]$	Bending stiffness matrix
θ	The angular difference between the global *x*-direction and the fiber direction
N	Force per unit length
M	Moment per unite length
F_{1t}	Maximum allowable tensile stress in fiber direction
F_{2t}	Maximum allowable tensile stress in transverse direction
F_{1c}	Maximum allowable compressive stress
F_{2c}	Maximum allowable compressive stress in transverse direction
F_6	Maximum allowable shear stress
ε_{1t}^{u}	Ultimate allowable strain for tensile loading in fiber direction
ε_{1c}^{u}	Ultimate allowable strain for compressive loading in fiber direction
ε_{2t}^{u}	Ultimate allowable strain for tensile loading in transverse direction
ε_{2c}^{u}	Ultimate allowable strain for compressive loading in transverse direction
γ_6^u	Ultimate allowable shear strain

LIST OF ACRONYMS/ABBREVIATIONS

FRPC	Fiber-reinforced polymer composite
ASTM	American Society for Testing and Materials
AE	Acoustic emission
FFT	Fast Fourier transform
SEM	Scanning electron microscope
VIP	Vacuum infusion process
CNC	Computer numerical control
2D	Two dimensional
3D	Three dimensional
MPa	Mega Pascal
SP	Specimen
kN	Kilo Newton
dB	Decibel
kHz	Kilo Hertz
NLGEOM	Non-linear geometry
U	Deflection
VBRTM	Vacuum bag resin transfer molding
RIFT	Resin injection under flexible tooling
SCRIMP	Seemann composites resin infusion molding process
VARI	Vacuum assisted resin injection process

1. INTRODUCTION

For most of the high-technology applications, achieving an efficient structural construction is one of the major goals of the design stage. These constructions are required to be as light as possible and damage tolerant with maximized stiffness and strength properties [1]. Materials with only desired characteristics such as composites may fulfill these requirements.

Fiber-reinforced polymer composite (FRPC) materials are preferred in many industries. For decades, their relatively strong and stiff characteristics have been attracting the attention of designers. While aerospace industry is proving their effectiveness in the field of weight minimization and fuel consumption, maritime industry is showing how FRPCs decrease construction costs [2]. Thanks to their high capability of coping with extreme environments, reliability, maintainability, life cycle costs and service life extension, FRPCs are highly preferred for some daily life products to many high-technology applications. From lifeboats to ship hulls, tennis rackets to bicycles, formula one cars to planes, FRPCs are in the use [3]. For most of the FRPC applications, fibers are aligned to create a layer with a directional dependency at mechanical properties. By piling up these layers with different orientations, a designer can obtain a laminate to fulfill desired structural requirements [4].

The main advantage of FRPC compared to conventional materials and other composite structures is their versatility. When the continuous fibers are aligned in the same direction, the unidirectionality creates a transversely orthotropic layer, at which mechanical properties are direction dependent [5]. If two or more such layers are piled up in different orientations according to an external reference coordinate system, the laminate has different mechanical properties than the laminae have. Just by changing the orientation or the order of stacking, the designer can obtain a different material which acts differently. Properties of a laminated structure including strength, stiffness and fatigue behavior can be tuned to obtain desired response by choosing a proper lamination.

In some cases, the desired properties may be achieved by using monolithic composites while for some other applications, it is needed to improve the configuration of the structure further. That can be achieved by combining two different types of materials into a one discrete structure like hybrid or sandwich composite structures. The sandwich composites have a thick, lightweight core which is bonded to a pair of thin, stiff, and strong faces (skins) as shown in Figure 1.1 [2]. The face material usually has a high stiffness and strength, whereas the core is made of a lightweight material; it separates the faces and transfers loads from one face to the other, and it typically has sufficiently high compressive and shear strength [1]. An adhesive is used to join the core and the skins and it is capable of transmitting shear and transverse loads to and from the core. The empty volume in the core can be filled by foam for some applications, too.

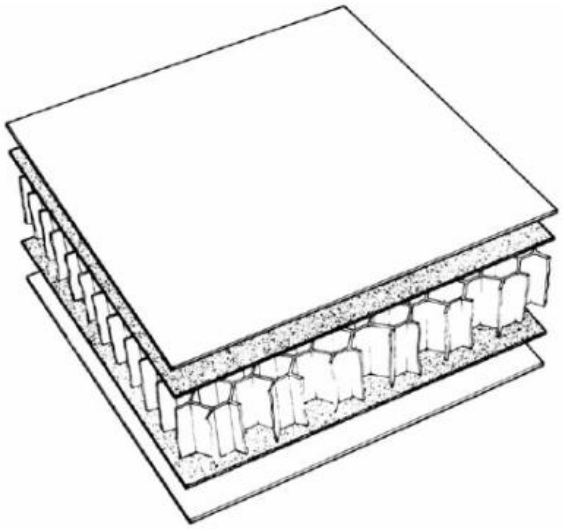

Figure 1.1. A sandwich structure with honeycomb core [2].

Sandwich composites exhibit high performance under bending and transverse loads as shown in Figure 1.2 [2]. The separation of face sheets increases the moment of inertia. In return to very little weight increases, bending stiffness and strength increase strikingly. As a result, sandwich structures are highly preferred for weight critical structural applications involving bending loads. It is also possible to obtain even more efficient structures by using laminated composites for face sheets [1]. Thanks to their well-improved mechanical characteristics, sandwich structures are very popular for high-technology applications ranging from aerospace industry to civil engineering, from ship

construction to racing cars, from lightening technologies to sport equipment. They can be seen in planes, trains, Formula 1 cars, satellites and so on [2].

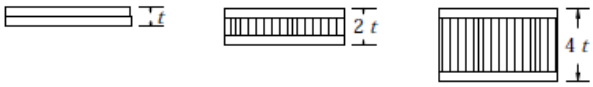

Relative Bending Stiffness	1	7.0	37
Relative Bending Strength	1	3.5	9.2
Relative Weight	1	1.03	1.06

Figure 1.2. Efficiency comparison of different structures [2].

1.1. Types of Sandwich Composites

Sandwich composites are manufactured by bonding thin and strong face sheets to both sides of a thick and light-weight core structure. There are various suitable materials for face sheets such as aluminum alloys or laminated composites in order to fulfill structural requirements [6]. However, the faces are always designed as sheets, independent of the material type. On the other hand, different structural designs can be adopted for core structures depending on the type of the application. Therefore, it is possible to classify sandwich composites according to their core.

Theoretically, the core of a sandwich composite can be made of any material and it can take any desired structural configuration. Nevertheless, they are mainly classified under four types: honeycomb core, corrugated core, solid or foam core and truss core [1]. Each structure possesses different mechanical and physical characteristics and mostly suitable for different types of application.

Honeycomb core is a three-dimensional structure which is made by nesting hexagonal cells together. The structure gets its name from their similar appearance to the natural honeycombs. The unit cell does not have to have the perfect form of a hexagon in order to mention the corresponding structure under this class. Honeycomb cores are usually more than ninety percent open space [6]. This makes honeycomb structures lightweight, good insulator and favorable for weight critical applications. They can

withstand bending loads successfully while in-plane shear loads and out-of-plane concentrated forces are undesired [7].

Similar to honeycomb structures, truss cores are made by nesting cells together in an order but in this case, a unit cell is an open cell. Figure 1.3a [8] shows a typical unit tetragonal cell. Forming a truss core structure is much easier than honeycomb structure and this flexibility makes truss cores favorable for complex and curved shapes.

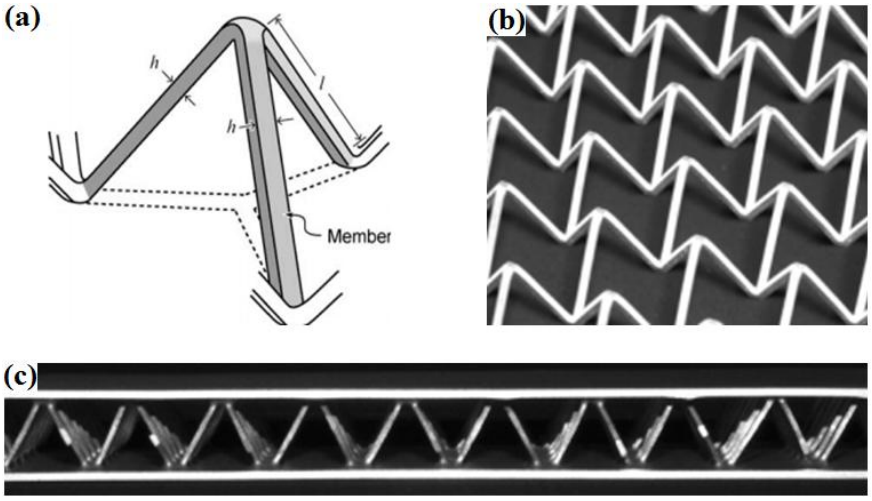

Figure 1.3. (a) The schematic representation of a tetragonal unit cell, the picture of (b) the manufactured core structure, and (c) the whole plate [8].

Corrugated cores resemble undulated sheets. When the structure is subjected to bending loads, it exhibits relatively high stiffness in one direction while pretty compliant in the perpendicular direction [1]. This core structure is very popular in maritime industry. One of the most common uses of corrugated sandwich structures in the daily life is cardboards. For the packaging industry, cardboards provide pretty low cost solutions [9].

Figure 1.4. An industrial example of corrugated sandwich plate [9].

As opposed to honeycomb, truss and corrugated core designs, foams do not have a definite geometric shape. By varying density, foam materials with a wide variety of physical and mechanical properties can be obtained [1].

In overall, the core material should have sufficient stiffness to prevent local buckling and sufficient strength to prevent damage. Lateral loads will create shear effects and core has to withstand it without the help of face sheets. In addition to mechanical demands, some thermal and chemical properties may be required such as corrosion resistance and low thermal conductivity [10].

1.2. The Literature Review

Researchers used experimental [11-45], numerical [12, 13, 16, 21, 25, 28-30, 32-34, 36-38, 41, 43-52], and analytical [13, 14, 18, 25, 26, 28, 30-33, 35-40, 42, 46-58] methods to investigate failure behavior of sandwich plates with honeycomb [11, 16-18, 21, 23, 26, 28, 29, 32, 38, 40, 41, 43-45, 48-51, 53, 58], corrugated [12, 59], foam [12, 13, 18-20, 22, 24, 27, 34-36, 42, 45, 52, 56], truss [14, 30, 31, 37, 57], and web [46] cores under static [13-40, 42, 43] and dynamic [17, 23, 25, 38-41, 44, 45, 49] loads.

Several failure modes have been investigated by the researches including core crushing [16, 17, 21, 23, 29, 32, 33, 37, 40, 43, 44, 51, 57], delamination [15, 19, 31, 54], face yielding [14, 18, 23, 40, 42], face wrinkling [14, 18, 23, 33, 35, 37, 43, 56], buckling [15, 22, 31, 37, 40, 47, 48, 54, 57], indentation [13, 14, 18, 20, 21, 23, 25, 26, 34-36, 38-41, 44, 49, 55, 56], face sheet-core debonding [15, 22, 47, 52], and core shear [14, 18, 19, 23-26, 30-32, 35, 37, 42, 51, 56, 57]. In order to investigate the failure modes, different loading conditions are configured for the simulations and experiments. For this purpose, three-point bending tests [11, 12, 14, 15, 18-20, 23-26, 28, 30, 34, 35, 40, 42-44, 56, 57], four-point bending test [18, 33, 46, 56], in-plane compression tests [15-18, 22, 37, 47, 48, 54], flatwise compression tests [15, 21, 29, 32], high-velocity impact tests [17, 23, 25, 45, 49], low-velocity impact tests [35, 38-41, 44], and indentation tests [13, 14, 18, 20, 21, 23, 25, 26, 34-36, 49, 55, 56] are conducted. Some researchers [24, 26, 33, 37, 40, 45, 49, 57] propose methods to predict failure and its mode.

1.3. The New Core Design

In this thesis study, a new core design is introduced. Figure 1.5 depicts the geometry of the core. It is composed of composite layers. The disadvantage of this type of a sandwich structure in comparison to honeycomb and foam core sandwiches is its cost. On the other hand, in the presence of transverse concentrated or distributed loads and shear loading, it is expected to show superior performance. As opposed to corrugated ones, it provides high bending stiffness and strength in all directions.

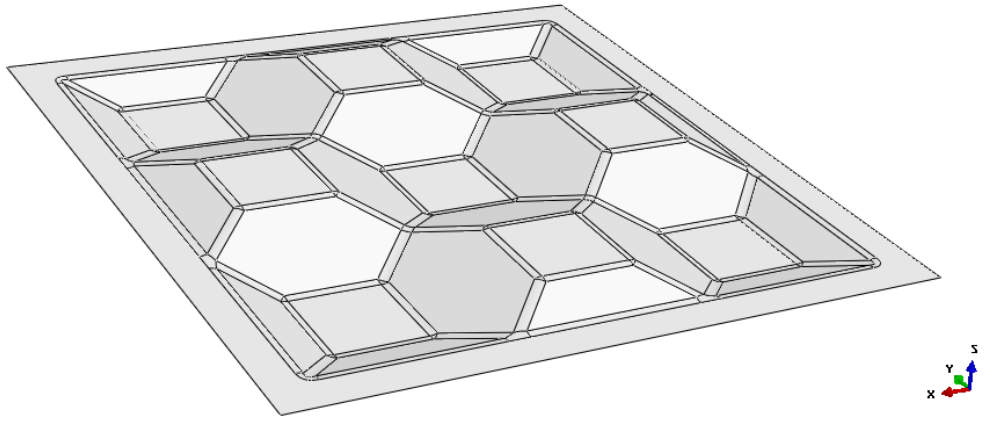

Figure 1.5. The schematic representation of introduced core design.

In order to design this particular core shape, several geometrical parameters have to be specified in the first place. The size of the unit cell, the core depth, and the wall angle determine the geometry of the core. The size of the top and the bottom areas where the top face and the bottom face are attached is mathematically a function of these three parameters, and they are important design parameters as well. Increase in these contact areas with the face sheets may improve the flexural strength at the expense of manufacturing difficulty. Increasing the core depth, while keeping the wall angle the same, improves flexural stiffness and strength due to the increase in the moment of inertia. It is possible to obtain numerous geometrical configurations by changing the size of unit cell, the wall angle and the core depth. The designer should consider the expected loading conditions and accordingly choose suitable values for the design variables. In addition to the geometrical parameters, the material parameters may also affect the mechanical behavior of the structure. In this thesis study, E-glass-fiber reinforced epoxy resin is the

selected material for both the core and the faces; but other types of materials can be used. The stacking sequences, the angular orientations of the laminae, volumetric fractions of the reinforcement and the matrix materials are also significant design parameters that change the mechanical response of the structure.

The major advantage of this particular core design is its versatility. It is possible to improve in-plane shear strength or bending stiffness by changing the design parameters. Unlike honeycomb cores, it can resist in-plane shear forces thanks to the angulated side faces and large contact surfaces. Its FRP structure enables the designer to arrange the mechanical response of the sandwich structure by changing the angular orientations of laminae and stacking sequences. Another important advantage is the low cost of the raw materials. Both E-glass cloth and epoxy resin are relatively inexpensive materials compared to the other materials used in the composite industry. The space may also be filled with foam to be improved some physical properties in order to use in specific applications.

1.4. Scope of the Thesis

The goal of this study is to develop an understanding of the failure behavior of undulated sandwich composites with a special core design under out-of-plane loading conditions and develop a parametric finite element model in order to predict failure.

In this thesis study, firstly, mechanical properties of E-glass-fiber / epoxy-resin composite materials are investigated. For this purpose, laminates with cross-ply and quasi-isotropic stacking sequences are manufactured by vacuum infusion process. Specimens are prepared from these laminates and tested according to ASTM D3039 test standard. Tension tests are performed under real-time acoustic emission monitoring (AE) in order to understand the activated failure mechanisms.

Secondly, the failure behavior of the sandwich structure is investigated via three-point bending tests under real-time acoustic emission monitoring. For the face sheets and the core, E-glass-fiber / epoxy-resin laminates with quasi-isotropic stacking sequence is selected. Machined and coated RenShape® Modeling Board is used as mold in order to the

give the three-dimensional form to the laminate under vacuum infusion process. The geometry of the mold is unique and not similar to any types of core structures reported in the literature and used in practice. The elements of the sandwich structure are bonded to each other by using an epoxy-based adhesive.

Thirdly, a finite element model for the sandwich structure is developed in ABAQUS by Python Scripting in order to predict the initial failure load under three point bending.

The motivation for this study is to broaden the understanding of the failure mechanisms in laminated composites and sandwich structures. These materials and structures exhibit superior characteristics and it is possible to create a pattern or structure in a manner that will tailor the structure to sustain subjected loads efficiently. They are mostly preferred in high-technology applications and are expected to take critical roles. Their failure in-service may cause catastrophic consequences. Therefore, understanding of how and when the failure occurs is essential for the designers in order to design a reliable and safe structure.

2. THEORETICAL BACKGROUND

E-glass fiber reinforced epoxy resin is selected as the material for both core and facesheets. Continuous fibers are gathered together in bundles and these bundles are placed next to each other to create a unidirectional ply. By piling up these unidirectional plies with different orientations, different roll layups such as cross-ply or quasi-isotropic layups can be obtained. Once the mechanical properties of E-glass and the final resin mixture are found, it is possible to determine the mechanical response via classical lamination theory. However, some theoretical assumptions may influence the accuracy of theoretical results. In addition to that, the mechanical behavior of the final product may differ due to the effects of vacuum infusion process. Air bubbles which are invisible to naked eye may become entrapped in the final part and decrease the strength of the part. Foreign substances may be entrapped since the manufacturing procedure is not held in a "clean room". Therefore, several parameters may influence the mechanical response of the laminated composites.

The mechanical behavior of a ply is formulated by its longitudinal Young's Modulus, transverse Young's Modulus, Shear Modulus, Poisson's Ratio, longitudinal tensile and compressive strengths, transverse tensile and compressive strengths and shear strength. It is possible to find each property by performing different tests on a unidirectional lamina. However, in the case of this study, it is highly impractical due to two main reasons: Firstly, it is not possible to find a unidirectional fiber roll in industry to prepare specimen. Secondly, each test requires different testing equipment with different fixtures. Therefore, theoretical calculations based on micromechanics are performed to determine composite properties; but the values provided in literature and tensile test results under acoustic emission monitoring are also used.

Although the material constants are sufficient to determine overall mechanical response of laminated structures, they do not reveal important failure mechanisms which cause fracture. Fiber reinforced composite structures have several failure mechanisms when they are subjected to loads. If the load is high enough, these mechanisms can cause progressive damage which may lead to catastrophic failure. These failure mechanisms may

occur in an order or simultaneously and because of the complexity of fiber reinforced composite structures, it is not easy to predict failure behavior accurately. Most of the studies in this field are focused on initiation and evolution of these failure modes under two-dimensional state of stress and limited to simple geometry and loading conditions. However, actual stress state is three dimensional and damage modes can easily interact with each other. In order to predict the failure behavior accurately, the structure has to be modeled accurately, including voids and impurities, and both in-plane and interlaminar stress components has to be taken into consideration. The amount of work to obtain such model is extremely high and therefore, initial failures of the structures are in the focus of this thesis study.

2.1. Important Failure Mechanisms for Laminated Composites:

For the fiber reinforced composites, the in-plane damage mechanisms which are commonly seen during various loading conditions are matrix cracking, interfacial debonding, fiber pull-out, fiber breakage and fiber kinking [60]. Unlike metal structures, failure and fracture progression is controlled by matrix micro cracks instead of a single macroscopic crack.

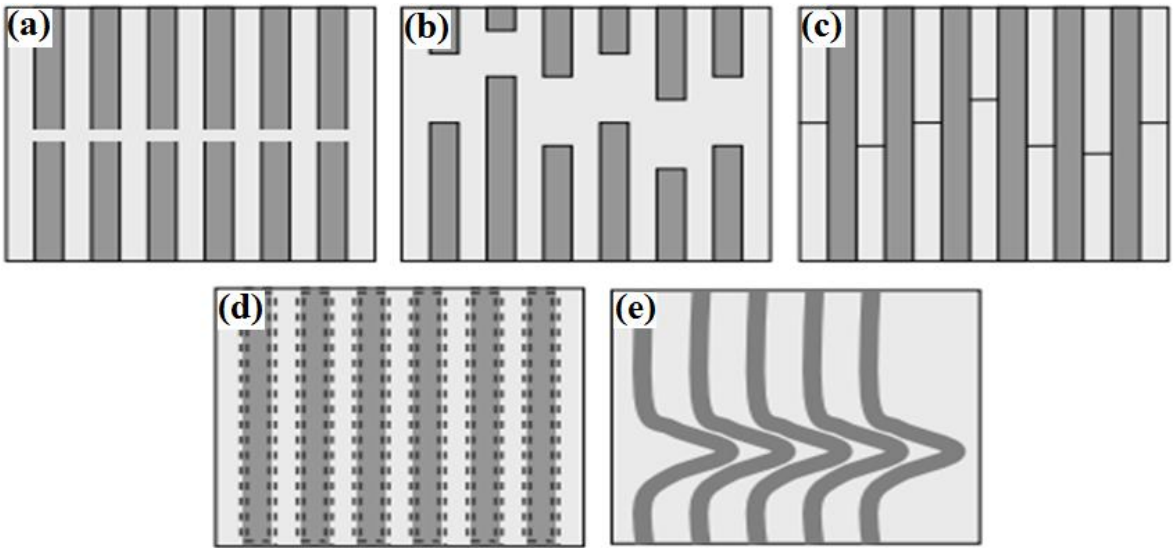

Figure 2.1. The schematic representation of different in-plane failure mechanisms at fiber reinforced composite laminates, (a) fiber fracture, (b) fiber pullout, (c) matrix cracking, (d) fiber matrix debonding, and (e) fiber kinking [60].

Besides, delamination is a commonly seen interlaminar damage mechanism [60].

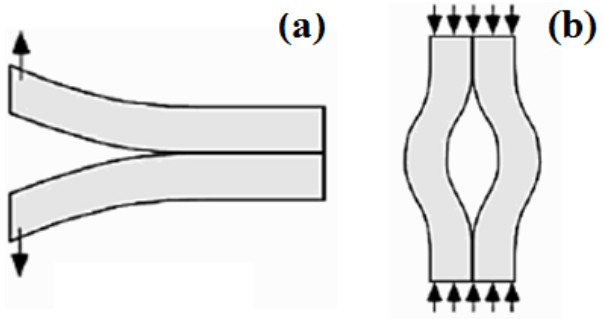

Figure 2.2. Schematic representation of different interlaminar failure mechanisms at fiber reinforced composite laminates: (a) Delamination and (b) buckling [60].

Matrix cracking is the most common failure mode since matrix material is much weaker than fiber material [3]. If transverse loading is applied to a unidirectional lamina, the matrix has to withstand it individually and the amount of matrix cracks increases rapidly.

When the matrix solidifies, fibers and matrix are bonded to each other and share an interface. When the structure starts to deform, the mismatch between material properties may lead to debonding at that interface. As a result, matrix can no more support the fibers in the region where debonding occurs. After matrix cracking, it is the second most commonly seen failure modes for fiber reinforced composites. Since weak bonding between matrix and fibers causes debonding and fibers are no more supported in that region, fibers can be now pulled out of matrix. Debonding and fiber pull-out occur at the same time in most cases [4].

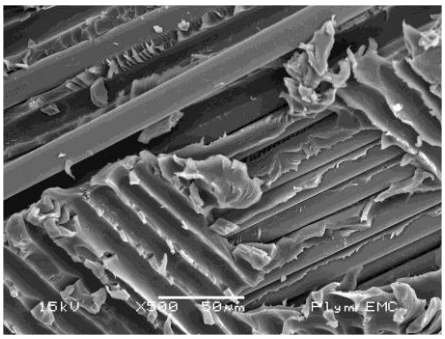

Figure 2.3. A damaged laminate with debonding failure mechanism at SEM [61].

Fibers are the reinforcing part of composite laminates. While other failure mechanisms are active, they are expected to withstand high stresses and keep the structure functional. Therefore, when fiber breakages start to occur, it is possible to say that the whole structure is about to fail. Due to the fact that the structure has already had several local weakened areas, fiber breakages make a domino effect and a catastrophic fracture is observed.

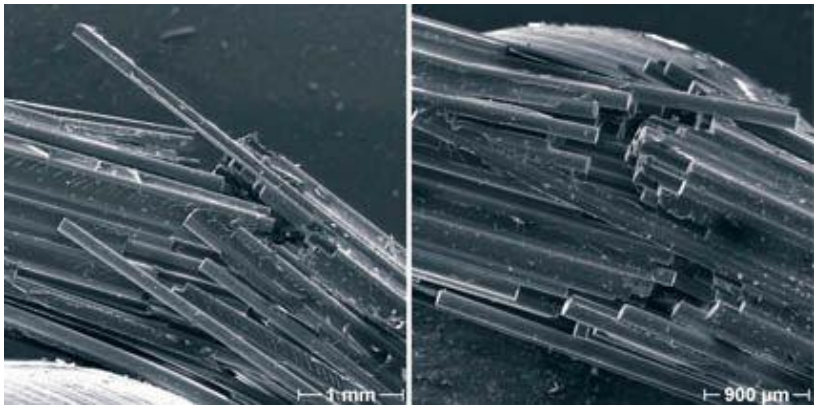

Figure 2.4. An SEM illustration of broken fibers [62].

Another failure mechanism that observed is kinking. When a fibrous laminate is subjected to a compressive load, micro buckling may be observed on fibers. If the fibers are not aligned with the compression axis, this will form a failure nucleus and causes kinking [63]. Kinking is a band of localized shear deformation, and in many cases it is considered as a result of material instability.

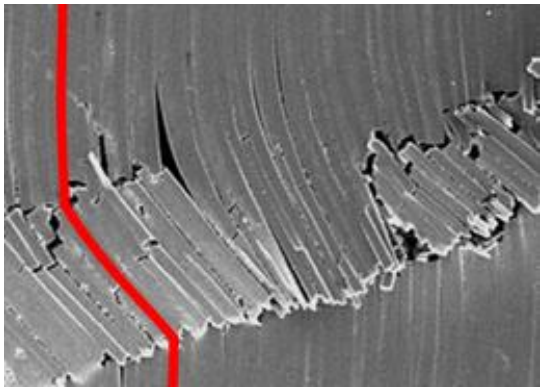

Figure 2.5. An SEM illustration of a kinked laminate [61].

An important failure mechanism for fiber reinforced composites is delamination. When randomly formed matrix cracks coalesce, they lead to delamination at the interface between the layers of laminate [64]. It can also occur because of the tensile stresses at the edges of the laminate. To model the delamination, the geometry of it is required, which is usually not known. Therefore, numerous tests have to be performed together with numerical simulations. Observation of failure zone and how progression unfolds is essential. This may provide additional understanding about how delamination zone extends. Delamination mostly occurs because of the presence of a geometric discontinuity or mismatch at Poisson's ratios of fiber and matrix materials [1].

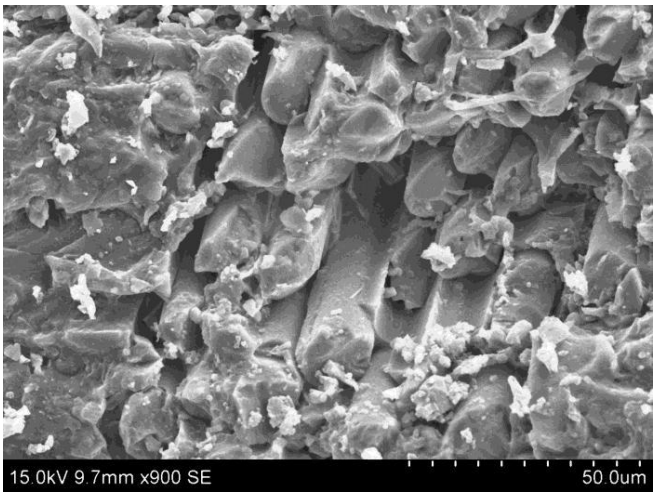

Figure 2.6. An SEM illustration of a delaminated structure [61].

The dominance of each failure mechanism is highly dependent to loading conditions and fiber orientations [4]. When a failure mechanism is activated, it creates a local weakened area, which changes the stress distribution in the lamina. When a lamina fails, it can no longer carry load and the stress is distributed between other laminae. As a consequence, the stress distribution changes at each lamina. If the remaining structure does not fail with the new stress distribution, it keeps carrying the load. Therefore, failure of a lamina does not necessarily mean failure of laminate. During a progressive failure, this occurs repeatedly until no lamina can withstand further.

2.2. Failure Criteria for Laminated Composites

After obtaining the stress and strain state using the classical laminate theory or finite element analysis, failure analysis of the laminate can be carried out. Predicting the failure load is essential for designing structural components. A reliable prediction allows designers to observe weak and strong points of the structure without performing money and time consuming physical tests and it guides them for improving their designs. To serve this purpose, several failure theories have been developed in years [5].

Although using a failure criterion to improve a design on paper is undeniably advantageous, the designer has to consider the fact that there are various factors which can affect the quality of a laminate structure. The production process may not cause any apparent difference in the macroscopic scale between two parts, but the mechanical behavior of them can be different due to the different extents of micro defects. Accordingly, strengths of different specimens with the same geometry may show scatter. Besides, the accuracy of the failure criteria may differ depending on the loading and geometric configuration. Failure criteria are only validated for a limited number of loading conditions and laminate configurations. Therefore, designers are advised to use more than one failure criterion and have a margin of safety instead of relying on only one failure criterion throughout the whole modeling process.

When the laminate structures which are manufactured by piling up unidirectional laminas with different fiber orientations are subjected to loading conditions, two basic failure modes are expected to occur. Firstly, delamination may occur if interlaminar stresses cannot be sustained by the layers. One of the main reasons of this type of failure is insufficient laminar bonding which is presumably caused by voids, imperfections or manufacturing errors [65]. It is possible to avoid delamination by following proper bonding methodologies. On the other hand, it is still an important mode of failure for laminates under fatigue loading or for thick laminates under static loading. Delamination requires more complex analyses and they are not considered in this study. Secondly, an individual layer may fail due to tension, compression, or shear. Fiber-matrix interface debonding, matrix cracking, fiber breakage and fiber pullout are common failure modes for fibrous composite materials.

To investigate the strength of a laminate structure under tension, compression or shear loads, each lamina has to be checked one by one according to proper failure criteria. This process requires stress and/or strain distribution at each lamina of the structure [5]. In practice, laminate structures are usually subjected to loads in such a way that stress and strain distributions of each lamina have to be extracted from the overall behavior. In such conditions, classical laminate theory is quite handy to overcome this problem and to extract desired data.

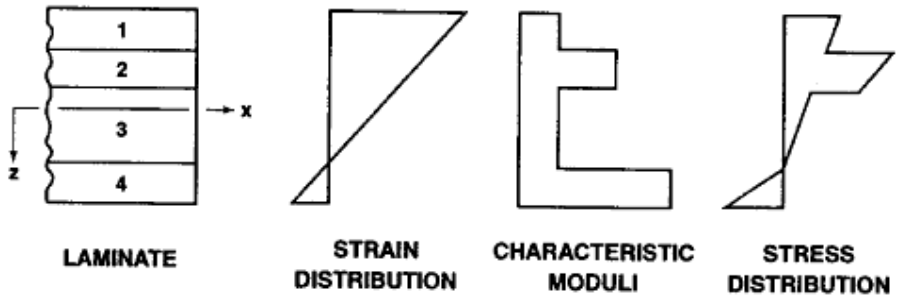

Figure 2.7. Stress and strain distribution of a composite laminate through the thickness [5].

Figure 2.7 represents bending test of a laminate structure [5]. Although strain changes continuously along the thickness, stress differs discontinuously because of having different mechanical properties at each layer according to a reference direction as a consequence of having different fiber orientations. Load is the measured data for this test. When it is evaluated together with extensional, coupling and bending stiffness matrices, mid-plane strains may be calculated via classical laminate theory. Following that, reduced stiffness matrices of each lamina are used to find stresses at each layer. At this point, the designer is capable of using stress and strain data of each layer for the failure analyses.

Maximum stress criterion and maximum strain criterion are widely used failure criteria. Each criterion consists of five sub-criteria. These five sub-criteria take the maximum allowable stress and strain values for longitudinal tension, longitudinal compression, transverse tension, transverse compression and shear loading conditions before failure occurs as limits. When the unidirectional lamina is subjected to a loading condition, the stress and strain fields are decomposed into two perpendicular components in lamina plane in such a way that while one direction coincides with the fiber direction, and the other coincides with the transverse direction. After that, each sub-criterion is

checked one by one. In case of limit excess for a sub-criterion, the part is assumed to have failed [66].

Equations 2.1-2.5 are the five sub-criteria of the maximum stress criterion. When the stress field on each lamina is calculated by classical laminate theory (see Appendix B), the subjected load is decomposed into its components in fiber and transverse direction for each lamina. Equation 2.1 is the first sub-criterion. F_{1t} is the maximum allowable tensile stress in fiber direction. If the component of the subjected load in fiber direction is in tension, denoted as σ_1, and greater than F_{1t}, the lamina is assumed to have failed. Similarly, F_{2t} is the maximum allowable tensile stress in transverse direction. As stated in Equation 2.2, if the component of the subjected load in transverse direction is in tension, denoted as σ_2, and greater than F_{2t}, the lamina is assumed to have failed. Equation 2.3 describes the third sub-criterion. F_{1c} is the maximum allowable compressive stress in fiber direction. Note that compressive stresses are denoted as negative values and the compressive strength of the materials may be different than its tensile strength in the same axis. Therefore, if the component of the subjected load in fiber direction is in compression, denoted as σ_1, and smaller than F_{1c}, the lamina is assumed to have failed. F_{2c} is the maximum allowable compressive stress in transverse direction (Equation 2.4). If the component of the subjected load in transverse direction is in compression, denoted as σ_2, and smaller than F_{2c}, the lamina is assumed to have failed. Finally, F_6 is the maximum allowable shear stress, independent from the sign. If the magnitude of the shear component of the subjected load, denoted as σ_6, is greater than F_6, the lamina is assumed to have failed (Equation 2.5). For a laminate structure, each sub-criterion has to be checked for each lamina in order to predict failure.

$$\sigma_1 \geq F_{1t} \tag{2.1}$$

$$\sigma_2 \geq F_{2t} \tag{2.2}$$

$$\sigma_1 \leq F_{1c} \tag{2.3}$$

$$\sigma_2 \leq F_{2c} \tag{2.4}$$

$$|\sigma_6| \geq F_6 \tag{2.5}$$

Similar to the maximum stress criterion, the maximum strain criterion consists of five sub-criteria (Equations 2.6-2.10). When the strain field in each lamina is known, these five sub-criteria have to be checked for each lamina one by one. Similarly, materials may undergo at different strain rate in compression or tension, although the loading axis is same. Equation 2.6 checks the strain in fiber direction under tension. ε_{1t}^{u} is the ultimate allowable strain for tensile loading in fiber direction. If the strain component of the strain field in fiber direction is positive, denoted as ε_1, and greater than ε_{1t}^{u}, the lamina is assumed to have failed. If the strain field in fiber direction is negative, and smaller than the ultimate allowable strain for compressive loading in fiber direction, ε_{1c}^{u}, the lamina is assumed to have failed (Equation 2.8). Similarly, Equation 2.7 checks the strain in transverse direction under tension. ε_{2t}^{u} is the ultimate allowable strain for tensile loading in transverse direction. If the strain component of the strain field in transverse direction is positive, denoted as ε_2, and greater than ε_{2t}^{u}, the lamina is assumed to have failed. If the strain field in transverse direction is negative, and smaller than the ultimate allowable strain for compressive loading in transverse direction, ε_{2c}^{u}, the lamina is assumed to have failed (Equation 2.9). Finally, if the magnitude of the shear strain, denoted as γ_6, is greater than γ_6^{u}, the ultimate allowable shear strain, the lamina is assumed to have failed (Equation 2.10).

$$\varepsilon_1 \geq \varepsilon_{1t}^{u} \tag{2.6}$$

$$\varepsilon_2 \geq \varepsilon_{2t}^{u} \tag{2.7}$$

$$\varepsilon_1 \leq \varepsilon_{1c}^{u} \tag{2.8}$$

$$\varepsilon_2 \leq \varepsilon_{2c}^{u} \tag{2.9}$$

$$|\gamma_6| \geq \gamma_6^{u} \tag{2.10}$$

When the stress and strain fields in each lamina are found via classical laminate theory and decomposed into fiber and transverse directions, Equations 2.1-2.10 have to be checked one by one. If any of these equations is satisfied for a lamina, that lamina is assumed to have failed. Maximum stress criterion and maximum strain criterion make reliable predictions for uniaxial loading conditions. However, when the lamina is subjected to a multi-axial stress state, the failure loads may differ from the values presumed by maximum stress and strain criteria. Jones *et al.* [5] plot the maximum stress and maximum strain criteria for a loading case for glass-epoxy matrix. Their mechanical data is taken from the studies of Tsai [67]. The solid curves on Figure 2.8a and Figure 2.8b correspond to maximum stress and maximum strain criteria, respectively [5]. As seen on the plots, the theoretical cusps in strength variation are not seen in the experimental data. Therefore, using an interactive failure criterion gives better predictions.

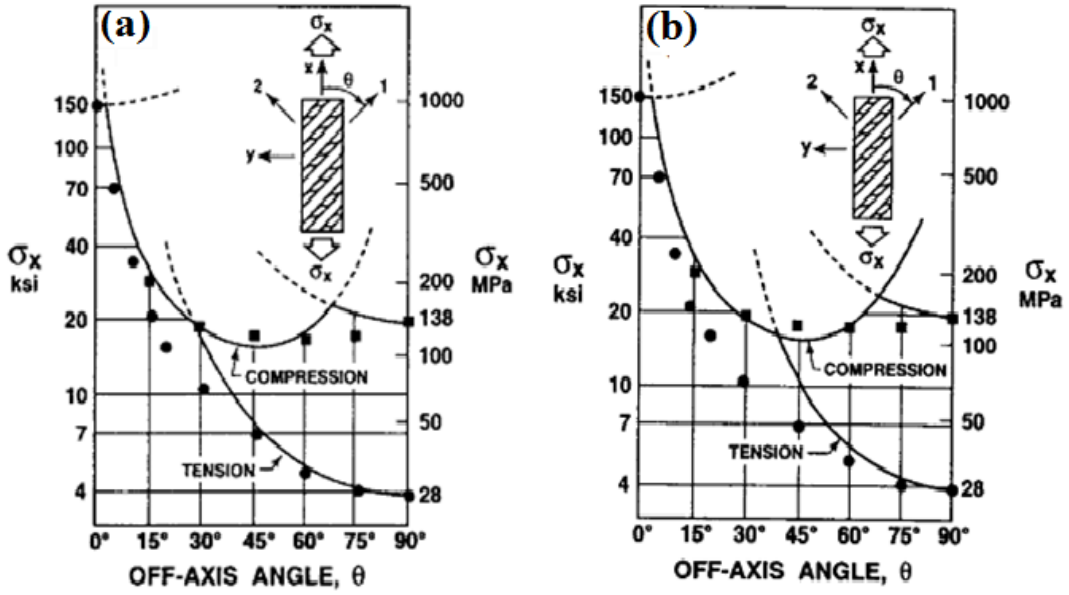

Figure 2.8. Comparison of (a) maximum stress and (b) strain criteria with experimental results [5].

Among various interactive criteria, Tsai-Hill criterion is used in this study. As stated by Jones *et al.* [5], the agreement between Tsai-Hill criterion and experiments is quite good for laminate composites made of E-glass-epoxy, which is the material of the specimens tested in the present study.

Tsai-Hill failure criterion was proposed by Tsai in 1968 as an extension of Hill's anisotropic plasticity model, which can be traced back to Von Mises yield criterion. For a multi axial loading condition, it simply combines sub-criteria of maximum stress criterion and evaluate the strength of a lamina interactively [65].

$$\alpha^2 = \left(\frac{\sigma_l}{\sigma_{l,rupture}}\right)^2 + \left(\frac{\sigma_t}{\sigma_{t,rupture}}\right)^2 - \frac{\sigma_l \sigma_t}{\sigma_{l,rupture}^2} + \left(\frac{\tau_{lt}}{\tau_{lt,rupture}}\right)^2 \tag{2.11}$$

Equation 2.11 represents Tsai-Hill failure criterion [65]. When a unidirectional lamina is subjected to a multi axial loading condition, loads are resolved into longitudinal and transverse directions in the first place and substituted into the failure criterion together with corresponding failure strength values. The strength values may differ for materials whether loading is tensional or compressive. If the right hand side of the equation is equal or bigger than 1, the lamina is assumed to have failed. For a laminate structure, the criterion has to be applied to each lamina individually [65]. Figure 2.9 shows the plot of Tsai-Hill failure criterion for the same tension test, taken from the studies of Tsai [67].

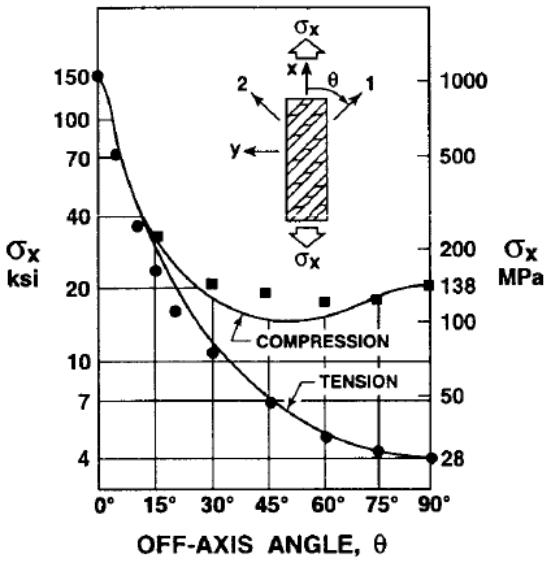

Figure 2.9. Comparison of Tsai-Hill failure criterion with the experimental results [5].

One should note that when a lamina within a laminate structure fails and loses its strength to carry loads, the rest of the structure may keep carrying. Therefore, failure of a

single lamina does not necessarily mean that the whole laminate structure has failed [68]. This mechanical behavior should be taken into consideration during design stage.

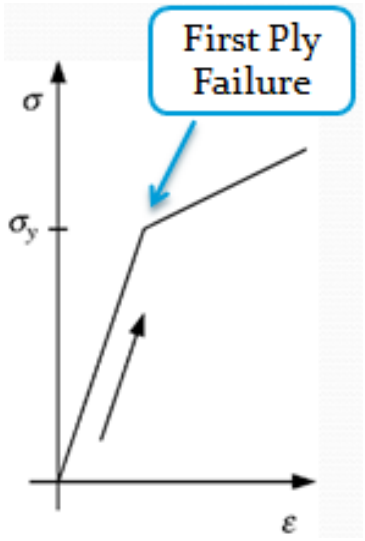

Figure 2.10. An ideal stress-strain curve for a laminate structure.

Figure 2.10 illustrates an example stress-strain curve for a laminate structure. At a certain stress level, first ply failure occurs and that lamina has become incapable of carrying load. Failure of a lamina can be theoretically imitated by setting all the components of transformed stiffness matrix of it to zero for further calculations. This intervention changes the A, B, and D matrices and expectations for macroscopic response of the laminate for further loading, which can be seen as change at slope. Failure of a lamina, theoretically recalculation of A, B, and D matrices, causes change of stress distribution at remaining laminae and if the remaining structure does not fail, it keeps carrying loads as expected.

Unlike maximum stress or maximum strain criteria, the mode of the failure cannot be told with Tsai-Hill failure criterion [65]. The criterion gives only one value for comparison and it is found by an interactive calculation. Figure 2.8 shows failure stress and failure strain values for each sub-criterion of maximum stress and maximum strain criterion and their change according to the angle between fiber direction and tensile direction. As stated previously, maximum stress and strain criteria do not take the interactions between different stress components into account. As seen in Figure 2.9, the variation of the lamina strength with the angle of lamina orientation is much smoother than maximum stress or

strain criteria which contain cusps that are not observed with experiments. Maximum stress and strain criteria assume longitudinal, transverse and shear failure occur independently which does not coincide with reality. As stated by Jones *et al.* [5], Tsai-Hill failure criterion should be accepted as one of the most reliable failure criteria for laminates with continuous E-glass fibers with epoxy matrix.

3. PREPARATION OF SPECIMENS

Sandwich composites may possess various geometrical configurations and can be made up of different materials such as metallic alloys and polymers. It is possible to develop different manufacturing methodologies for different configurations. Sandwich composites usually have isotropic metallic sheets or laminated composite parts as face sheets [2]. However, almost all configurations use isotropic materials for their core section. For this thesis study, both the core and the facesheets of the sandwich structure are laminated composite structures themselves. Among various manufacturing techniques, vacuum infusion process (VIP) is preferred to manufacture experimental specimens, due to its significant advantages.

3.1. The Procedure

Sandwich composite specimens used in the tests are produced by vacuum infusion process, which is explained in Appendix A. For some configurations, it is possible to manufacture the whole sandwich structure together as one part. However, the face sheets and the core are produced separately in this study because of the geometric complexity. In this section, the procedure for specimen preparation is presented step-by-step.

- VIP requires a rigid and clean surface on which dry reinforcements are placed. A properly cleaned thick glass is sufficient for two face sheets. On the other hand, a three dimensional mold must be used for the core. The glass in Figure 3.1 is wide enough to manufacture components larger than one square meter. The mold in Figure 3.2 is made of RenShape® and it is shaped by CNC machining. It is coated with lacquer.

- E-glass fiber is chosen as the reinforcement material in this study. Glass fiber reinforcements can be commercially found in rolls with desired orientations and densities. The operator cuts the glass fiber roll to provide desired stacking sequence and dimension.

Figure 3.1. The thick layer of glass.

Figure 3.2. The lacquer coated mold.

- Peel ply is vital for the vacuum infusion process. When the dry reinforcement is impregnated under the vacuum pressure, the resin may bond with other setup components unless there is a separating peel ply layer. In order to provide a proper separation, peel ply should be larger than the part to cover it.

Figure 3.3. (a) Peel ply and (b) glass-fiber reinforcement.

- Epoxy is chosen as the resin material in this study. Despite having relatively acceptable viscosity values, its penetration speed under vacuum pressure may not be fast enough to wet the whole part before solidification starts. On the one hand, the flow mesh enables the resin to infuse much faster and decreases the risk of a premature solidification. On the other hand, it also helps the vacuum pump to extract air. The operator cuts the flow-mesh layer with almost the same dimensions as that of the part.

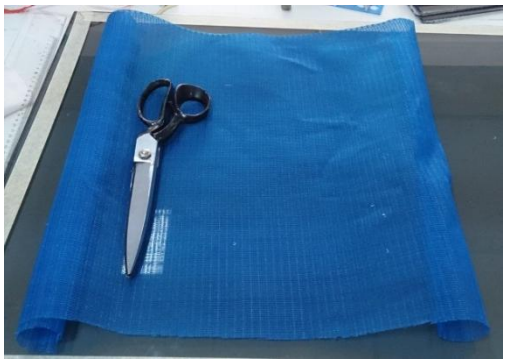

Figure 3.4. Flow mesh.

- Under the vacuum pressure, the resin will follow the shortest route to reach the outlet. Therefore, a spiral tube should be placed as an extension of inlet and a second flow mesh as an extension of outlet to provide uniform resin flow. A schematic drawing is represented in Figure 3.5 [69]. The operator cuts spiral tube and a second flow mesh. In addition to these components, plastic tubes for inlet and outlet are also cut.

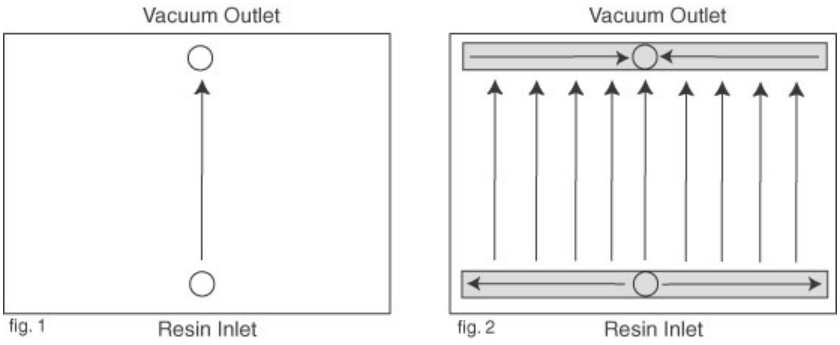

Figure 3.5. The schematic diagram for tubing [69].

- Vacuum bag is cut in the desired dimensions.

- The regions on which sealing tapes are going to be stuck are covered by paper tape since the mold surfaces will be coated by mold release wax. Direct contact of the tape with the wax may decrease its sealing performance and cause leakage.

- The designated zones are coated by mold release wax carefully (Figure 3.6).

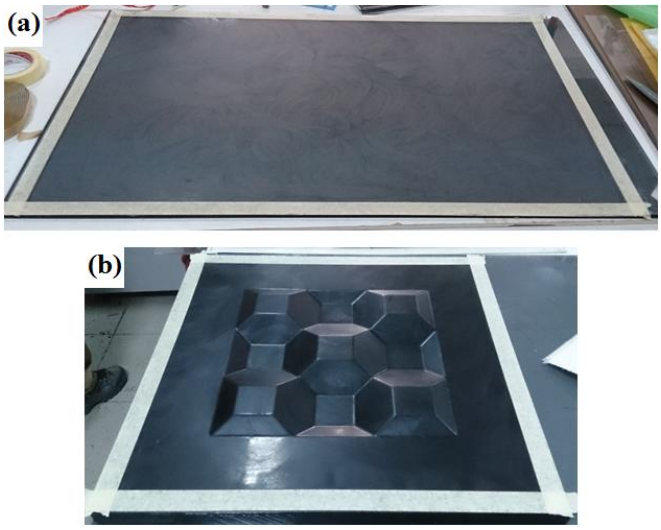

Figure 3.6. The waxed (a) glass-plate mold and (b) core-mold surfaces.

- The paper tapes are replaced with sealing tapes. Fiber glass layers are placed on the wax coated zones observing desired stacking sequence and fiber orientations. There is a slight difference between the face and core production. An additional peel ply layer is put underneath the reinforcement material to protect the surface of the three dimensional lacquer coated mold (Figures 3.7 and 3.8).

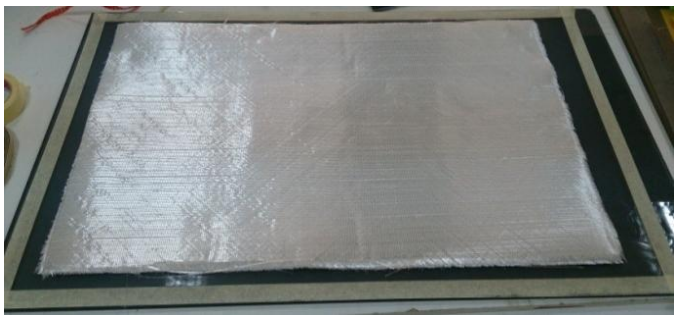

Figure 3.7. Placing of reinforcements on the glass surface.

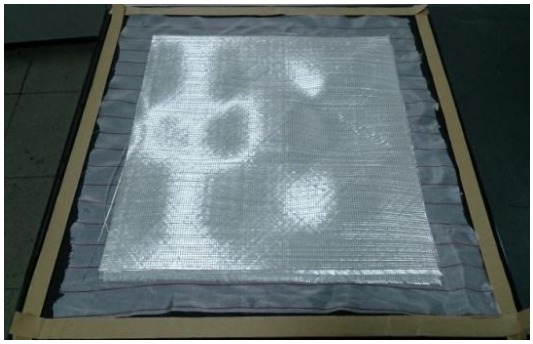

Figure 3.8. Placing of reinforcement on the mold surface.

- Peel ply is spread over the fiber glass layers.

- Inlet and outlet tubes are placed very carefully. Their mouth regions are smoothed because of the fact that any sharp edge may puncture the vacuum bag and cause leakage.

- Spiral tube is placed as an extension of the inlet and covered by peel ply layer. On the other side, the second flow mesh is placed as an extension of outlet. Unlike the first flow mesh, the second one is only beneficial for air extraction. Therefore, it does not touch the reinforcement or other components directly. Instead, the connection is made by special pads which block resin infusion while enabling air extraction.

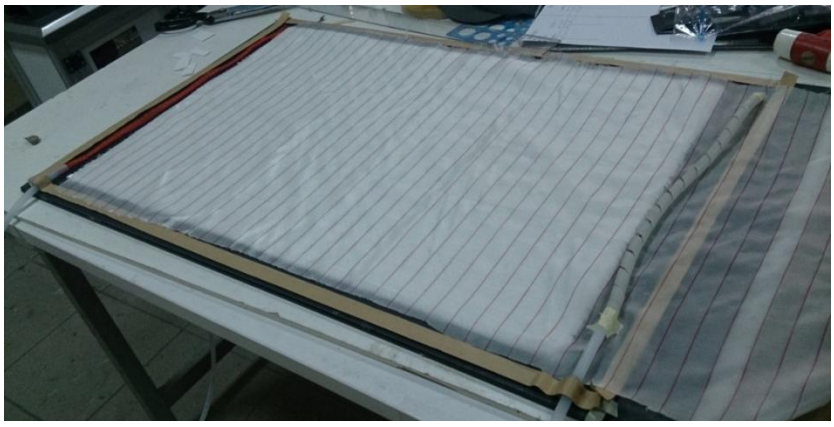

Figure 3.9. Placement of peel ply.

- Flow mesh is placed on the peel ply layer to speed up resin infusion.

- The vacuum bag is stuck by the sealing tape. Note that the vacuum bag is a flexible membrane. However, its flexibility has a limitation. Hence, there will not be another chance to fix an incorrect placement. Therefore, this step is advised to be done very carefully (Figure 3.10).

Figure 3.10. The sealing procedure.

- The vacuum pump is switched on to extract the air inside. Because the inlet is previously blocked by the operator, the pressure in the vacuum bag drops to zero ideally, to very low values practically (Figures 3.11 and 3.12). At this point, there is a chance for the operator to investigate the whole setup for leakage. It is advised to take his/her time. This step is considered to be the most critical step of the whole process because of the fact that once resin infusion begins, it is irreversible. Any potential error such as air entrapment in the final product may be fatal for it.

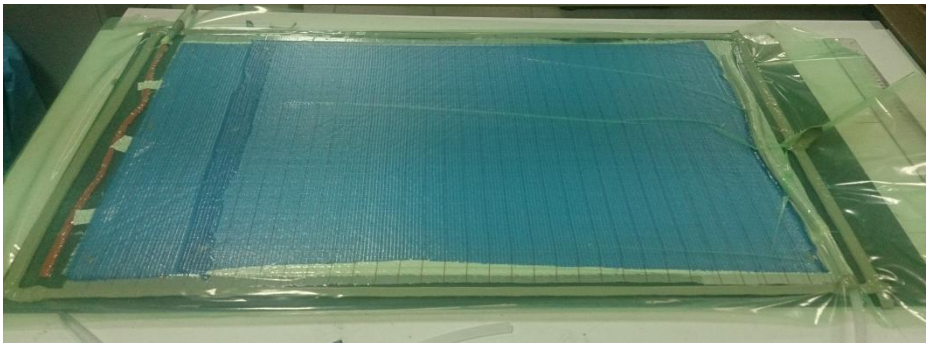

Figure 3.11. The setup under vacuum pressure.

- A second check is done by blocking the outlet and switching off the vacuum pump (the pump should prevent the air from being sucked back into the vacuum bag) after

extracting the air and observing the change in pressure. 0.1 bar of pressure rise within 15 minutes is acceptable.

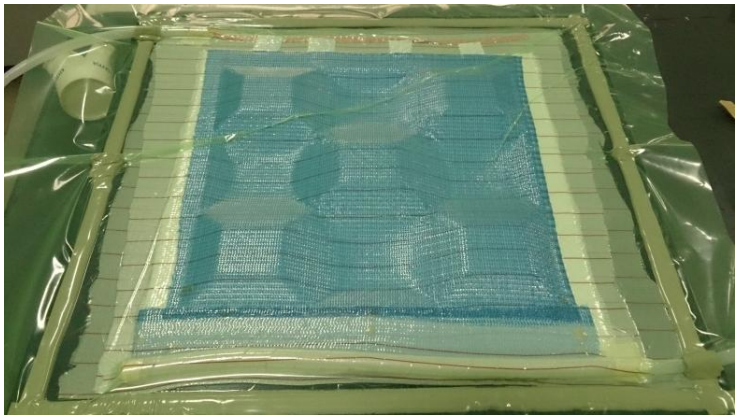

Figure 3.12. Three dimensional laminate under pressure.

- Once the sealing quality is ensured, the operator may proceed to prepare the resin. In this study, L285 laminating resin with H285 hardener is selected to make the epoxy resin ready for impregnation. The operator is advised to mix the two elements in accordance with the instruction notes. Since the mixture contains air bubbles and dissolved gases, degassing procedure has to be followed prior to impregnation by simply putting the mixture into a vacuum chamber while taking the pot life into account.

- The inlet tube is sunk into the resin reservoir before removing the blockage. As the crucial detail, the ambient air should not be allowed to be sucked into the vacuum bag anymore. This can be achieved by preparing resin more than the required amount. Once the reinforcement is totally impregnated by the liquid resin, the inlet has to be blocked again carefully. The excessive resin in the vacuum bag will be eventually sucked out of vacuum bag.

- The pot life of the resin material varies depending on the temperature. The higher is the temperature of the resin, the faster is the solidification process. The vacuum pump has to be kept switched on during the whole solidification process. In this study, the pump continues to work for three extra hours, required time for gelation.

However, the total curing requires at least one day. The part can be subjected to further heat treatment if it is desired.

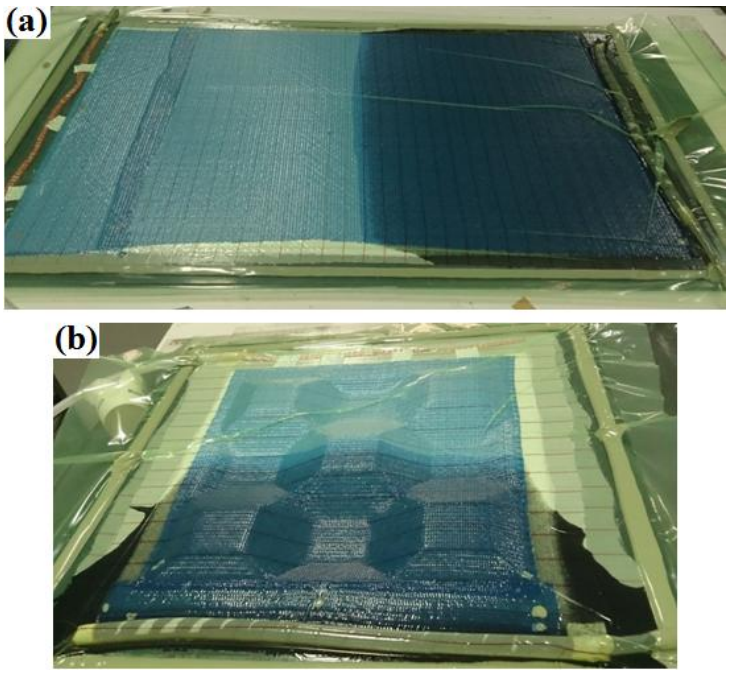

Figure 3.13. Resin impregnation to (a) flat and (b) three dimensional parts.

- After consolidation, the face or core part is removed gently from the glass plate or the 3D-mold surface. Peel ply is removed from the parts slowly while paying attention to the potential risk of delamination due to excessive force applied by the operator (Figure 3.14).

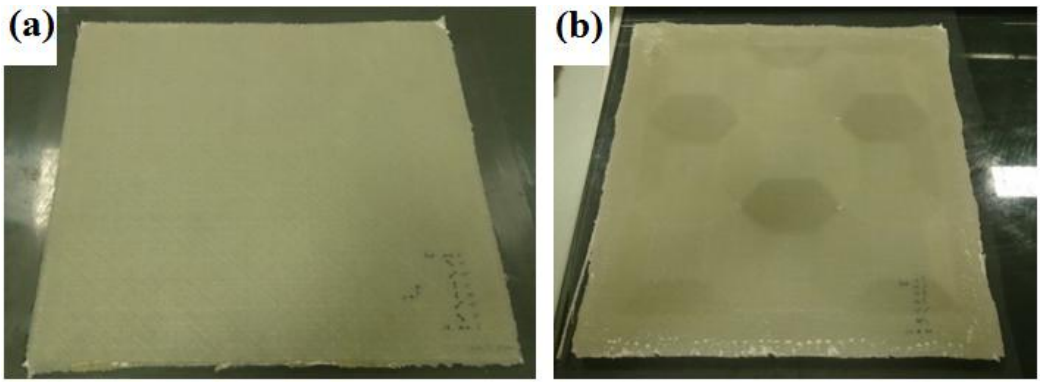

Figure 3.14. Final (a) sheet and (b) core parts.

- For a single sandwich structure, one core and two face sheets are required. Instead of manufacturing two facesheets in two steps, one large flat part can be manufactured and cut into two pieces to obtain two facesheets. However, the operator should note that the final surfaces on the two sides of a flat part are not the same in terms of surface toughness and for the gluing to be effective, at least one of the bonded surfaces should be rough. Therefore, the operator has to flip one facesheet which is cut from the large plate; but this may result a change in the stacking sequence. Instead, the operator can create two different and separate areas under the vacuum bag with two different stacking sequences taking the flipping step into account. Once the core and face sheets are ready, the core and one face sheet are bonded to each other by applying an adhesive. The operator is advised to attach only one side in one step. For a better bonding quality, heavy blocks are placed on the top during the curing time in ambient temperature to generate sufficient pressure.

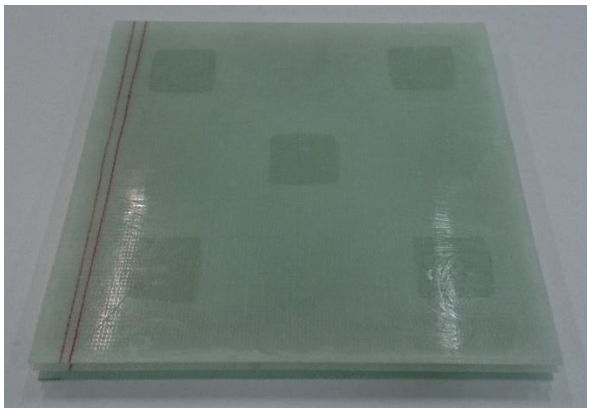

Figure 3.15. The manufactured sandwich plate.

3.2. Quality of the Parts

VIP is considered to be one of the most suitable manufacturing techniques for fiber reinforced polymer composites. The operator can obtain high quality products repeatedly, especially for 2D parts. On the other hand, it is possible to face some local defects such as wrinkling (Figure 3.16a), undulation (Figure 3.16b) or resin accumulation (Figure 3.16c) while manufacturing 3D parts. This occurs because of the use of two dimensional reinforcement sheets, which are put into 3D form during the process.

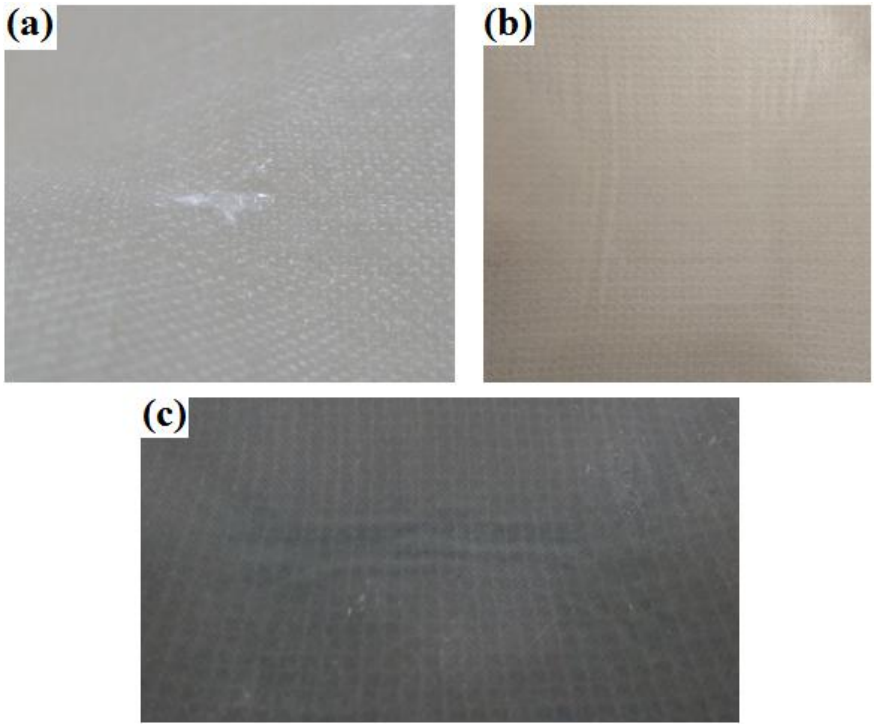

Figure 3.16. Typical manufacturing problems of VIP technique: (a) Wrinkling, (b) undulation, and (c) resin accumulation.

3.3. Test Standard

ASTM D3039 standard test methodology is followed to determine in-plane tensile properties of the laminated composite with epoxy resin matrix reinforced by continuous E-glass fibers. D3039 is a standardized test method specified by American Society for Testing and Materials for determining tensile properties of polymer matrix composite materials [70]. Several mechanical properties in tensile direction including ultimate tensile strength, ultimate tensile strain, modulus of elasticity, Poisson's ratio and transition strain may be obtained from this test methodology.

The standard indicates that at least five specimens need to be tested for each test condition. In this study, this requirement is satisfied by testing 10 specimens, two different stacking sequences are available for the reinforcement. For the case 1 and 2, the specimens have layup sequences of $[0/90]_{2s}$ and $[0/45/-45/90]_{s}$, respectively. Mid-plane symmetry sets all the elements of coupling stiffness matrix zero. A null coupling stiffness matrix signifies that in-plane loads do not generate bending or twisting. Testing randomly arranged

stacking sequence combinations is possible and the desired values may be extracted via post-processing, which is highly impractical.

D3039 standard does not oblige an exact geometry with defined dimensions for the tension specimens and the tabs. Instead, it sets a range for them. D3039 standard describes the parametric dimensional requirements of the tension specimens and the tabs, the specimen geometry and tolerance values, see Appendix D.

As stated in D3039, many factors may influence the tensile response of specimens such as material preparation technique, stacking sequences, specimen preparation, ambient conditions before and during the test, specimen alignment, gripping, loading rate or entrapped air [70].

3.4. Preparation of Tension Specimens

The tension tests are performed with two different groups of specimen. In order to do that, two plates with $[0/90]_{2s}$ and $[0/45/-45/90]_{s}$ stacking sequences are manufactured by VIP. The plates are cut into pieces with water cooled diamond blade in such a way that the fiber direction of the top and the bottom layers in each set make an angle of 0^{o} with the tensile direction.

In order to ease tab bonding process and to make better measurements of material properties such as weight, the plate should be cut into large pieces. The dimensions of the specimens are taken as 25 mm in width, 250 mm in length while tabs are 50 mm in length. Considering the dimensions of the specimens, the large plates are cut from the plate (Figure 3.17). Similarly, a quasi-isotropic plate is also manufactured and cut into pieces.

The specimens are mounted to the test machine in the vertical direction, in other words tension direction, which is assigned as 0^{o}. The stacking sequences are called according to this assignment.

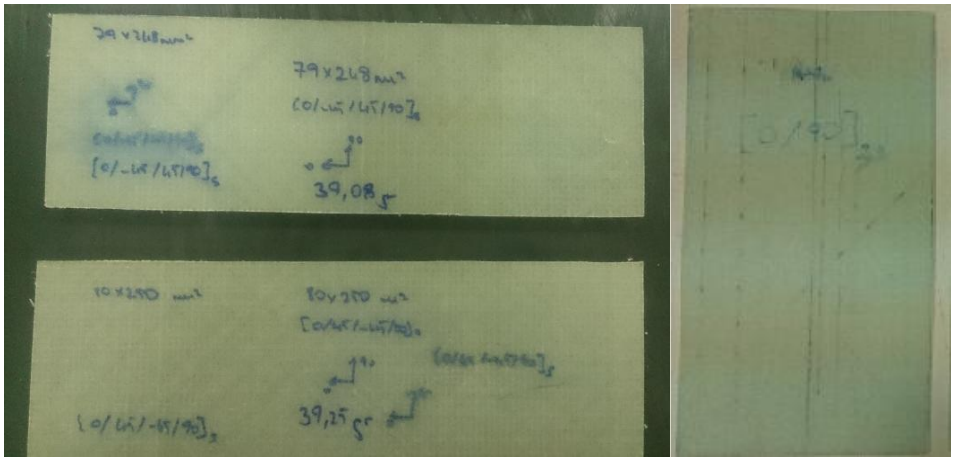

Figure 3.17. Specimen sets as one part.

Table 3.1. The dimensions and the weights of the manufactured plates.

Plate #	Stacking	Length [mm]	Width [mm]	Weight [gr]
1	$[0/90]_{2s}$	250	140	75.8
2	$[0/45/-45/90]_{2s}$	248	79	39.08
3	$[0/45/-45/90]_{2s}$	250	80	39.25

Plate 1, 2 and 3 are cut from the large laminated plates using water cooled diamond blade and the edges are grinded with sandpaper. Weight, width and length are measured by the operator and the measured values are tabulated in Table 3.1.

It is possible to find various kind of E-glass fiber cloth in the market with different specifications. The fabric can be weaved by using continuous fibers or these fibers can be stitched to obtain multi-axial textiles. Manufacturers can also provide clothes with different densities. In this thesis study, fiberglass clothes are delivered as rolls from the company of METYX®. The operator uses [0/90] biaxial cloth and [0/45/-45/90] quasi-axial cloth to produce tension specimens. Their properties are listed in Table 3.2.

Table 3.2. Mechanical constants and unit weight of the used cloths [3].

	[0/90] biaxial cloth	[0/45/-45/90] quasi-axial cloth
Unit weight [gr/m^2]	343.6	630
E_1 for 0^o lamina [GPa]	72.4	72.4
Poisson's ratio	0.22	0.22
G for 0^o lamina [GPa]	26.2	26.2

For the epoxy resin, a product of HEXION® is selected. As mentioned previously, epoxy resin is delivered in two separate containers as laminating resin MGS® L285 and hardener MGS® 285. The mixing ratio for L285:H285 is stated in the technical instructions as 100:40 ± 2 in terms of weight. This ratio has to be observed carefully since it affects the irreversible solidification process and influences the material properties of neat resin. The two liquids have to be mixed until no clouding is visible and a homogeneous mixture is obtained. The properties of the hardened resin are given in Table 3.3 [71].

Table 3.3. The properties of the hardened resin [71].

Density [gr/cm^3]	1.12
E_1 [GPa]	3.2
Poisson's ratio	0.36
G [GPa]	1.18

The tabs are bonded to the plates using ARALDITE® 2000+ adhesive which offers high performance and durable long term bonding. The same adhesive is used to join the face sheets of the sandwich composite specimens to the core part as well. Heavy blocks are placed on top to apply pressure (Figure 3.18a). The heavy blocks should stay at least 12 hours during the solidification of the adhesive in order to obtain high bonding quality.

Once the applied adhesive layer hardens, each plate is cut into pieces in order to obtain tension test specimens. Instead of cutting the each specimen from the large plate in the first place and bond the tabs one by one, the followed methodology enables the operator to control any misalignment of the tabs easily and eases the procedure. Therefore, the obtained pieces have better tab alignments. Each specimen is numbered starting from 1. The dimensions are measured at different places after edge grinding process and tabulated in Tables 3.4 and 3.5.

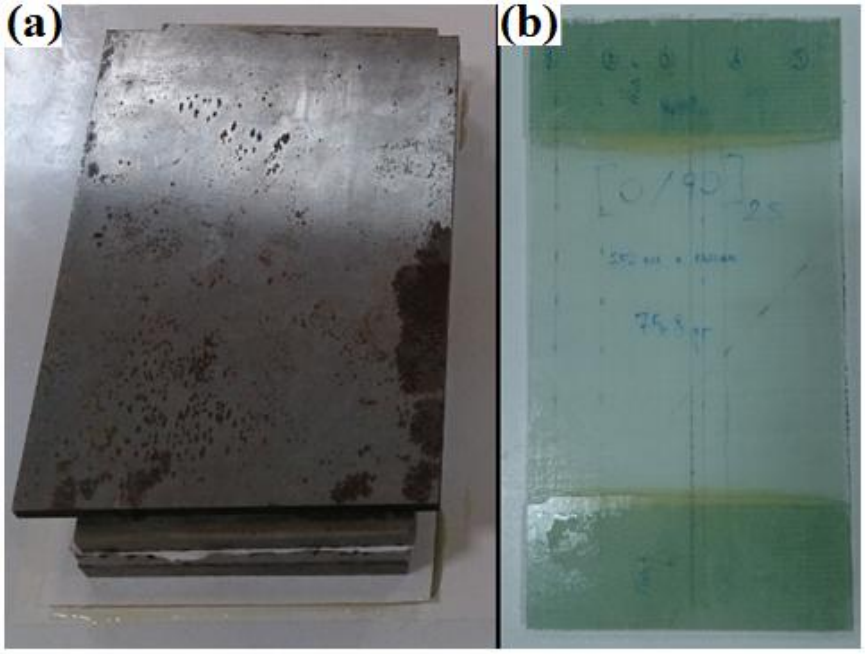

Figure 3.18. (a) Placement of a heavy block in order to apply pressure and (b) the plate after the adhesive solidification process.

Table 3.4. Properties of specimen 1 to 5.

	Plate 1: $[0/90]_{2s}$				
Specimen #	1	2	3	4	5
Specimen width [mm]	24.61	24.21	24.07	25.14	25.1
Specimen thickness [mm]	1.29	1.32	1.31	1.36	1.36
Plate area [cm^2]	14 x 25 = 350				
Plate volume [cm^3]	46.48				
Plate weight [gr]	75.8				
Weight of used fiber [gr]	0.035 x 4 x 343.6 = 48.1				
Weight of used resin [gr]	27.7				
Vol. of used resin [cm^3]	27.7 / 1.18 = 23.47				
Vol. of used fiber [cm^3]	23.1				
Fiber volume fraction [%]	49.5				
Resin volume fraction [%]	50.5				

Table 3.5. Properties of specimen 6 to 10.

	Plate 2: $[0/45/-45/90]_{2s}$			Plate 3: $[0/45/-45/90]_{2s}$	
Specimen #	6	7	8	9	10
Specimen width [mm]	24.3	24.2	24.6	24.8	24.5
Specimen thickness [mm]	1.2	1.21	1.18	1.19	1.21
Average thickness [mm]	1.2			1.2	
Plate area [cm^2]	7.9 x 24.8 = 195.92			8 x 25 = 200	
Plate volume [cm^3]	23.5			24	
Plate weight [gr]	39.08			39.25	
Weight of used fiber [gr]	0.0196 x 2 x 630 = 24.69			0.02 x 2 x 630 = 25.2	
Weight of used resin [gr]	14.56			14.05	
Vol. of used resin [cm^3]	14.6 / 1.12 = 13			14. 05 / 1.12 = 12.54	
Vol. of used fiber [cm^3]	10.5			11.45	
Fiber volume fraction [%]	44.7			47.8	
Resin volume fraction [%]	55.3			52.2	

Volumetric fractions of the fiber and the resin are used to find the material constants of tension specimens theoretically. These properties are essential to determine [*A*], [*B*] and [*D*] matrices.

4. ACOUSTIC EMISSION MONITORING OF LAMINATED COMPOSITE STRUCTURES

The main failure mechanisms that lead to failure of a laminated composite structure under loading are matrix cracking, fiber-matrix interface debonding, delamination and fiber breakage [72]. Since each failure mechanism creates characteristic signals, these signals recorded via acoustic emission monitoring can be used to identify the types of activated failure mechanisms in laminated structures [73]. Especially for the parts in service, such as pipes or pressure vessels, this non-destructive testing methodology is quite helpful to detect any defect.

When the piezoelectric transducer detects a waveform and converts it into an electric signal, the software records previously selected parameters such as amplitude, rise time, counts and duration into a single hit datum with the time of the event. A brief summary about acoustic emission monitoring is given in Appendix C. While performing an experiment or a standardized test under acoustic emission monitoring, the software is capable of receiving external data related to the position of grips or load. During a tension test of a laminated composite specimen, a single transducer can easily detect more than 1000 hits. In most cases, multiple transducers are mounted on specimens. As a result, thousands of hits can be detected during a single test and evaluation of their parameters and corresponding waveforms may reveal the activated failure mechanisms.

To identify the failure modes, researchers have developed several techniques to evaluate the AE data.

4.1. Parameter Based Approaches

Parameter based approaches evaluate AE data by considering hit parameters, especially amplitude, duration, rise time, counts, and energy. These values are extracted from the acoustic wave, which are highly dependent on the material itself. In addition, even the position of the transducer (distance from the source) may influence the form of the recorded wave [74]. Therefore, it is simply impossible to create a strict chart that is

always valid and applicable. Nevertheless, it can be deduced from the previous studies that while micro cracking generates AE signals in the low-range, debonding and delamination are observed in the mid-range [73]. On the other hand, fiber-originated failure mechanisms generate acoustic waves in the high-range [72]. In addition to these, studies on similar material types may help the operator to develop an understanding.

4.2. Pattern Recognition Techniques

Besides parameter based approaches, several pattern recognition techniques have been developed to identify the failure mechanisms in materials. Instead of using a single parameter which is extracted from the detected acoustic wave, these techniques are based on the classification of several parameters into clusters forming patterns [73]. The similarities and differences between these parameters are taken into account to classify AE data.

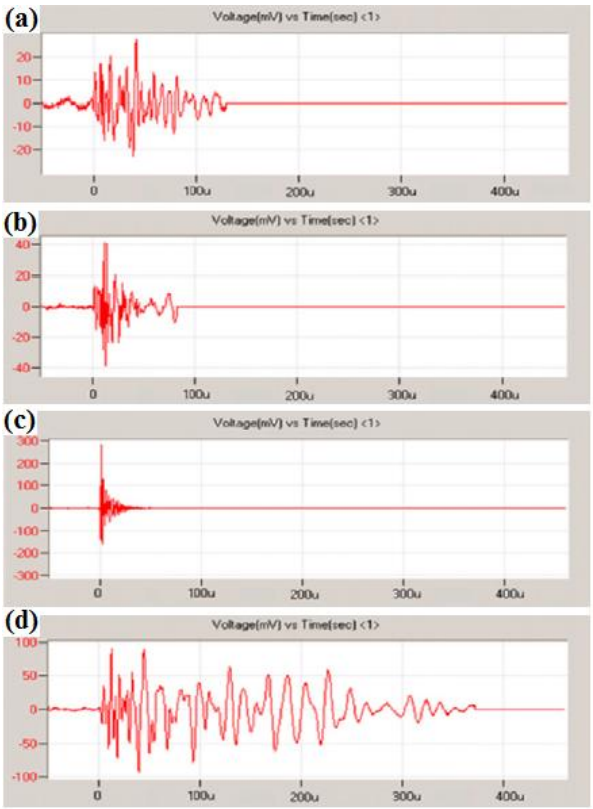

Figure 4.1. Typical detected AE waveforms generated by different failure mechanisms: (a) Matrix cracking, (b) fiber-matrix debonding, (c) fiber breaking, and (d) delamination [75].

Figure 4.1 shows typical examples of the waveforms corresponding to failure mechanisms for laminated composite structures [75]. As seen in the graphs clearly, several methods can be developed to classify similar waveforms. A number of researches have used various pattern recognition techniques for this purpose. Among several methods, K-mean algorithm, Kohenen's self-organizing map, fuzzy C-means clustering with principle component analysis are the popular techniques [73].

4.3. Fast Fourier Transform

Another reliable technique is fast Fourier transform (FFT) analysis. It is a version of discrete Fourier transform, which transforms a discrete signal in the time domain into its discrete frequency domain [76]. Its discrete nature and speed allow the FFT algorithm to do the same transformation faster. Its speed makes analyzing a signal's spectrum in real-time possible.

The amplitude or duration of a signal may vary according to the position of source relative to the transducers. On the other hand, time-domain to frequency-domain transformation reveals the dominant (peak) frequency of the detected wave and it retains the same dominant frequency independently of transducer's position [73]. Since the failure mechanisms create characteristic signals, the dominant frequency of a detected wave can be directly related to the responsible failure mode. For this purpose, many different algorithms have been developed by using wide range of mathematical techniques.

As seen in the literature, the corresponding frequency ranges for typical failure mechanisms in laminated composites change according to the material types. On the other hand, the general understanding that they provide is highly beneficial for the interpretation of data obtained in tests with different material combinations.

4.3.1. Visual Basic Coding

In order to find the peak frequency value of a single AE hit datum, the FFT function in Excel can be used. However, it is not practical for the evaluation of a set of AE data with 5000 hits. Therefore, a Visual Basic code is written. When the code is executed, it

performs an iterative study and makes a list of peak frequency magnitudes for the data set in the designated folder.

4.4. Acoustic Emission Studies in the Literature

Many researchers have studied acoustic emission parameters to identify the activated failure modes for laminated composites with fiber-reinforced polymer matrix structures [73]. The majority of these researchers have focused on amplitude parameter. In 1978, Wadim [77] managed to correlate different ranges of amplitude parameter with different failure mechanisms. He stated that while matrix cracking is responsible for lower ranges, delamination and fiber failure cause higher ranges. Gong *et al.* [78] succeeded to refine the ranges in late 1990s by inserting friction before breakage phenomenon into intermediate ranges. As seen in Table 4.1, some other researchers defined different ranges by performing experiments with different types of fiber and matrix materials.

Laksimi *et al*. [79] reported that the source of amplitude range of 33-45 dB was micro cracking mechanism; micro crack growth originated signals were expected between 45-58 dB; fiber-matrix debonding generated acoustic waves in the range of 58-68 dB; friction at matrix and fiber interface created signals between 68-86 dB; higher amplitudes characterized fiber fracture.

Table 4.1. Different amplitude parameter based classification methodologies [80].

	Matrix micro cracking	Matrix/matrix friction	Debonding	Matrix/fiber friction	Fiber breakage
Wadim	30-45 dB		45-55 dB		65-100 dB
Kim *et al*.	40-70 dB				60-100 dB
Kotsikos	40-55 dB	55-70 dB	55-70 dB		80-100 dB
Gong *et al*.	34-46 dB	46-58 dB	58-68 dB	68-86 dB	86-100 dB
Meraghni *et al*.	35-48 dB	48-60 dB	60-65 dB	65-82 dB	82-100 dB
Laksimi *et al*.	33-45 dB	45-58 dB	58-68 dB	68-86 dB	86-100 dB

Aramugam *et al*. [81] performed standard tensile (ASTM D3039) tests on GFRP specimens. Figure 4.2 corresponds to AE data of a single layer specimen. He classified the AE data in terms of amplitude parameter in low, medium and high ranges as 48 dB to 65

dB, 65 dB to 85 dB and 85 dB to 99 dB, respectively. The amplitude distribution was also in correlation with duration parameter. He described the stages as damage initiation, micro crack formation, unstable crack growth, fiber-matrix debonding and fiber failure by evaluating duration and amplitude parameters with cumulative count parameters.

Similarly, Bussiba *et al*. [82] evaluated counts rate and cumulative counts to identify failure modes at fiber reinforced polymer matrix composites.

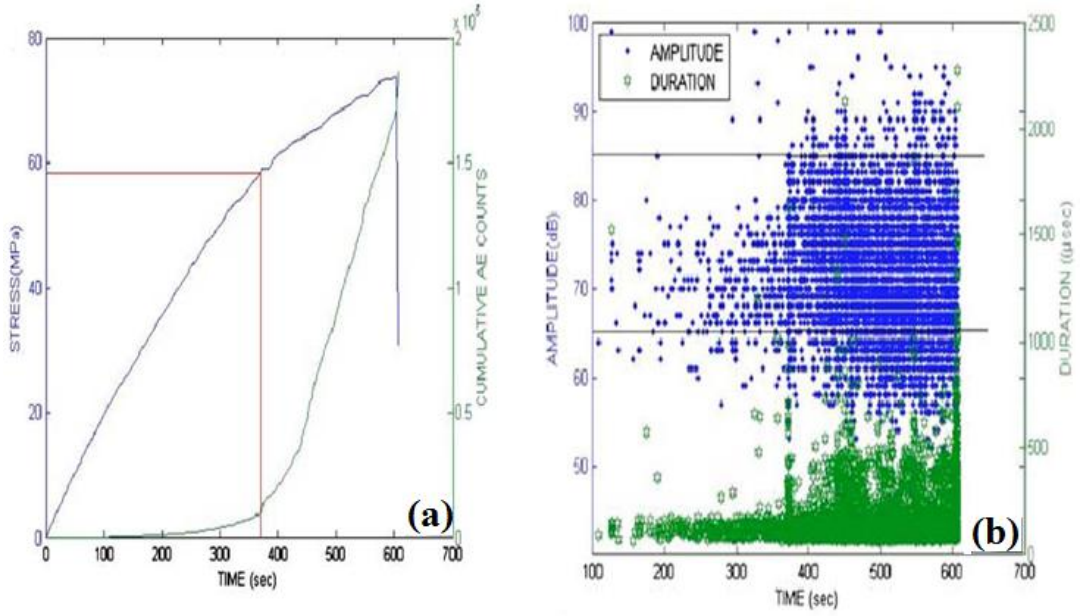

Figure 4.2. Mechanical and AE response of a laminated specimen: (a) Cumulative counts and (b) variation of amplitude and duration data [81].

Asokan *et al*. [83] claimed that evaluating acoustic emission (AE) data according to amplitude and duration parameters might help to identify failure modes. It was proposed that while matrix cracking generated short waves in low ranges, strong delamination generated long waves in higher ranges. The proposed classification chart is given in Table 4.2.

In 2014, Masmoudi *et al.* [75] performed tension tests of unidirectional and cross-ply laminates fabricated by hand lay-up process from glass fibers and epoxy resin. After collecting the AE data, the classification of hits was made by using k-means methodology. This classification reveals the presence of four different failure modes. Figure 4.3 shows the distribution of amplitude parameter vs. time for a cross-ply laminate under tension test

where matrix cracking, fiber-matrix debonding, fiber breakage, and delamination corresponds to A, B, C, and D classes, respectively.

Table 4.2. Proposed failure modes according to the classification of AE data in terms of amplitude and duration parameters [83].

Zone	Amplitude [dB]	Duration [μs]	Proposed failure mode
1	45-65	<300	Weak matrix cracking
2	45-65	>300	Weak matrix cracking
3	65-80	<300	Weak fiber failure, strong matrix cracking
4	65-80	>300	Weak delamination, strong matrix cracking, some fiber failure
5	80-99	<300	Strong fiber failure, strong matrix cracking
6	80-99	>300	Strong delamination, strong matrix cracking, some fiber failure

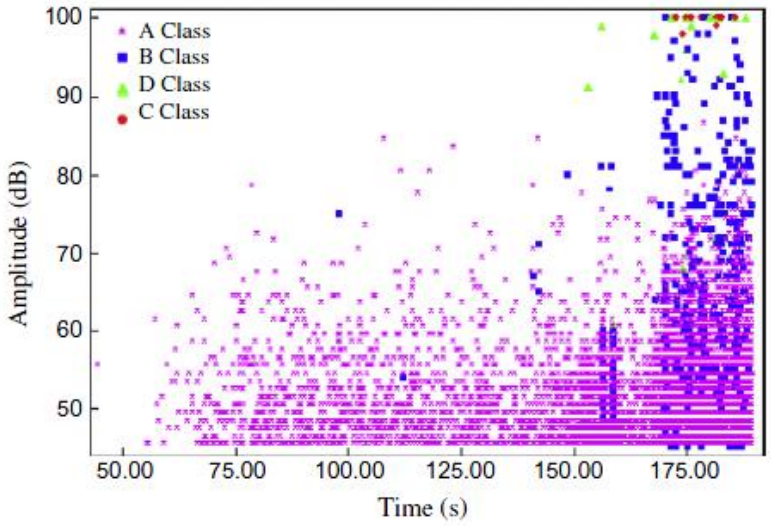

Figure 4.3. Amplitude distribution of the collected AE data after classification [75].

Figure 4.4 shows a detected waveform in time-domain and frequency-domain, taken from the studies of Aramugam *et al.* [73] on glass epoxy laminates. The piezoelectric transducer detects the wave motion on the surface and converts it into an electric signal,

which is represented in Figure 4.4a. Corresponding frequency-domain graph, which is represented in Figure 4.4b, clearly reveals the peak frequency of the signal.

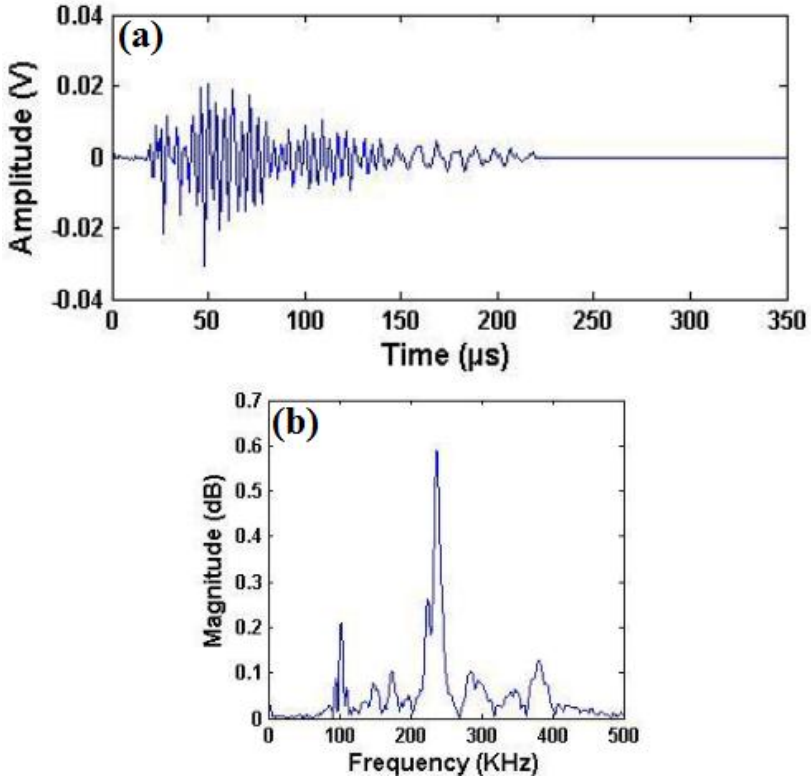

Figure 4.4. A detected waveform (a) in time domain and (b) in frequency domain [73].

Aramugam *et al.* [73] came to a conclusion that the peak frequency ranges 90-110 kHz and 130-200 kHz were related to matrix cracking and delamination for glass-epoxy laminates, respectively. He stated that the range between 230-250 kHz was a sign of debonding, while higher frequency content was observed for fiber failures.

Similarly, de Groot *et al.* [84] reported that for carbon-epoxy laminates, matrix cracking resulted in frequencies between 90-180 kHz while fiber failure was observed above 300 kHz. Debonding failure was expected to create a signal between 240-310 kHz.

Fotouhi *et al*. [85] investigated fracture mechanisms of glass/epoxy composites under quasi-static three point bending. AE waveforms were processed by wavelet packet techniques and integrated k-means technique. Fiber breakage, debonding and matrix cracking were observed as dominant failure mechanisms and corresponding frequency ranges were listed as 100-190 kHz, 200-320 kHz and 355-450 kHz, respectively.

Aramugam *et al*. [86] investigated mode I delamination of glass-fiber reinforced polymer laminates under acoustic emission monitoring. Each failure mode was identified by creating a correlation with FFT outputs, as seen in Figure 4.5.

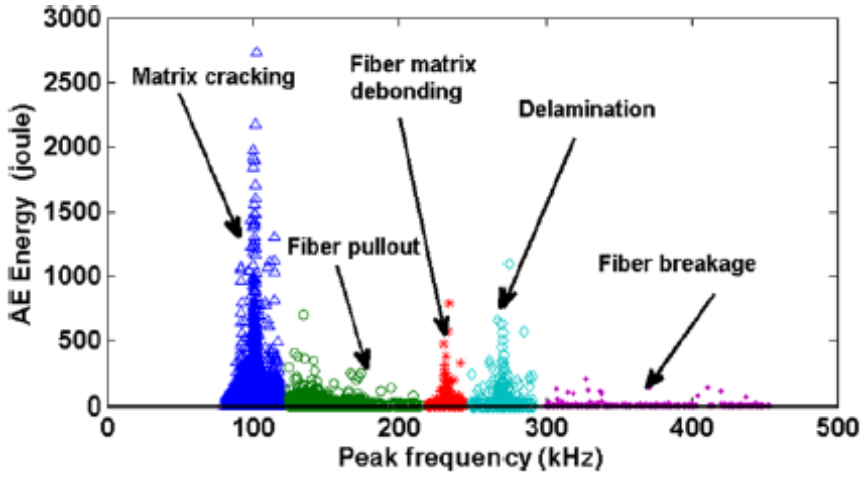

Figure 4.5. Classification of AE data for different failure modes [86].

5. TENSILE TESTS

The tension tests are performed using INSTRON 8801. Cross-ply and quasi-isotropic specimens are subjected to displacement controlled loading with the rate of 1 or 2 mm/min, respectively. INSTRON 8801 is a compact servo hydraulic fatigue testing system which is capable of performing various static and dynamic tests. The machine can apply loads up to 100 kN with 150 mm of usable stroke. The testing machine gets its power supply from an integrated hydraulic power unit, INSTRON 3520, which has 207 bars of operating pressure and 24.8 HP of engine [87].

Tension specimens have to be attached to the grips of the testing machine carefully since any possible misalignment may lead to undesired bending effects on the specimen. A proper part installation (Figure 5.1a) is followed by placing the external extensometer (Figure 5.1b) which measures the strain and sends the data to the controlling unit.

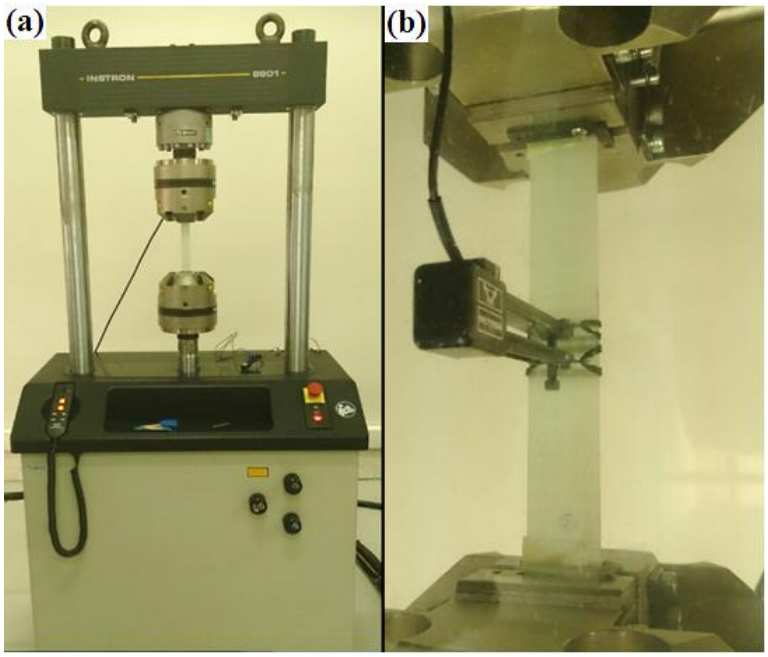

Figure 5.1. (a) A properly placed specimen and (b) an external extensometer.

Bluehill^{TM} is the software which controls the testing machine. Before running the test, the dimensional properties of the mounted specimen are entered to the software by the

operator. After running the test, the software starts saving the real-time data such as load, stress, and extension with desired intervals.

After the specimen is placed in the grips of INSTRON 8801, the acoustic emission transducers are placed on the surface of the tension specimens by using clamps (Figure 5.2). To prevent any damage on the sample and highly sensitive transducers, thick rubber bands are placed carefully. Before placing the transducer on the surface of the specimen, ultrasonic gel is applied on the interface. The gel layer creates a continuous medium between the surface and the transducers for the benefit of acquisition. The data acquisition for AE system is achieved by AEwin^{TM} software.

AE monitoring is done by four-channel system provided by Physical Acoustics Corporation. The sampling rate is selected as five mega sample per second. Two PK15I piezoelectric transducers are used for the signal detection. The integrated amplifier is set to 26 dB. For these wide band sensors, a broad frequency range is chosen as 20 kHz – 1 MHz for the acquisition. To filter the noises, 45 dB is taken as the threshold value. Peak definition time, hit definition time, and hit lockout time are selected as 50, 100, and 300 micro seconds, respectively.

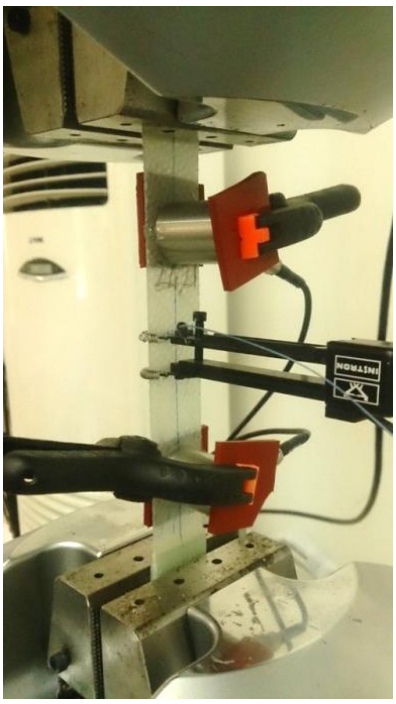

Figure 5.2. Installation of piezoelectric transducers.

5.1. Tension Tests

Each specimen is subjected to tensile loading until failure occurs. The data of each set are gathered separately and saved under different files.

ASTM D3039 standard classifies failure modes according to the failure type, area, and location; see Appendix D. Figure 5.3 shows the cross-ply specimens cut from $[0/90]_{2s}$ plate. From left to right, the specimens are numbered as 1, 2, 3, 4, and 5, respectively. Corresponding failure codes for specimens from 1 to 5 are LGM. L stands for lateral, indicating the failure mode; G stands for gage, indicating the failure area; M stands for middle, indicating failure location.

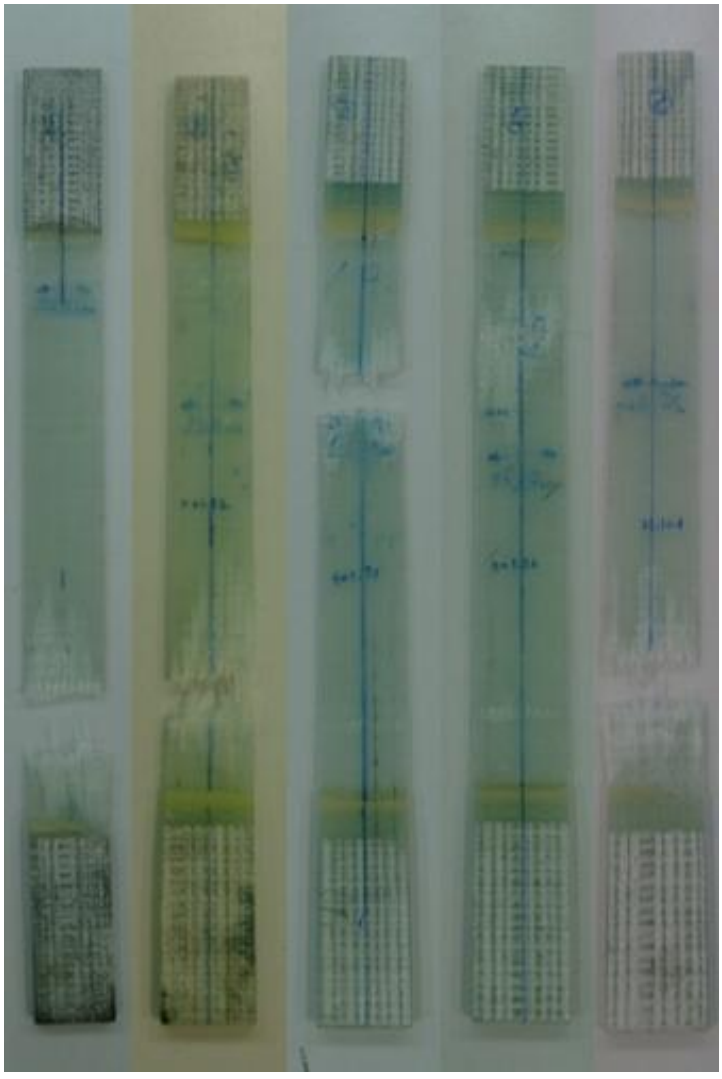

Figure 5.3. Failed cross-ply specimens.

Figure 5.4 shows the quasi-isotropic specimens cut from $[0/45/-45/90]_s$ plate. From left to right, the specimens are numbered as 6, 7, 8, 9, and 10, respectively. For 6 and 7 the failure code is AGM. A stands for angled, indicating the failure mode. G stands for gage, indicating the failure area. M stands for middle, indicating failure location. For 8 and 9 it is MGM. First M stands for multi-mode, indicating the failure mode. G stands for gage, indicating the failure area. Second M stands for middle, indicating failure location. For 10 it is LGM. L stands for lateral, indicating the failure mode. G stands for gage, indicating the failure area. M stands for middle, indicating failure location.

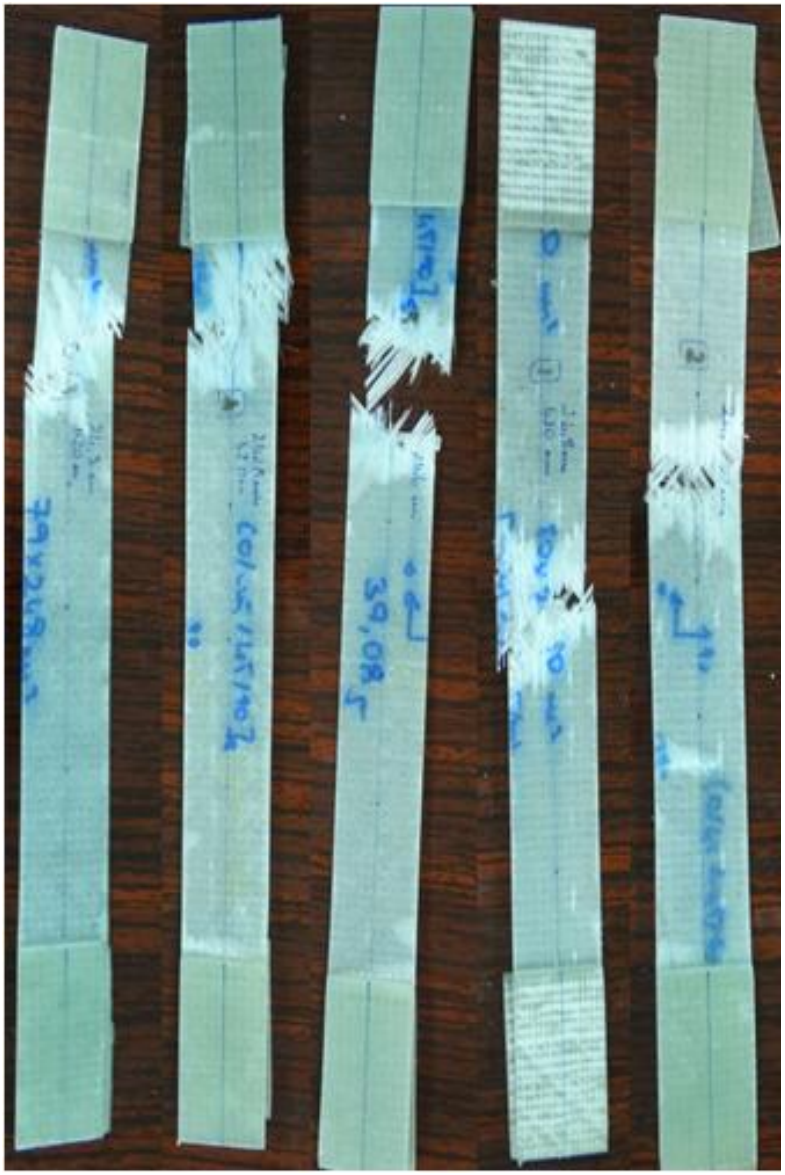

Figure 5.4. Failed quasi-isotropic specimens.

5.2. Test Results

For the cross-ply specimens, the corresponding load-strain curves are shown in Figure 5.5.

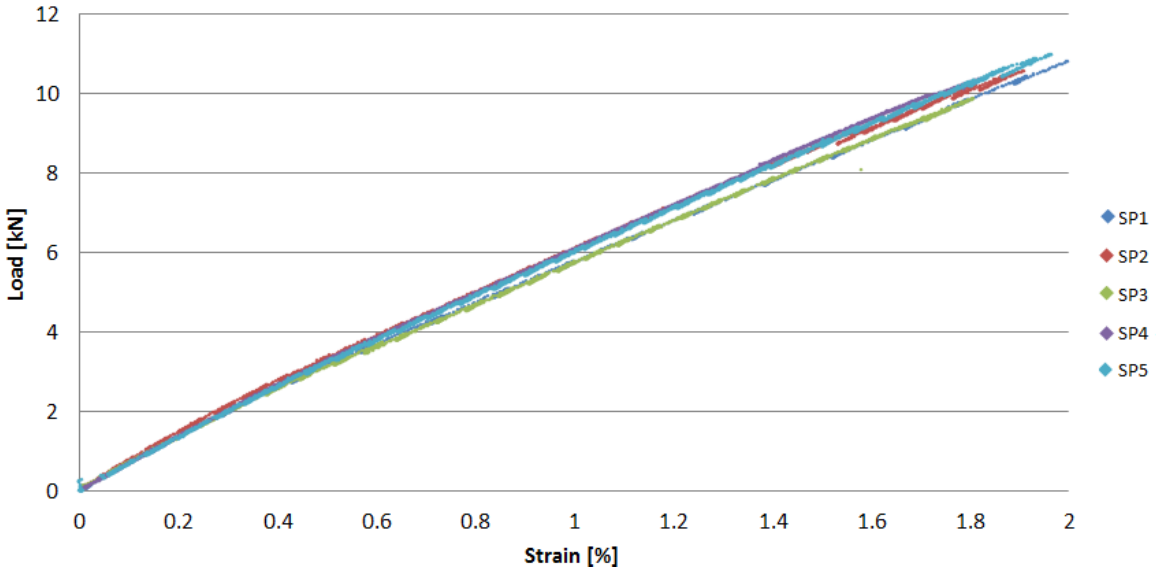

Figure 5.5. Load vs. strain curves for the cross-ply specimens.

When fiber-reinforced composite structures are subjected to in-plane loads, their load bearing capacities are high. On the other hand, they usually exhibit brittle fracture characteristics as seen in Figure 5.5. While the load is gradually increased, somewhat linear stress-strain curve is obtained up to the point where specimen suddenly fails.

The cross-ply specimens fail when the strain reaches 0.018-0.02 mm/mm level. The load at fracture exceeds 10 kN. These results agree with the ones reported in the study of Aramugam *et al.* [83].

Load vs. strain curves for quasi-isotropic specimens are presented in Figure 5.6. Compared to cross-ply specimens, quasi-isotropic specimens fail at lower loads while reaching higher strain values as expected. While four plies are aligned along the tension direction in the cross-ply specimens, only two plies are aligned in the quasi-isotropic specimens; the other two plies lie along 45^{o} and -45^{o} directions and this results in higher strain levels.

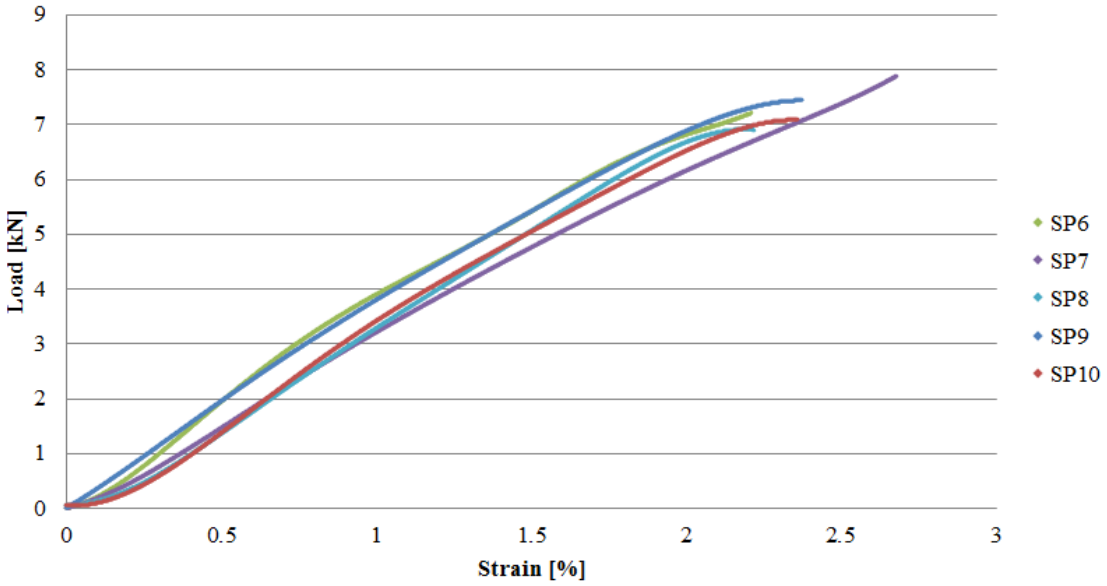

Figure 5.6. Load vs. strain curves for the quasi-isotropic specimens.

From the two plots in Figures 5.5 and 5.6, one may get the impression that fiber-reinforced polymers fail in an instant without giving any warning. However, this is not true. An observer may not be able to see the signs of activated failure mechanisms, but this does not mean that the structure undergoes no damage until catastrophic failure occurs. Figures 5.7 and 5.8 present the AE data for the specimens 4 and 9 in time domain, respectively. During the real-time acoustic emission monitoring, two transducers detect 9084 acoustic waves for the cross-ply specimen and 8836 acoustic waves for quasi-isotropic specimen. AEwin™ software calculates the corresponding hit parameters, including amplitude values in the scale of dB.

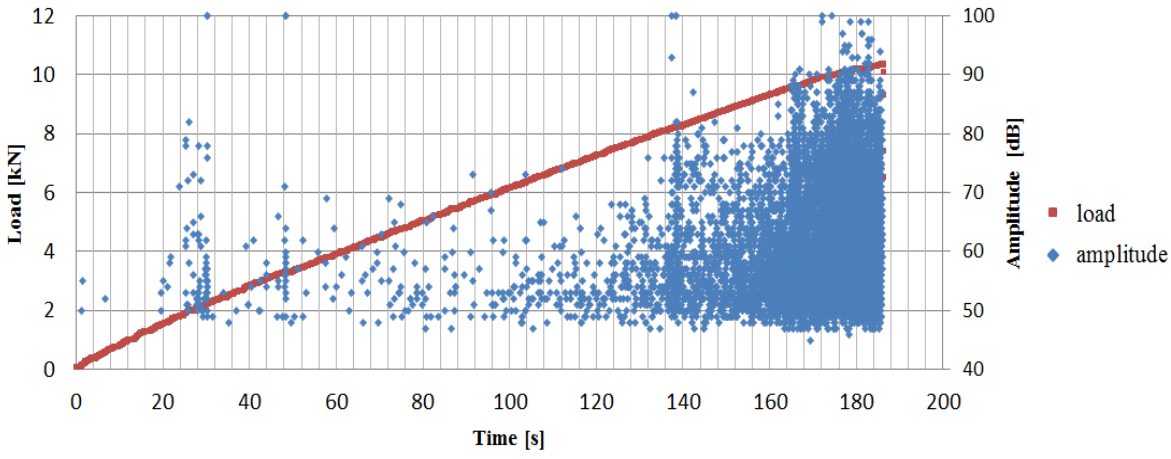

Figure 5.7. AE data of cross-ply specimen.

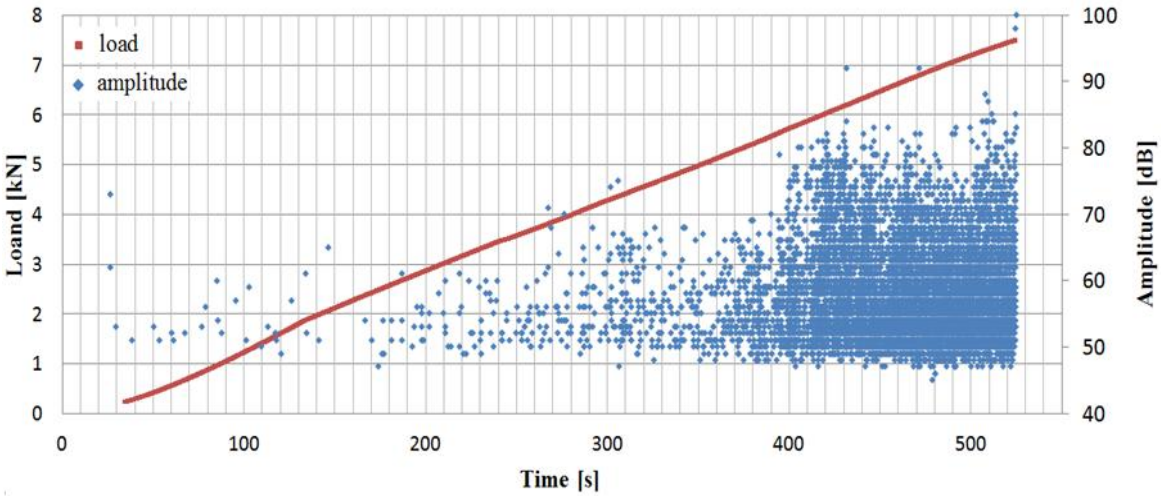

Figure 5.8. AE data of quasi-isotropic specimen.

Table 5.1. Number of detected hits.

Specimen ID	Number of AE Hits
1	6636
2	15801
3	8303
4	9084
5	13343
6	7556
7	9697
8	6022
9	8836
10	4456

AE data include several parameters such as duration, count, energy, and rise time. The AE data for specimens 4 and 9 are plotted in Figures 5.9, 5.10, and 5.11. From these four plots, one can infer that although cross-ply structure resists forces above 10 kN without giving any visible warning, the transducers start to detect high amounts of waves when the load exceeds about 8 kN. Similarly, while quasi-isotropic specimens resist forces above 7 kN, intense acoustic data activity starts when the load exceeds 6 kN. As discussed in AE Section, there are various methods to classify these AE data and correlate with failure mechanisms. Figure 5.13 reveals that different specimens have quite similar behavior.

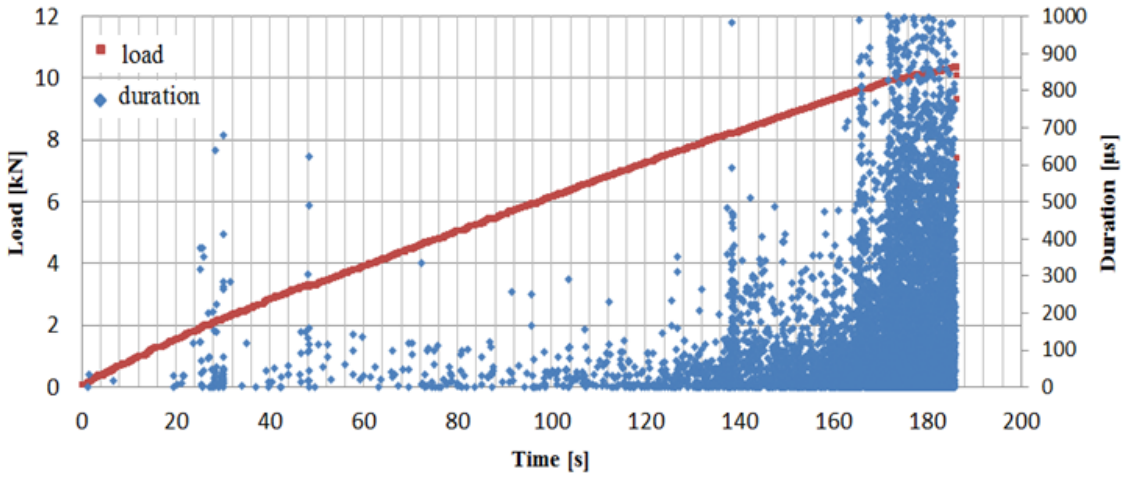

Figure 5.9. Load and duration vs. time for the cross-ply specimen 4.

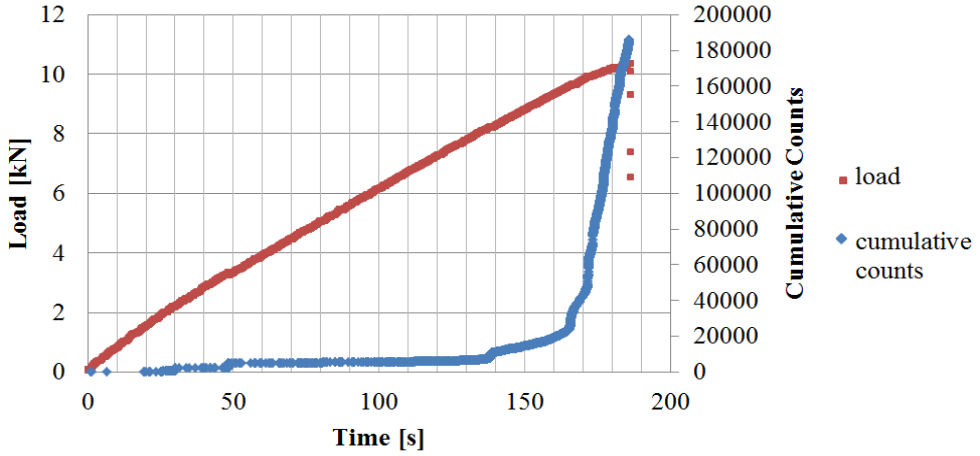

Figure 5.10. Load and duration vs. time for the quasi-isotropic specimen 9.

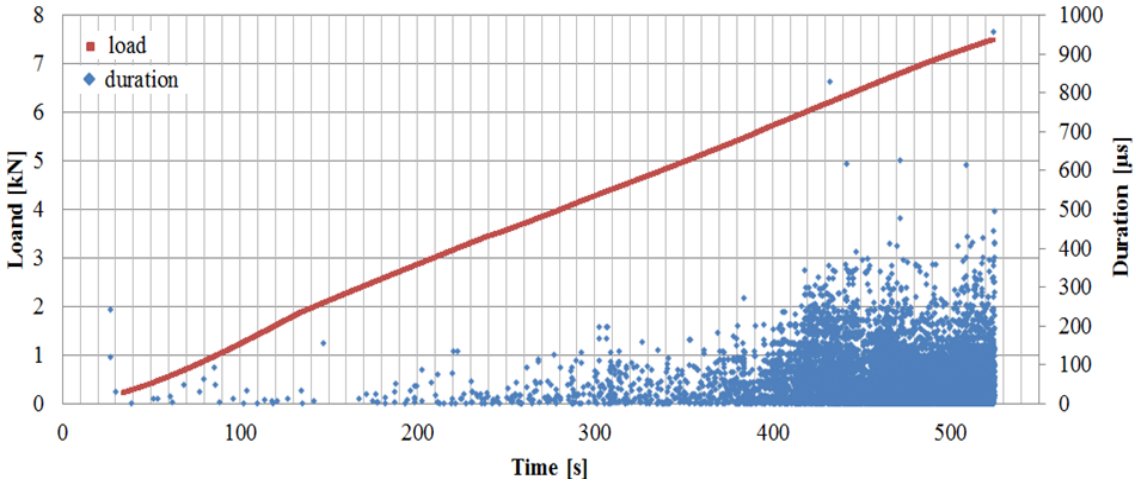

Figure 5.11. Load and cumulative counts vs. time for the cross-ply specimen 4.

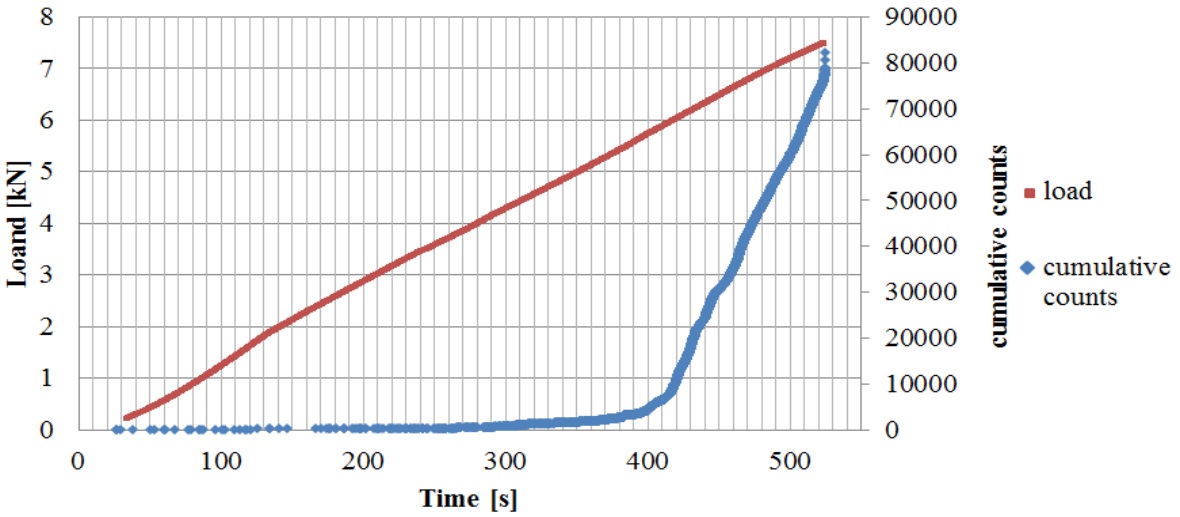

Figure 5.12. Load and cumulative counts vs. time for the quasi-isotropic specimen 9.

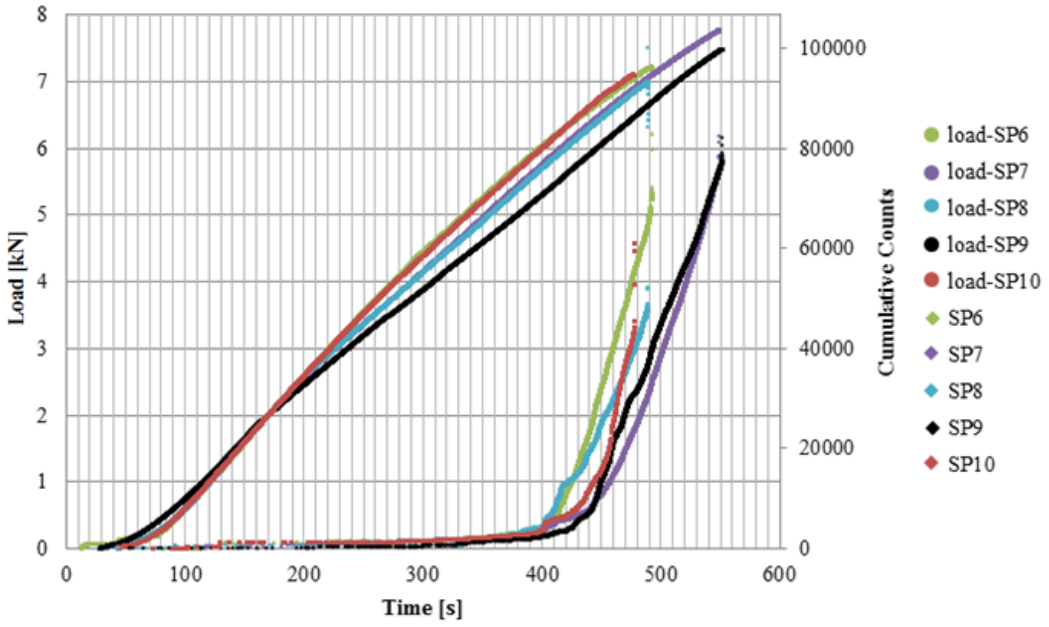

Figure 5.13. Cumulative counts and load vs. time for the quasi-isotropic specimens.

According to Aramugam *et al.* [83], if the value of the amplitude parameter is lower than 65 dB and the duration parameter is lower than 300 μs, the corresponding hit belongs to mode I. If the value of the amplitude parameter is lower than 65 dB and the duration parameter is higher than 300 μs, the corresponding hit belongs to mode II. If the value of the amplitude parameter is between 65 dB and 80 dB and the duration parameter is lower than 300 μs, the corresponding hit belongs to mode III. If the value of the amplitude parameter is between 65 dB and 80 dB and the duration parameter is higher than 300 μs,

the corresponding hit belongs to mode IV. If the value of the amplitude parameter is higher than 80 dB and the duration parameter is lower than 300 μs, the corresponding hit belongs to mode V. If the value of the amplitude parameter is higher than 80 dB and the duration parameter is higher than 300 μs, the corresponding hit belongs to mode VI. According to Aramugam *et al.* [83], mode I and mode II refer to weak matrix cracking; mode III refers to strong matrix cracking and weak fiber failure; mode IV implies weak delamination, strong matrix cracking and some fiber failure; mode V refers to strong fiber failure and strong matrix cracking. Finally, mode VI refers to strong delamination, strong matrix cracking and some fiber failure. Figures 5.14 and 5.15 show the distribution of the amplitude parameter for specimen 4 and 9 after applying the methodology of Aramugam *et al.* [83]. These measured acoustic data can be correlated with failure mechanisms and the failure behavior of a laminated structure can be evaluated. As discussed in Acoustic Emission Monitoring Section, each failure mechanism generates characteristic acoustic waves. Several techniques have been developed in order to correlate failure mechanisms with AE data, but it is not possible to create a distinct chart to classify them. Several researches proposed different ways to classify AE data. According to Laksimi *et al.* [79], 45-58 dB range refers to matrix/matrix friction; 58-68 dB range identifies debonding; 68-86 dB range refers to matrix/fiber friction and 86-100 dB range refers to fiber breakage. Figures 5.16 and 5.17 show the distribution of the amplitude parameter after applying the methodology of Laksimi *et al.* [79].

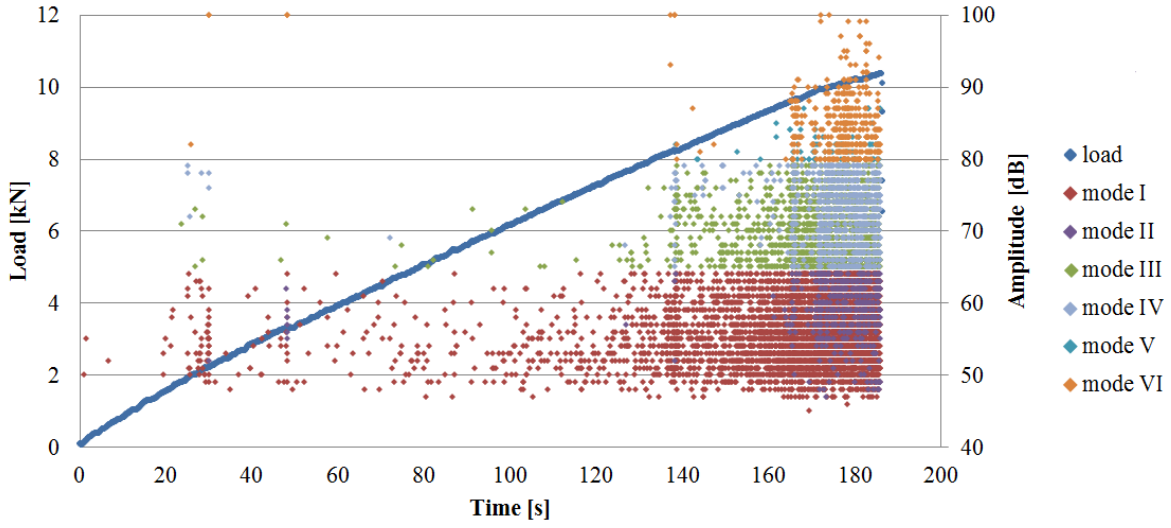

Figure 5.14. Classification of the AE data for cross-ply specimen 4 according to Aramugam *et al.* [83].

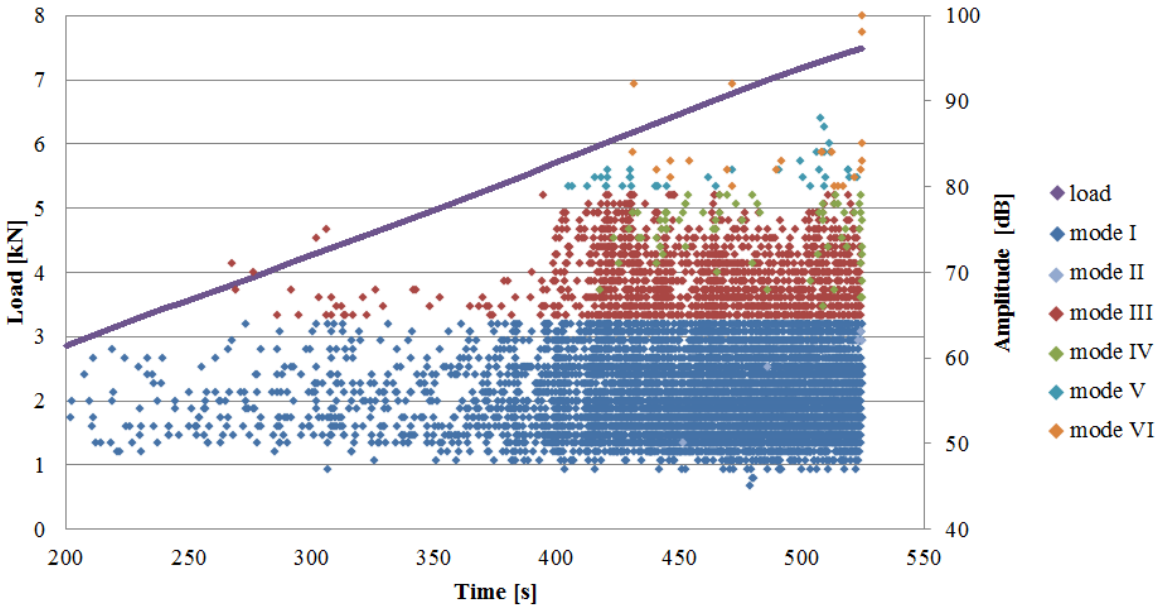

Figure 5.15. Classification of the AE data for quasi-isotropic specimen 9 according to Aramugam *et al.* [83].

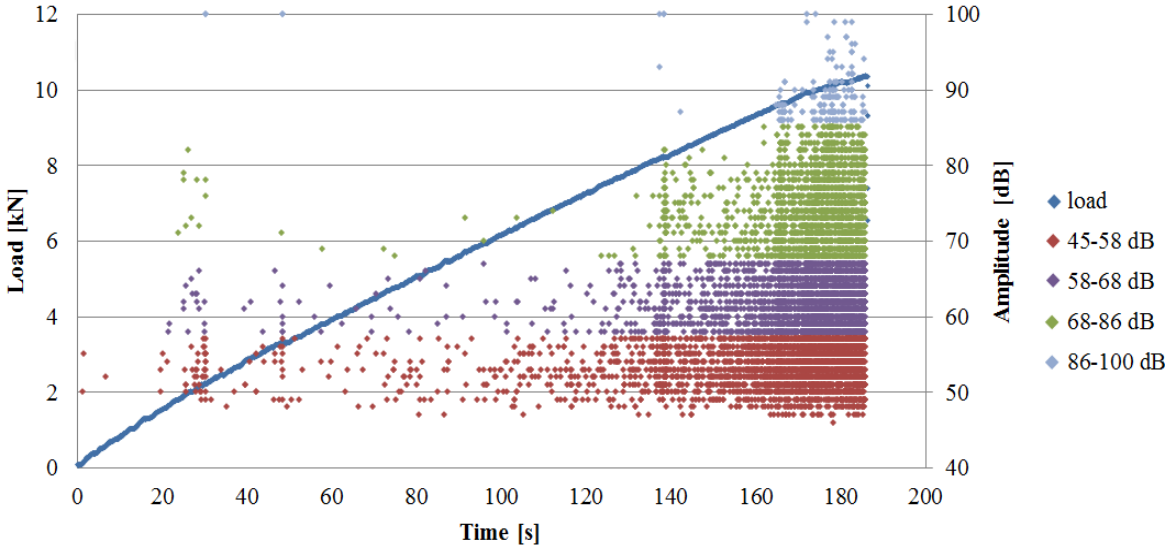

Figure 5.16. Classification of the AE data for cross-ply specimen 4 according to Laksimi *et al.* [79].

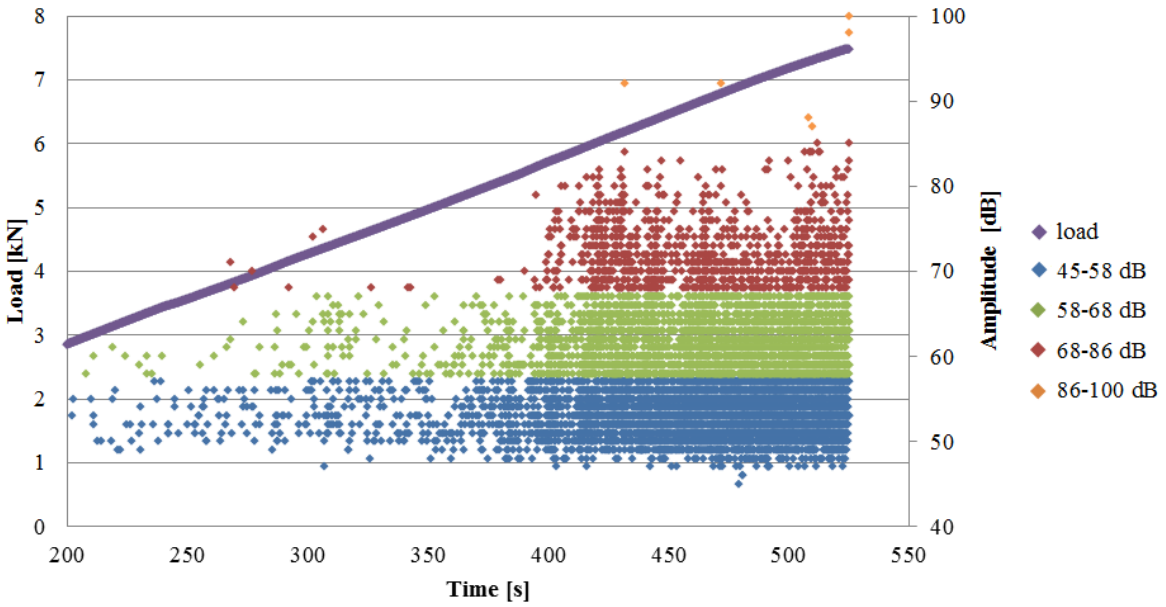

Figure 5.17. Classification of the AE data for quasi-isotropic specimen 9 according to Laksimi *et al.* [79].

Because classification of AE data according to failure mode is highly dependent on the type of reinforcement and matrix materials, the final judgment regarding the failure behavior should not solely based on parameter-based techniques. Evaluation of the AE data in FFT spectrum may give more reliable results. For FFT evaluation, it is known that higher dominant frequency values are obtained when a more critical damage occur. Figure 5.18 shows the peak frequency distribution for quasi-isotropic specimen 9. By observing the peak frequency plot in Figure 5.18, it is possible to come up with a conclusion that while 140-160 kHz band corresponds to matrix cracking, 180-230 kHz band and 230-270 kHz band correspond to delamination or debonding. Fiber breakage occurs at much higher frequencies, at 350-370 kHz band [73]. Failure mechanisms are expected to get activated in the order of matrix cracking, interfacial debonding, delamination and fiber breaking when a fiber-reinforced laminate is subjected to a gradually increasing tensional load [88] (Figure 5.19). Since the transducers start detecting AE data on 230-270 kHz band before 180-230 kHz band, one may assume that 180-230 kHz band and 230-270 kHz band should correspond to delamination and debonding, respectively. Hits obtained at 150 kHz in the earlier stages of the experiment should correspond to matrix micro cracking. This occurs at about 2-3 kN. They evolve to matrix cracking while the load reaches 3-5 kN range. However, they do not affect the mechanical behavior of the quasi-isotropic specimen. On

the other hand, critical matrix failure is started at 5 kN and the corresponding load level can be accepted as the first ply failure load for the quasi-isotropic specimens. It is followed by fiber-resin debonding and delamination at 5.5-6 kN. When the load exceeds 6.5 kN, critical fiber breakage failure mechanism is activated. Corresponding peak frequency is 360 kHz. For the quasi-isotropic specimens, the initial fiber failures at 6.5 kN are expected to have occurred in the laminae where fibers are aligned with the tension direction.

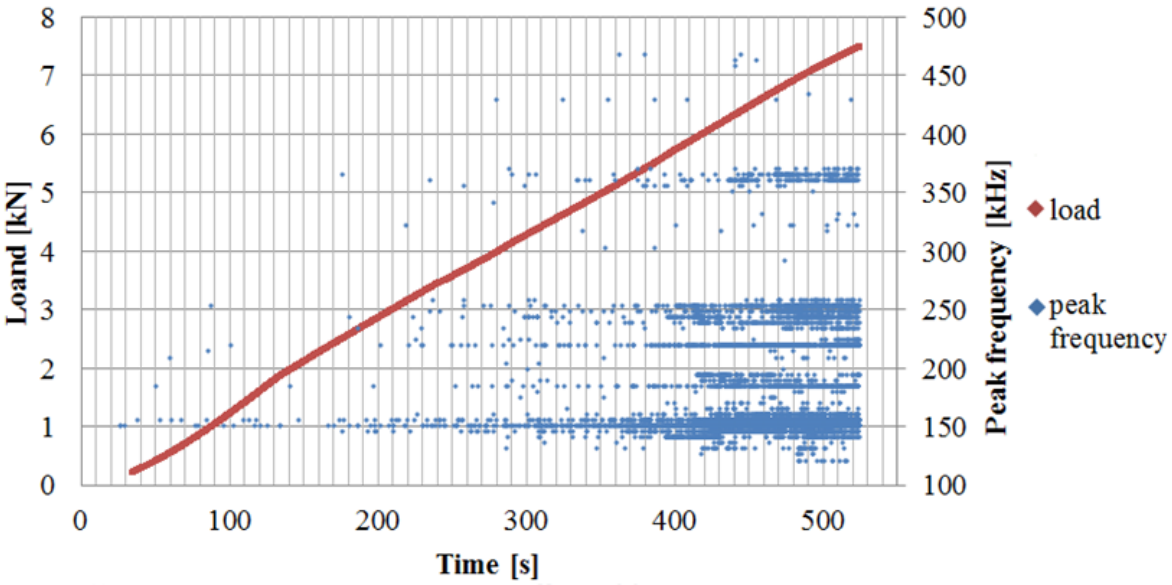

Figure 5.18. Load and peak frequency distribution for quasi-isotropic specimen 9.

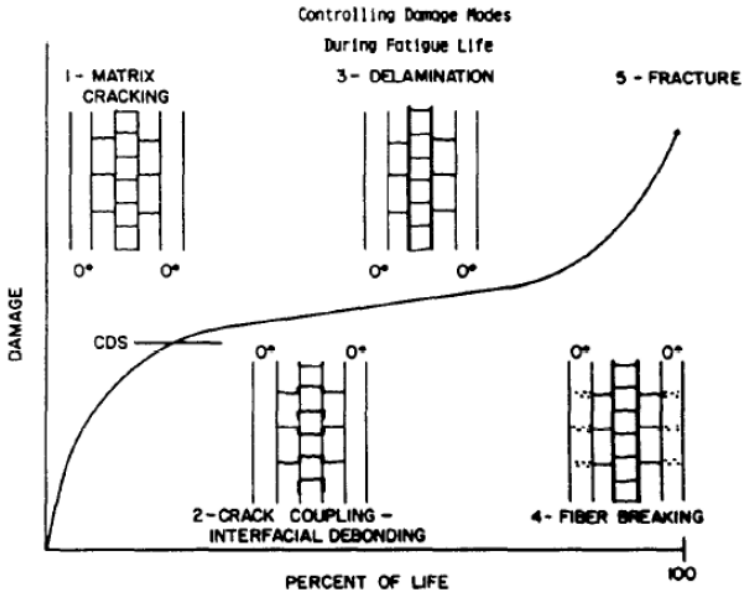

Figure 5.19. Activated damage mechanisms during the lifetime of a laminate [88].

Similarly, when the load reaches to 8 kN for the cross-ply specimens, the first ply failure occurs and when it reaches to 10 kN, the specimens get into an unstable zone due to extensive delamination. Above 10 kN fibers can no longer withstand the load and the specimen fails.

5.3. Extraction of Strength Values

In order to find the strength values via classical laminate theory, the lamina properties has to be calculated from micromechanics in the first place. From the measurements of the weight and the dimensions of the dry reinforcement and the tension specimens (Table 3.1), the volumetric fractions are calculated. The material properties of the reinforcing E-glass cloth and the epoxy resin are obtained from the manufacturers. From the rule of mixtures methodology (see Appendix B, Equations B.1-B.4), the mechanical properties of a transversely orthotropic lamina are found. Table 5.2 shows the calculated lamina properties for the cross-ply specimen 4.

Table 5.2. Material properties for a unidirectional lamina calculated based on micromechanics.

Volumetric fraction of fiber	0.51
Volumetric fraction of resin	0.49
E_1 [GPa]	38.2
E_2 [GPa]	6.2
ν_{12}	0.29
G_{12} [GPa]	2.3
ν_{23}	0.28
G_{23} [GPa]	2.4
ν_{21}	0.047

Once the lamina properties are found via the rule of mixtures methodology, the stiffness matrix of the lamina, [*Q*], is calculated (Appendix B, Equations B.5-B.10). The stiffness matrix defines the mechanical response of the lamina accepting the fiber direction as direction 1 and the transverse direction as direction 2. In order to transform the lamina stiffness matrix from the principal material coordinate system to the laminate global coordinate system for each lamina in the cross-ply specimen, Equations B.11-B.17 in Appendix B are used by setting the θ parameter to the lamina angle values. The θ

parameter indicates the angular difference between the global *x*-direction and the fiber direction. For the k[th] layer of the cross-ply specimen, Equation 5.1 describes its mechanical behavior.

$$\begin{bmatrix}\sigma_x\\ \sigma_y\\ \sigma_{xy}\end{bmatrix}_k = \begin{bmatrix}\bar{Q}_{11} & \bar{Q}_{12} & \bar{Q}_{16}\\ \bar{Q}_{12} & \bar{Q}_{22} & \bar{Q}_{26}\\ \bar{Q}_{16} & \bar{Q}_{61} & \bar{Q}_{66}\end{bmatrix}_k \begin{bmatrix}\varepsilon_x\\ \varepsilon_y\\ \gamma_{xy}\end{bmatrix}_k \tag{5.1}$$

Classical laminate theory enables defining the stress-strain relation and the mechanical behavior of each lamina in terms of mid-surface strains and curvatures of the laminate, as formulized in Equation 5.2.

$$\begin{bmatrix}\sigma_x\\ \sigma_y\\ \tau_{xy}\end{bmatrix}_k = \begin{bmatrix}\bar{Q}_{11} & \bar{Q}_{12} & \bar{Q}_{16}\\ \bar{Q}_{12} & \bar{Q}_{22} & \bar{Q}_{26}\\ \bar{Q}_{16} & \bar{Q}_{61} & \bar{Q}_{66}\end{bmatrix}_k \left[\begin{bmatrix}\varepsilon_x^0\\ \varepsilon_y^0\\ \gamma_{xy}^0\end{bmatrix} + z\begin{bmatrix}\kappa_x\\ \kappa_y\\ \kappa_z\end{bmatrix}\right] \tag{5.2}$$

At the tension tests, the strain and load data are recorded for the specimens. Thanks to the mid-plane symmetry, the curvature parameters in Equation 5.2 are equal to zero which gives Equation 5.3.

$$\begin{bmatrix}\sigma_x\\ \sigma_y\\ \tau_{xy}\end{bmatrix}_k = \begin{bmatrix}\bar{Q}_{11} & \bar{Q}_{12} & \bar{Q}_{16}\\ \bar{Q}_{12} & \bar{Q}_{22} & \bar{Q}_{26}\\ \bar{Q}_{16} & \bar{Q}_{61} & \bar{Q}_{66}\end{bmatrix}_k \begin{bmatrix}\varepsilon_x^0\\ \varepsilon_y^0\\ \gamma_{xy}^0\end{bmatrix} \tag{5.3}$$

If the thickness of a laminate is defined as *h*, it is convenient to define *N*, force per unit length, and *M*, moment per unite length with the following equations.

$$N_{\alpha\beta} = N_{\beta\alpha} = \int_{-\frac{h}{2}}^{\frac{h}{2}} \sigma_{\alpha\beta} dz \quad \alpha, \beta = 1, 2 \tag{5.4}$$

$$M_{\alpha\beta} = M_{\beta\alpha} = \int_{-\frac{h}{2}}^{\frac{h}{2}} x_3 \sigma_{\alpha\beta} dz \quad \alpha, \beta = 1, 2 \tag{5.5}$$

For the tension tests, the specimens are not subjected to moments. For the force per unit length equation, the integral can be divided into parts to express the behavior of each layer separately by substituting Equation 5.3 into Equation 5.4. Therefore, *N* can be expressed in terms of mid-plane strains and transformed stiffness matrices of the structure (Equations 5.6 and 5.7).

$$[N] = \begin{bmatrix} N_{11} \\ N_{22} \\ N_{12} \end{bmatrix} = \sum_{k=1}^{N} \int_{z_{k-1}}^{z_k} \begin{bmatrix} \sigma_{11} \\ \sigma_{12} \\ \sigma_{22} \end{bmatrix}_k dz \tag{5.6}$$

$$[N] = \left\{ \sum_{k=1}^{N} [\bar{Q}]_k \int_{z_{k-1}}^{z_k} dz \right\} [e] \tag{5.7}$$

For the simplicity, Equation 5.7 can be written as following:

$$\begin{Bmatrix} N_x \\ N_y \\ N_{xy} \end{Bmatrix} = \begin{bmatrix} A_{11} & A_{12} & A_{16} \\ A_{12} & A_{22} & A_{26} \\ A_{16} & A_{26} & A_{66} \end{bmatrix} \begin{Bmatrix} \varepsilon_x^0 \\ \varepsilon_y^0 \\ \gamma_{xy}^0 \end{Bmatrix} \tag{5.8}$$

where;

$$A_{ij} = \sum_{k=1}^{N} \left(\bar{Q}_{ij}\right)_k (z_k - z_{k-1}) \tag{5.9}$$

Equation 5.8 describes the mechanical behavior of multi-directional laminates with mid-plane symmetry under in-plane tension loads. The thickness of the cross-ply specimens are measured as 1.35 mm. For 0^o and 90^o laminae, the calculated values of [*Q*] are tabulated in Table 5.3.

Table 5.3. [*Q*] of 0^o and 90^o laminae for the cross-ply specimen.

[*Q*] for 0^o laminae [MPa]			[*Q*] for 90^o laminae [MPa]		
38740.5	1816.6	0	6282.4	1816.6	0
1816.6	6282.4	0	1816.6	38740.5	0
0	0	2283.3	0	0	2283.3

From the tension test data, mid-plane strain values for each stress level are recorded. Thanks to the mid-plane symmetry, the strain remains the same through the thickness since no curvature occurs. By using Equation 5.9 with the calculated values of $\bar{Q}_{ij}$, the elements of [A] are calculated for the cross-ply specimen (Equation 5.10).

$$[A]_{specimen\ 4} = \begin{bmatrix} 30615.5 & 2470.58 & 0 \\ 2470.58 & 30615.5 & 0 \\ 0 & 0 & 3105.33 \end{bmatrix} \tag{5.10}$$

Figure 5.20 shows a comparison of the analytical and test results regarding load-strain relation. If the strain data of the tension test are taken as input, the calculated [A] for the cross-ply specimen (Equation 5.10) allows to predict the load curve via Equation 5.8. In order to obtain the analytical load vs. strain curve, firstly, [A] of the cross-ply specimen four (Equation 5.10) is substituded in Equation 5.8. For the uniaxial tension test of the cross-ply specimen with the mid-plane symmetry condition, N_y, N_{xy}, and γ_{xy}^0 are equal to zero which gives the simplified version of Equation 5.8 (Equation 5.11). ε_x^0 is the recorded strain data for the cross-ply specimen during the tension test and is a known parameter. These two equations in Equation 5.11 with two unknowns, N_x and ε_y^0, are solved analytically which gives the corresponding the N_x value for each strain value. When N_x is multiplied by the width of the specimen, 25 mm, the predicted applied load for the cross-ply specimen is calculated.

$$\begin{Bmatrix} N_x \\ 0 \end{Bmatrix} = \begin{bmatrix} 30615.5 & 2470.58 \\ 2470.58 & 30615.5 \end{bmatrix} \begin{Bmatrix} \varepsilon_x^0 \\ \varepsilon_y^0 \end{Bmatrix} \tag{5.11}$$

The predicted load-strain curve should coincide with actual load-strain curve. Actually, due to the viscoelastic deformation of the epoxy resin, only the initial parts of the two curves match because the resin is assumed to be a linear elastic material in the analytical model and therefore viscoelastic effects are not considered. For this reason, the actual data deviate from the predicted curve after 0.005 mm/mm strain value as seen in Figure 5.20. Considering that the error is tolerable, Young's modulus, shear modulus and Poisson's ratios calculated based on micromechanics are accepted as lamina properties.

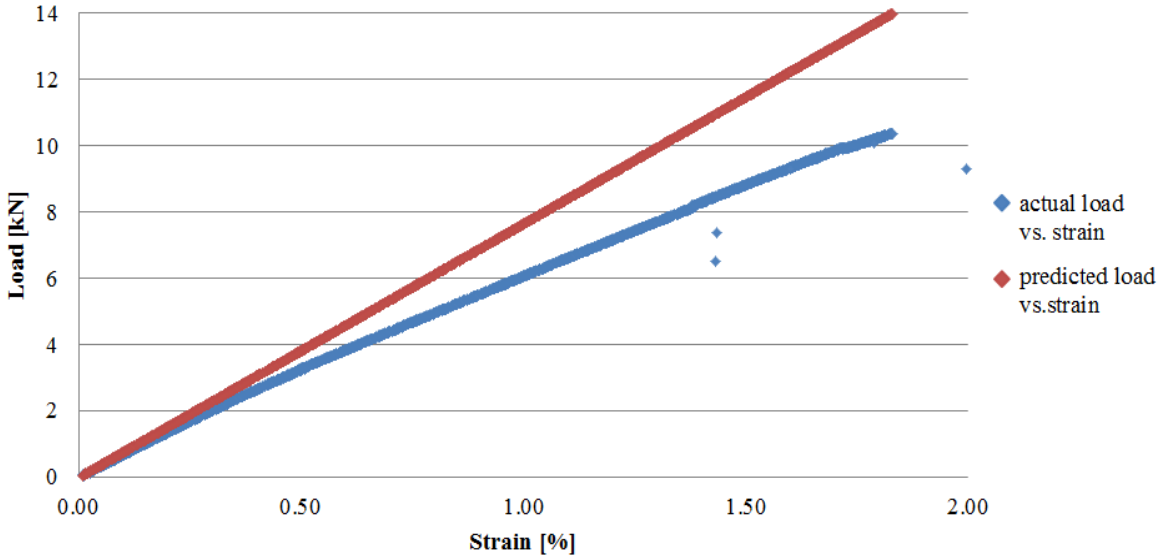

Figure 5.20. Actual load and the predicted load vs. strain curves for cross-ply specimen 4.

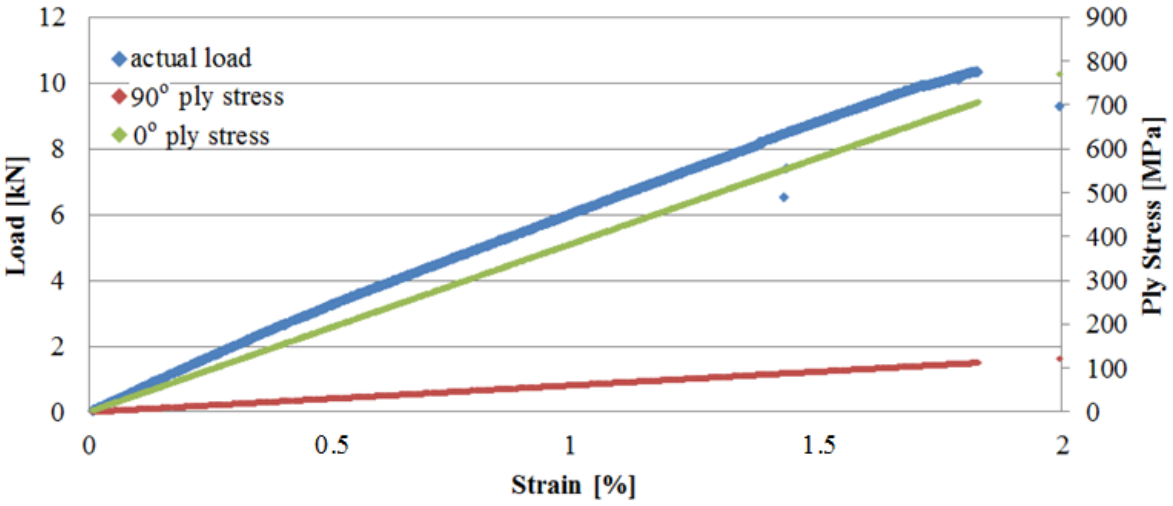

Figure 5.21. Actual load and the predicted ply stress vs. strain curves for cross-ply specimen 4.

The same methodology is also followed for the quasi-isotropic specimen 9 and its [A] is calculated as

$$[A]_{specimen\ 9} = \begin{bmatrix} 18188.9 & 5723.37 & 0 \\ 5723.37 & 18188.9 & 0 \\ 0 & 0 & 6232.75 \end{bmatrix} \tag{5.12}$$

Firstly, [A] of the quasi-isotropic specimen nine (Equation 5.12) is substituded in Equation 5.8. For the uniaxial tension test of the quasi-isotropic specimen with the mid-plane symmetry condition, N_y, N_{xy}, and γ_{xy}^0 are equal to zero which gives the simplified version of Equation 5.8 (Equation 5.13). ε_x^0 is the recorded strain data for the quasi-isotropic specimen during the tension test and is a known parameter. These two equations in Equation 5.13 with two unknowns, N_x and ε_y^0, are solved analytically which gives the corresponding N_x and ε_y^0 values for each ε_x^0 value. When N_x is multiplied by the width of the specimen, 24.7 mm, the predicted applied load for the quasi-isotropic specimen is calculated. Figure 5.22 shows the actual load and the predicted load vs. strain curves for quasi-isotropic specimen 9. Similar to the cross-ply specimen, a good agreement between the prediction and the actual data is observed.

$$\begin{Bmatrix} N_x \\ 0 \end{Bmatrix} = \begin{bmatrix} 18188.9 & 5723.37 \\ 5723.37 & 18188.9 \end{bmatrix} \begin{Bmatrix} \varepsilon_x^0 \\ \varepsilon_y^0 \end{Bmatrix} \tag{5.13}$$

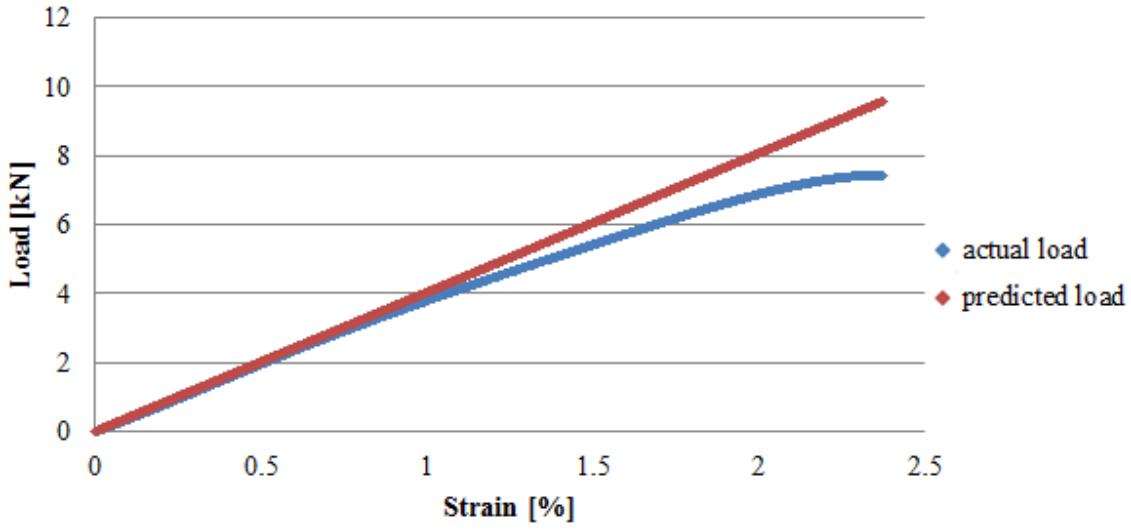

Figure 5.22. Actual load and the predicted load vs. strain curves for quasi-isotropic specimen nine.

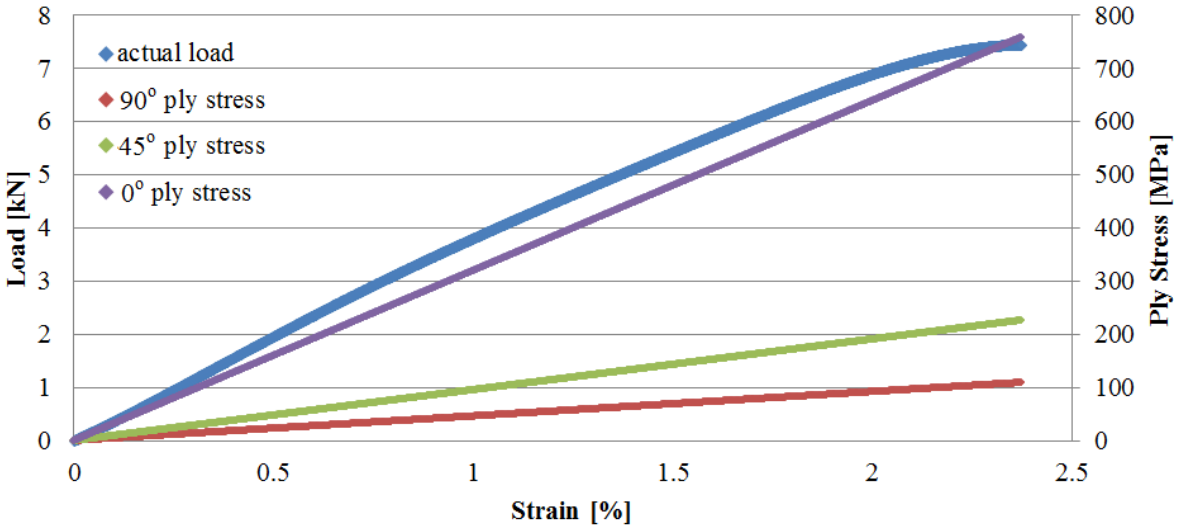

Figure 5.23. Actual load and the predicted ply stress vs. strain curves for quasi-isotropic specimen 4.

Figures 5.20 and 5.22 show the predicted load vs. strain curves for the cross-ply and quasi-isotropic specimens. These prediction curves can be used to calculate transverse tensile strength. The stress state developed in each lamina of the cross-ply specimens at 8 kN load is calculated. The weakest lamina is the one oriented perpendicular to the tension direction, because the strength of a lamina in transverse direction is much lower than the strength in the fiber direction. Therefore, the first signals should correspond to the failure of 90^o laminae in tension. The corresponding stress level is then the transverse tensile strength of the lamina. Similarly, the failure behavior of the quasi-isotropic specimens is examined. When the load reaches 5 kN, the critical matrix failure is observed from the AE data (150 kHz band). These signals should correspond to the failure of 90^o laminae in tension. The corresponding stress level is then the transverse tensile strength of the lamina. By using the measured ε_x^0 strain values and the calculated (Equations 5.11 and 5.13) ε_y^0 strain values, the corresponding stress states of the cross-ply and the quasi-isotropic specimens are calculated through Equation 5.3. The transverse tensile strength of the lamina is found as 79 MPa for the cross-ply specimen and 68 MPa for the quasi-isotropic specimen. When the load exceeds 10 kN for the cross-ply specimen, the strongest parts of the structure fail and this leads to fracture. Therefore, the corresponding stress should be the longitudinal tensile strength. When the load exceeds 6.5 kN for the quasi-isotropic specimen, the strongest parts of the structure fail (AE signals on 360 kHz band, indicating fiber failure), and the corresponding stress level should be the longitudinal tensile strength.

When the first ply failure occurs, the load bearing capability of that ply decreases dramatically, which changes the mechanical respond of the laminate structure and also the stress states at each laminae. In order to find the stress states, the matrix cracking in the transverse laminae has to be taken into consideration. The matrix cracking in the transverse laminae decreases the transverse properties strikingly. On the other hand, their load bearing capabilities in fiber direction still remain. Therefore, E_2 and G_{12} of these laminae are decreased to %15 of their initial values. With the updated properties, [A] of the cross-ply and quasi-isotropic specimens are calculated again and used to predict load vs. strain curves. Figure 5.24 depicts the updated prediction of load vs. strain curve for the quasi-isotropic specimen.

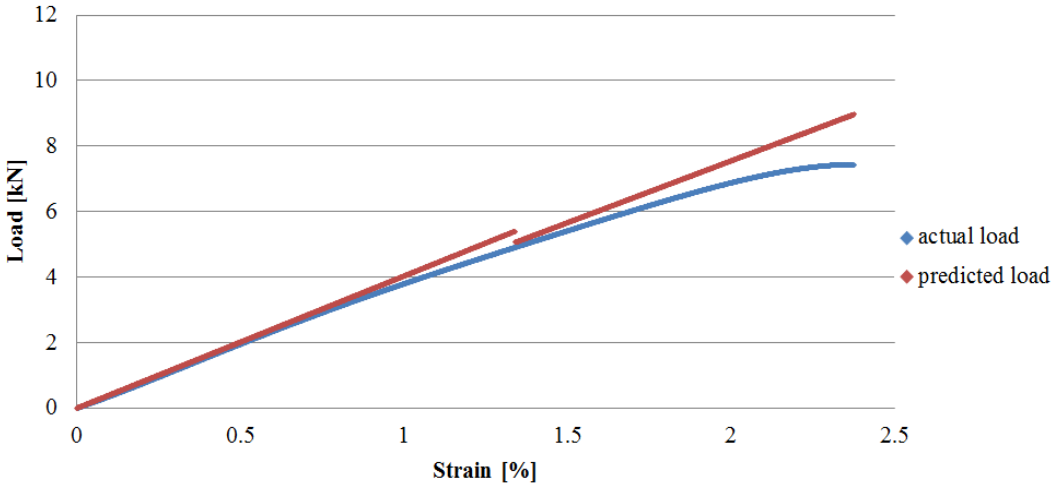

Figure 5.24. The updated prediction of load vs. strain curve for the quasi-isotropic specimen nine.

By using the measured ε_x^0 strain values and the calculated (Equations 5.11 and 5.13) ε_y^0 strain values, the stress states of the cross-ply and the quasi-isotropic specimens are calculated through Equation 5.3. The longitudinal tensile strength of the lamina is found as 671 MPa for the cross-ply specimen and 622 MPa for the quasi-isotropic specimen.

Table 5.4. shows the calculated longitudinal and transverse tensile strength values for a unidirectional lamina for the cross-ply specimen 4 and the quasi-isotropic specimen 9. As seen in Table 5.4, the agreement in the results obtained using two different stacking sequences is acceptable. Therefore, one may assume the the longitudinal tensile strength of

a single lamina is 650 MPa, and the transverse tensile strength of a single lamina is 75 MPa. For the other required material properties, literature sources are used to find a match with the material used in this study. Unfortunately, it is not possible to find an exact match in the literature. On the other hand, from the studies of Fereidoon *et al.* [12], and Makris *et al*. [89], the longitudinal compressive strength is decided to be taken as 600 MPa, the transverse compression strength as 120 MPa, and shear strength as 60 MPa. One should note that although the calculated mechanical properties via micromechanics and the calculated strength properties via experiments are sufficient enough for the FE studies in this study, a slightly mismeasured specimen dimension or weight can change the calculated properties easily. The adopted values for the missing material data may lead to erroneous predictions, too. For the further studies, more sensitive measuring of dimensions and weights is advised and the missing mechanical property values for the laminate in this study should be found via conducting proper experiments. In addition to Table 5.2, which lists some of the lamina properties including Young's modulus, shear modulus and Poisson's ratios; Table 5.5 lists the strength properties for the unidirectional lamina.

Table 5.4. Calculated longitudinal and transverse tensile strength values for a unidirectional lamina.

	Specimen 4	Specimen 9
Longitudinal Tensile Strength of Lamina [MPa]	671	622
Transverse Tensile Strength of Lamina [MPa]	79	68

Table 5.5. The strength properties for the unidirectional lamina.

Longitudinal Tensile Strength [MPa]	650
Longitudinal Compressive Strength [MPa]	600
Transverse Tensile Strength [MPa]	75
Transverse Compressive Strength [MPa]	120
Shear Strength	60

6. FINITE ELEMENT MODELING OF THE SANDWICH STRUCTURE

In order to predict the failure load of the sandwich structure made of glass-fiber reinforced composite sheets and core under out-of-plane loading, a finite element model is developed in ABAQUS finite element software. The face sheets and core are modeled separately and assembled together. The boundary conditions of the model reflect the physical loading conditions in deflection controlled in three-point bending test. By using secant algorithm, the deflection at which failure occurs and the corresponding failure load are iteratively determined. The predicted region of failure, the deflection causing failure, and the corresponding reaction force are compared with physical test results in order to validate the model.

6.1. Parts

Sandwich composite structures have basically four different core types, which are honeycomb, truss, solid-foam and corrugated cores. However, it is possible to use another structural design for the core elements. For this study, a unique core structure is adopted. Figure 6.1 represents the unit cell for the core structure. The base area is 100 mm to 100 mm. The height is 10 mm and the top area is 50 mm to 50 mm. As a result, the angle between the surface and the side faces is equal to 21.8 degrees.

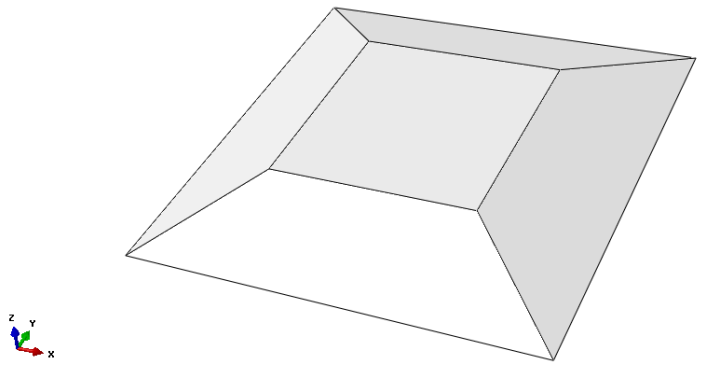

Figure 6.1. The unit cell for the core structure.

In the test specimens, nine of these unit cells are placed next to each other to create a 3x3 core structure. However, before merging these cells into a single part, five of them are flipped over. Merging is followed by introduction of fillet and addition of an outer frame as shown in Figure 6.2. Then shell elements are generated through the surface.

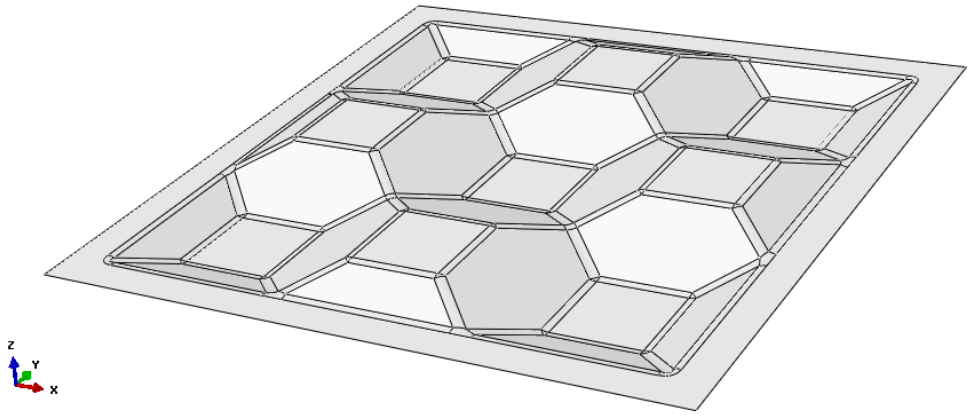

Figure 6.2. The core design.

The unique core design for this thesis study is depicted in Figure 6.2. The part is 340 mm in *x* and *y* directions and 20 mm from top to bottom. For the finite element simulations, there is no geometrical limitation for the shape of core. On the other hand, it may become impossible to manufacture the corresponding structure properly if the size of unit cell is too small.

For the face sheets, a two-dimensional deformable shell surface is created in 3D modeling space. The parts are 340 mm in *x* and *y* directions.

In order to apply load, a 3D circular bar is created as a rigid part. The diameter of the rigid bar is selected as 26 mm, same with the three-point bending fixtures of the test setup. While testing the sandwich structure, a rubber band is placed between the rigid bar and the face sheets for two reasons: firstly to distribute the line load and avoid stress concentrated areas, secondly to prevent slipping of the part over the bars. A 3 mm thick rubber band is also created as 3D deformable solid element.

6.2. Definition of Material and Stacking Sequences

The core and the sheets are E-glass-fiber reinforced epoxy laminates which are composed of eight. The mechanical properties of the material are listed in Tables 5.2 and 5.5. The extraction of these data is explained in Tensile Testing Section. The thickness of each ply is taken to be 0.18 mm for the core and 0.15 mm for the face sheets since the measured thickness of the core was 1.40 mm and that of the face sheets was 1.20 mm. The stacking sequence is defined as $[0/45/-45/90]_s$ for the core and the face sheets (Figure 6.3). Three integration points are assigned through the thickness of each ply.

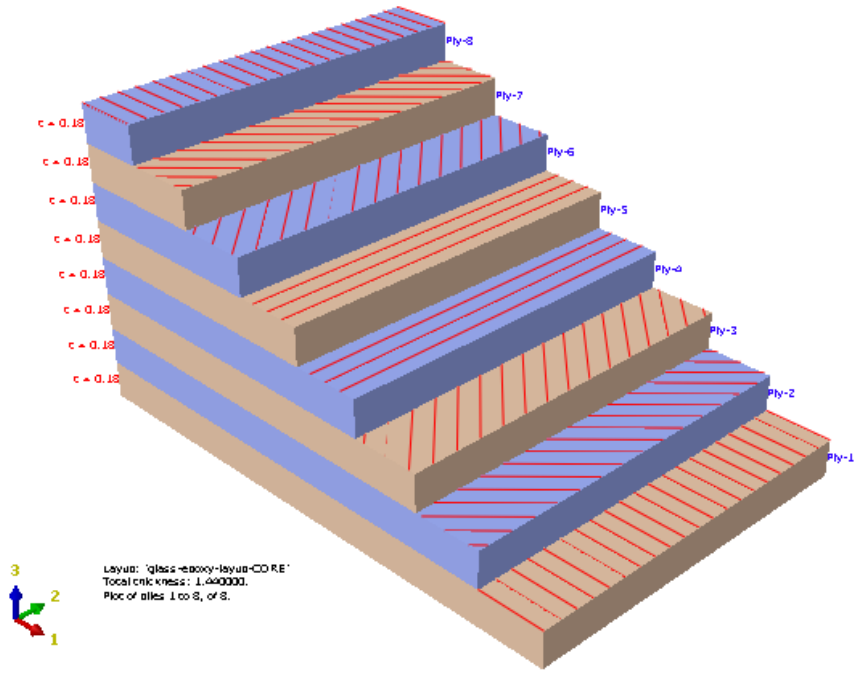

Figure 6.3. Ply orientation.

For a single ply, direction 1 corresponds to fiber direction and direction 2 corresponds to the in-plane direction transverse to the fibers. Because of the fact that global coordinate system is chosen as the reference coordinate system for the face sheets, direction 1 coincides with *x*-axis and direction 2 coincides with *y*-axis when the fiber orientation is given as 0^o. Figure 6.4 shows the orientation of fibers for 0^o ply.

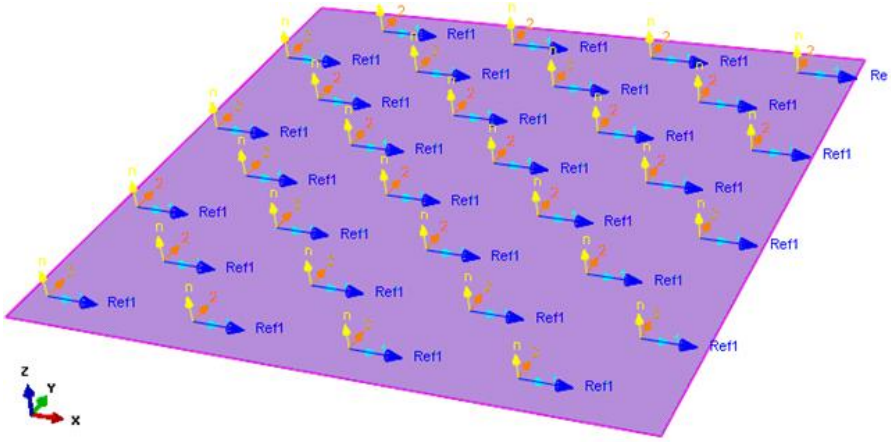

Figure 6.4. Fiber orientation for the face sheets.

Similarly, Figure 6.5 shows the orientation of fibers for 0^o ply at the core structure. For the top and bottom surfaces, which are on the *x-y* plane, direction 1 and direction 2 coincide with *x* and *y* axes, respectively. However, for other planes which are not on *x-y* plane, the orientation is decided by the direction of surface normals. Direction 3 is chosen to coincide with normal direction and as a result, the proper orientation is obtained.

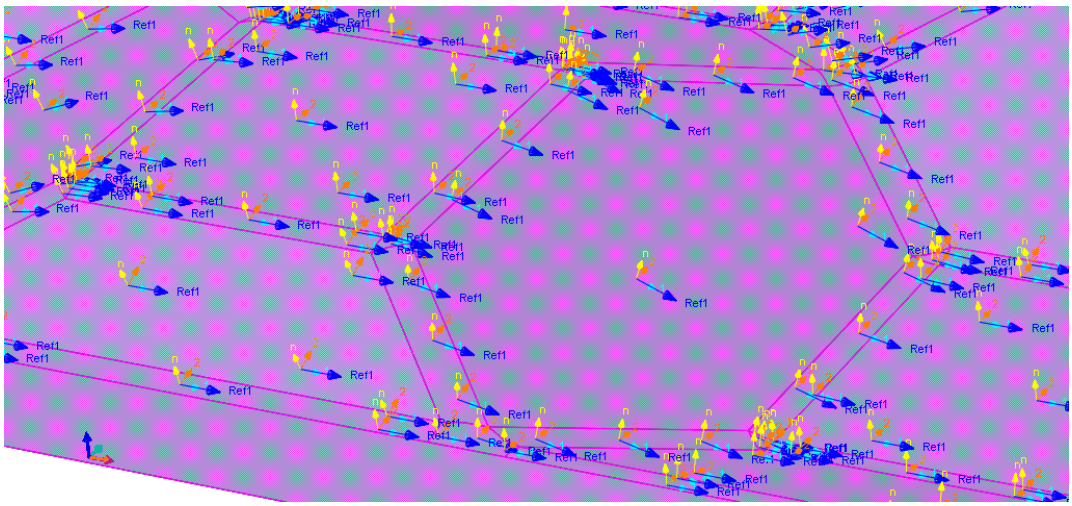

Figure 6.5. Fiber orientation for the core.

For the rubber band, the behavior of an isotropic material with 200 MPa as Young's Modulus and 0.3 as Poisson's Ratio is modeled and assigned to the rubber part. Although rubber is an incompressible hyper-elastic material undergoing large strains, it is modeled as a linear elastic material considering that the domain of interest is the composite part and therefore approximate representation of the band is sufficient.

6.3. Assembly

At the assembly section, each element is added to the assembly as dependent instances and translated to their exact locations. The distance between the centers of the two rigid bars under the structure is selected as 200 mm, the maximum span for the three point bending fixture.

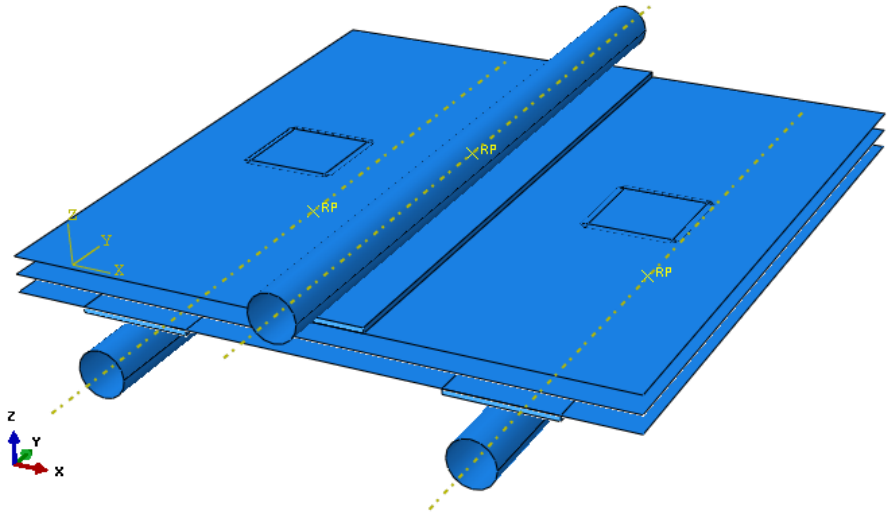

Figure 6.6. The assembly of the sandwich model.

6.4. Step

A general, a static step is defined for the deflection controlled three-point bending analysis. Due to the one dimensional interaction zone between the rigid bars and rubber bands, non-linearity effects have to be taken into consideration during the calculations. Therefore, NLGEOM is turned ON. Maximum number of increments is given as 1E6 and minimum increment size is given as 1E-30.

After running a job, the software creates a result file in which output data are stored. ABAQUS records stress, deflection and strain values as default parameters. However, if the user desires to record other parameters, such as Tsai-Hill failure index values, it has to be specified in this module. In this regard, four field output requests are created. The first

one is requested for the whole model's stress, strain, reaction force and displacement data. Other three requests are for storing failure index data for all section points of all the plies.

6.5. Interaction

In the test specimens, the core is attached to the top and bottom faces by an adhesive. In order to avoid difficulties of modeling a very thin layer, the adhesive is not included in the finite element model. Considering that, a quite strong epoxy based adhesive is used to bond core to the faces, no slip is expected during loading. Therefore, the interaction surfaces where adhesive is applied are simply tied to each other for simplicity.

While the structure deforms, initially not interacting surfaces may start to interact. Therefore, a contact property is defined for all other surfaces. In this model, no relative motion or indentation during interaction is expected. For this reason, contact properties are defined as frictionless for tangential behavior and "hard-contact" for normal behavior.

6.6. Boundary Conditions

In order to fix the rigid bars contacting the bottom of the sandwich structures, displacement boundary conditions at their reference points are defined as U1=0, U2=0, U3=0, UR1=0, UR2=0, and UR3=0. On the other hand, the motion of the rigid bar at the top should be allowed in the transverse direction. Rotational degrees of freedom and lateral translational degrees of freedom are fixed by setting U1, U2, UR1, UR2, and UR3 to zero while U3 is set to 6 mm as the initial displacement value (Figure 6.7).

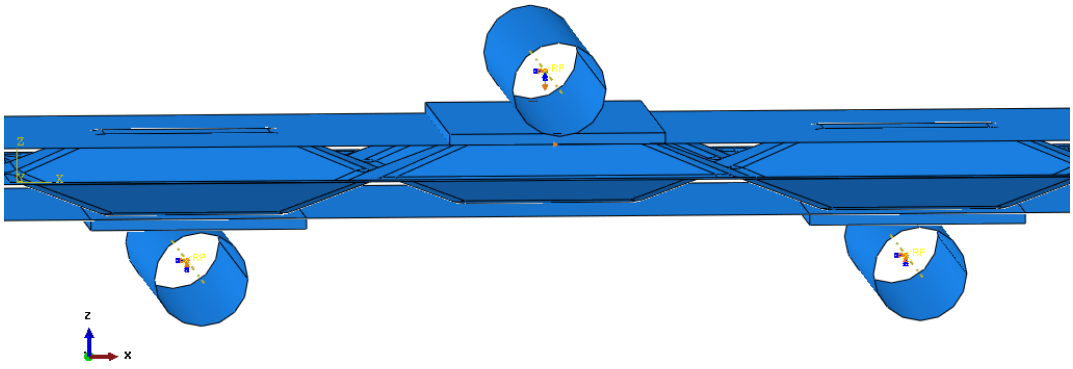

Figure 6.7. Boundary conditions.

One symmetry plane for the model is the *y*-*z* plane and it passes through the line where the upper bar and the rubber initially interacts. As a consequence, that plane should not move in *x* direction after deformation. Accordingly, the top face is partitioned along the line where the symmetry plane crosses and the lateral motion in the *x* direction is fixed. The second symmetry plane is on the *x*-*z* plane and it passes through the geometrical center of the top face. In order to limit lateral movement in the *y* direction, the node where two symmetry planes cross on top face is picked and fixed.

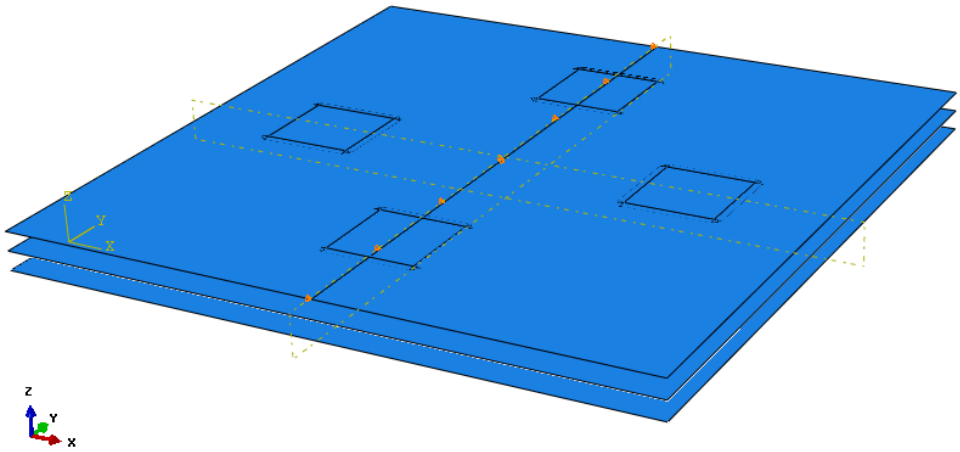

Figure 6.8. The symmetry planes.

6.7. Mesh

Shell elements approximate a three-dimensional continuum with a surface model. If the lateral dimension-to-thickness ratio is greater than 10, modeling it as a shell body decreases the computational time significantly without causing erroneous results. Accordingly, the core and face sheets are discretized by shell.

In ABAQUS, there are many different shell element types. They can be listed under three different categories: general-purpose shells, thick shells and thin shells. General-purpose shell element types are S4R and S3R. Thick shells are S8R and S8RT. Thin shells are STRI3, STRI35, S4R5, STRI65, STRI65, S8R5, and S9R5. For the loading conditions and the geometry in the present problem, general-purpose and thick shells are considered to be suitable. The analysis is not temperature dependent. Plus, triangular meshing is

unnecessary. Therefore, suitable element types are S4R and S8R for the model in this thesis study.

The element S4R has four nodes while S8R has 8 nodes. Both element types have reduced integration points. They have six degree of freedom, thee for displacement and three for global rotation. These elements obey first-order shear deformation theory. Therefore, they assume that transverse shear strains remain constant through the thickness.

In the elements, there are numerical calculation points that reflect the behavior of element. The way how algorithms integrate these points may influence the outcome of the analysis since the values of these points are used for the interpolation of other points. These points are called integration points and according to the element type, the number of them in one element can change.

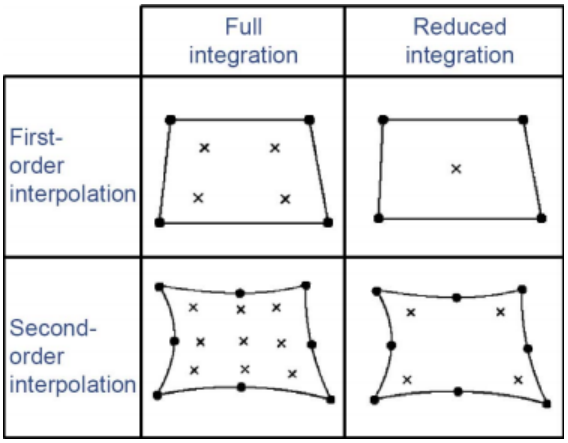

Figure 6.9. The integration points according to the integration type and the order of interpolation [90].

The algorithms carry out first order interpolation for elements with four nodes and second order interpolation for elements with eight nodes. The integration points for the full and reduced integration are shown in Figure 6.9 [90].

In the face sheets, S4R elements are generated. On the other hand, S8R element type is used in the core part since the core has more complex geometry. Convergence is better obtained with eight-node elements compared to elements with four nodes.

With the core structure, a mesh convergence study is conducted in order to decide the element size. While applying the same loading conditions, different element sizes are selected for the core. Based on the results presented in Figure 6.10, the element sizes for the core and sheets are selected as 4 mm and 5 mm, respectively.

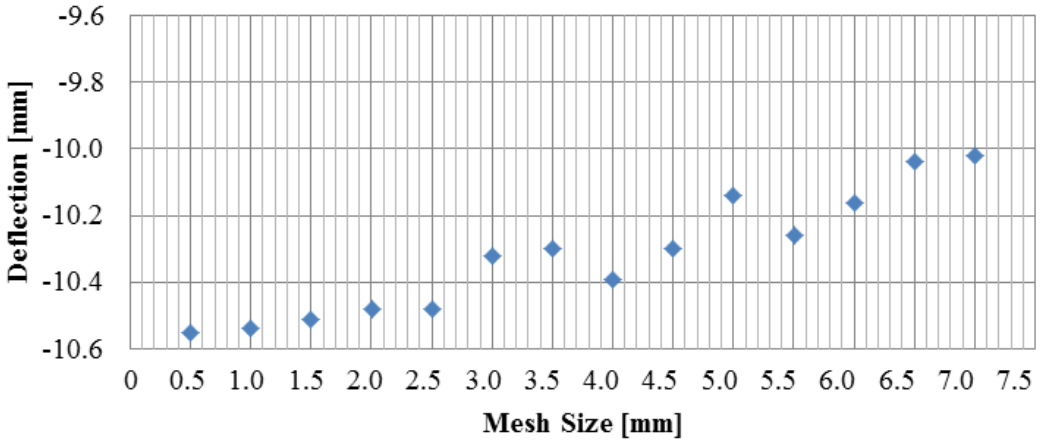

Figure 6.10. Mesh convergence study.

Figure 6.11 shows the meshed core structure, while Figure 6.12 shows the meshed assembly.

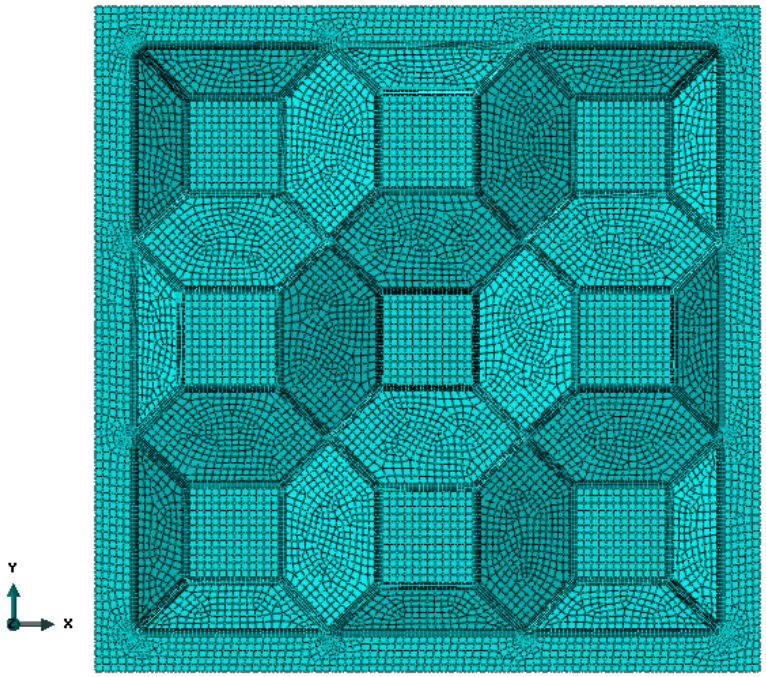

Figure 6.11. Meshed core structure.

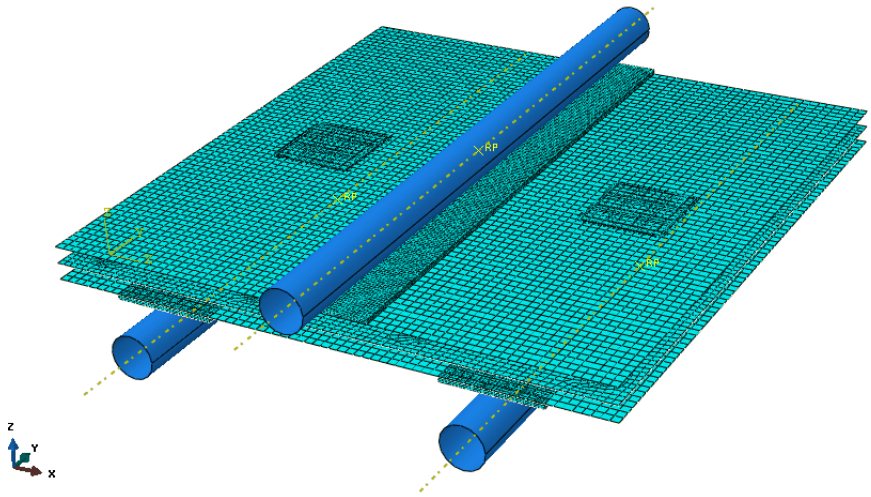

Figure 6.12. Meshed assembly.

Rubber bands are also meshed with an element size of 2 mm with C3D20R elements. They are brick elements with 20 nodes and reduced integration. Circular bars with rigid properties do not need to be meshed.

6.8. Job and Python Scripting

The finite element model of the sandwich structure is developed with the purpose of predicting initial failed regions and corresponding loading levels. In order to achieve this goal, an iterative study is performed by using secant algorithm.

$$x_n = x_{n-1} - f(x_{n-1})\frac{x_{n-1}-x_{n-2}}{f(x_{n-1})-f(x_{n-2})} = \frac{x_{n-2}f(x_{n-1})-x_{n-1}f(x_{n-2})}{f(x_{n-1})-f(x_{n-2})} \qquad (7.1)$$

The secant algorithm (Equation 7.1) is a root finding algorithm. It requires two inputs and corresponding outputs to perform an iterative study and find the root of a function. Because of the fact that displacement boundary conditions are defined, the assigned value for the deflection of the upper bar is the input value while the maximum failure of index in the structure is the output. When the index value is equal to or more than 1.0, the part is assumed to have failed. Therefore, the function is defined so that when the secant algorithm finds its root, it automatically finds the deflection value which makes the maximum value of failure index equal to 1.0.

In order to find the deflection value cause failure, a parametric Python Script code is written. The whole finite element model is created by this script code. According to the given initial deflection values, which are 6 mm and 4 mm, the code creates the first job file, runs the simulation and waits for completion to proceed for the second step. Once the first job is completed, it extracts the maximum failure index value in the structure from the corresponding result file and records the value as the output. Similarly, the second job is created and the second output value is obtained by following same steps. From this point, the secant algorithm starts to work and calculate the deflection value for the first iteration. It creates the corresponding job file and waits for completion to extract maximum index value. The user has to define a tolerance as stopping criterion for the secant algorithm as well. If the different between nth output and the previous one lies within the tolerance, the algorithm does not proceed to further iterations. In this study, the tolerance is given as 0.0001 for failure index.

Another important part of the code is that it does not take the values from stress concentrated areas into consideration while extracting the failure index values. Due to one dimensional loading (line loading due to circular-to-flat surface interaction), encircled regions are neglected during failure index data extraction.

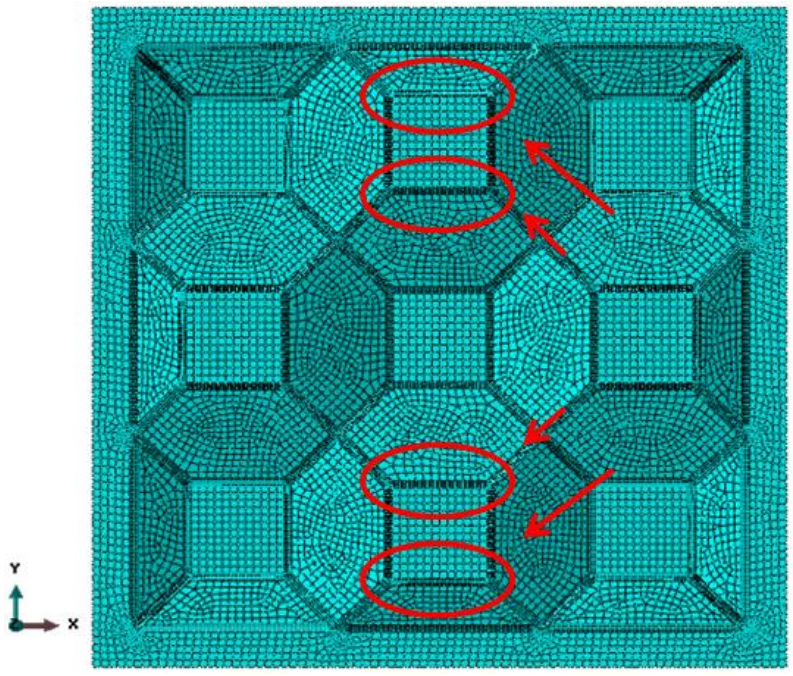

Figure 6.13. Stress concentrated regions.

The element types, the number of element and nodes for each segment of the model are tabulated in Table 6.1. Since the size of the structure is large, the required time for a single simulation is long. To decrease the computational time, results are obtained in a computer with 10 processors. The written Python Script to create such model has 820 lines and 43456 characters in total.

Table 6.1. Element properties of each part in the model.

	Element Type	Number of Element	Number of Nodes
Face Sheets	S4R	4624 each	18496 each
Core	S8R	15327	122616
Rubber Bands	C3D20R	15300 each	306000 each
The Model	-	70475 total	1077608 total

7. RESULTS AND DISCUSSION

In order to observe the failure behavior of the new sandwich design and verify the finite element model, three sandwich plates are manufactured and tested using a three-point bending test setup. The stacking sequence and the dimensions of these specimens are listed in Table 7.1:

Table 7.1. The stacking sequence and the dimensions of the specimens.

	Part of the Structure:	Property:
Stacking Sequence	The core and the face sheets	$[0/45/-45/90]_s$
Thickness	The face sheets	0.15 mm / ply
	The core	0.18 mm / ply

7.1. Test Setup

Three-point bending tests are performed on MTS servo hydraulic test machine with a three-point bending fixture. The three circular bars used in the fixture have a length of 300 mm, which is the same as the lateral length of the specimens, and a diameter of 26 mm.

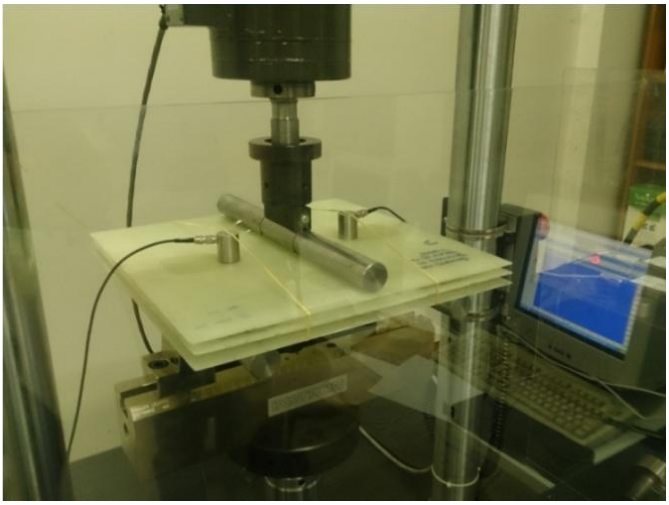

Figure 7.1. The experimental setup.

For specimen 1, both of the piezoelectric transducers are placed on the top and no rubber bands are placed between the bars and the specimen. The test is deflection

controlled with the rate of 3.55 mm/min. The same settings are used for the acoustic emission equipment as in the test of the cross-ply specimens. Figure 7.1 shows the experiment setup.

The tests are planned such that the load is increased until the structure breaks apart. Accordingly, the maximum stroke is used in this three-point bending test, which is 75 mm. However, the plate remained in one piece even after 75 mm deflection. As seen in Figure 7.3, the plate keeps its integrity although the deflection at the end of the experiment approaches almost four times its total thickness. At the peak load, the measured reaction force reaches 4820 N. The corresponding deflection is measured as 5.70 mm. The whole experiment takes more than 20 minutes with the chosen loading rate. On the other hand, only the first region up to the ultimate load is needed for model verification. In order to predict the whole failure behavior, a progressive model has to be developed, which is not within the scope of this study.

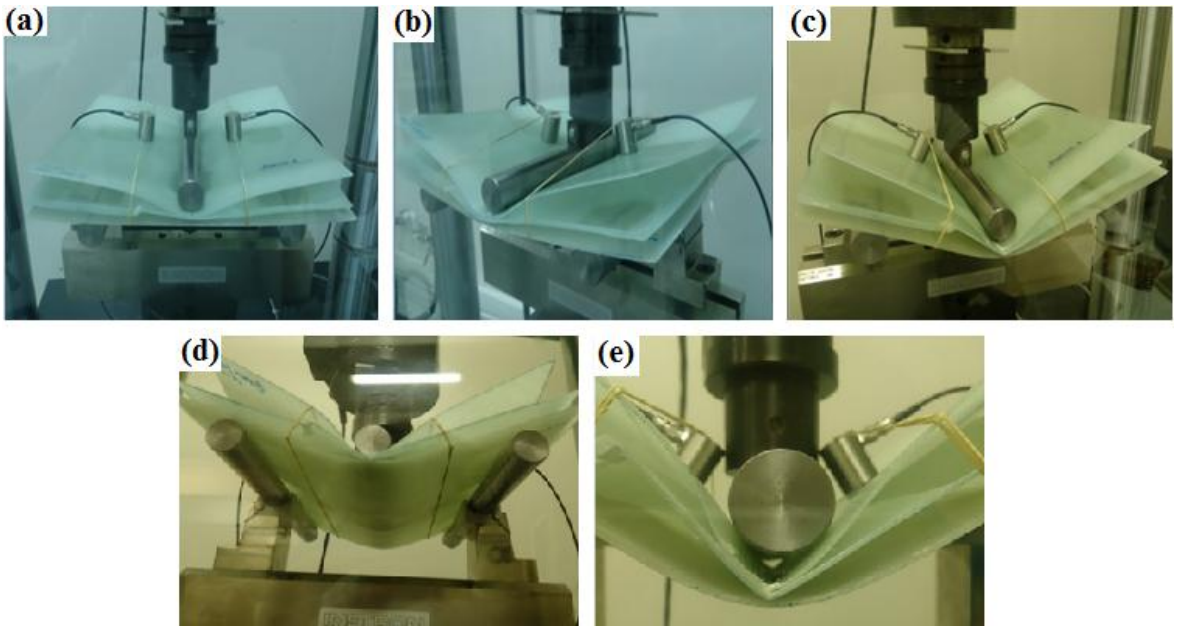

Figure 7.2. The first experiment at when the deflection of the middle bar is (a)17 mm, (b) 28 mm, (c) 52 mm (d) 52 mm, and (e) 66 mm.

7.2. Three-Point Bending Tests of the Sandwich Plates

Figure 7.3 shows the change in load over time. From the beginning to 3 kN, the load increases linearly. From 3 kN up to the ultimate load, which is 4.8 kN, the slope gradually decreases. The change of slope between 3 kN - 4.8 kN may be explained by the effects of activated failure mechanisms and partially by viscoelastic effects. In that case, some AE data should be detected at the corresponding times. However, the transducers were able to detect a signal only after reaching the ultimate load level (Figure 7.4). This may be the result of inappropriate positioning of the transducers.

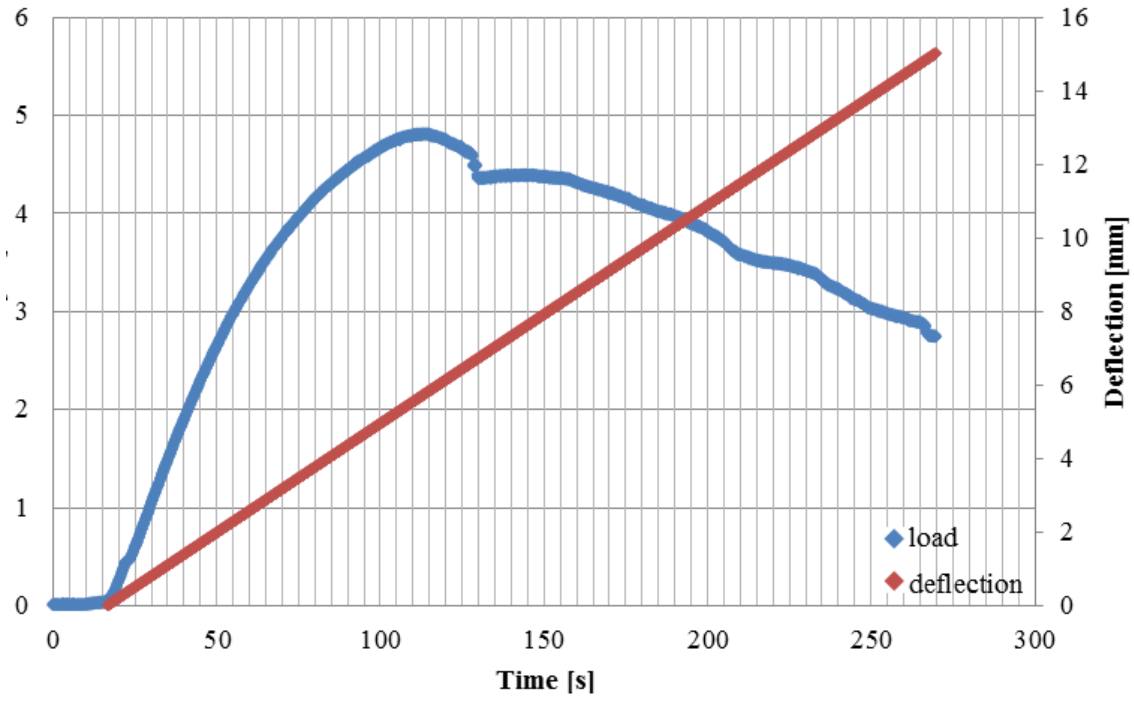

Figure 7.3. Load and deflection vs. time for the first specimen.

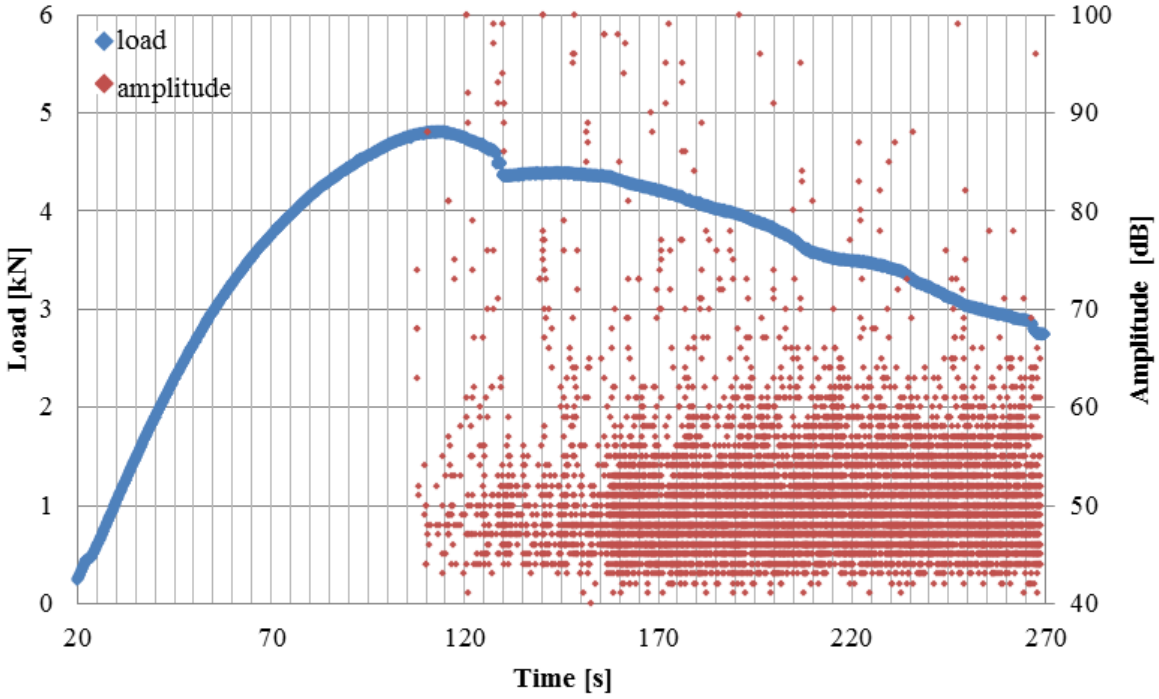

Figure 7.4. Load and amplitude distribution vs. time for the first specimen.

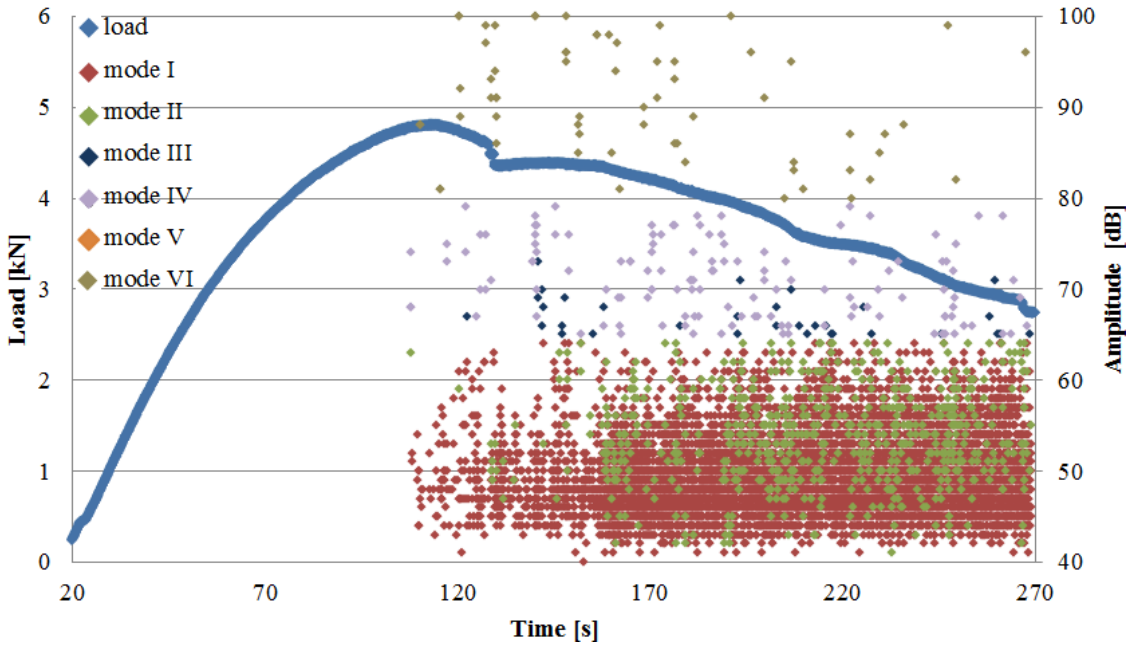

Figure 7.5. The classification of the amplitude data according to Aramugam *et al.* [83].

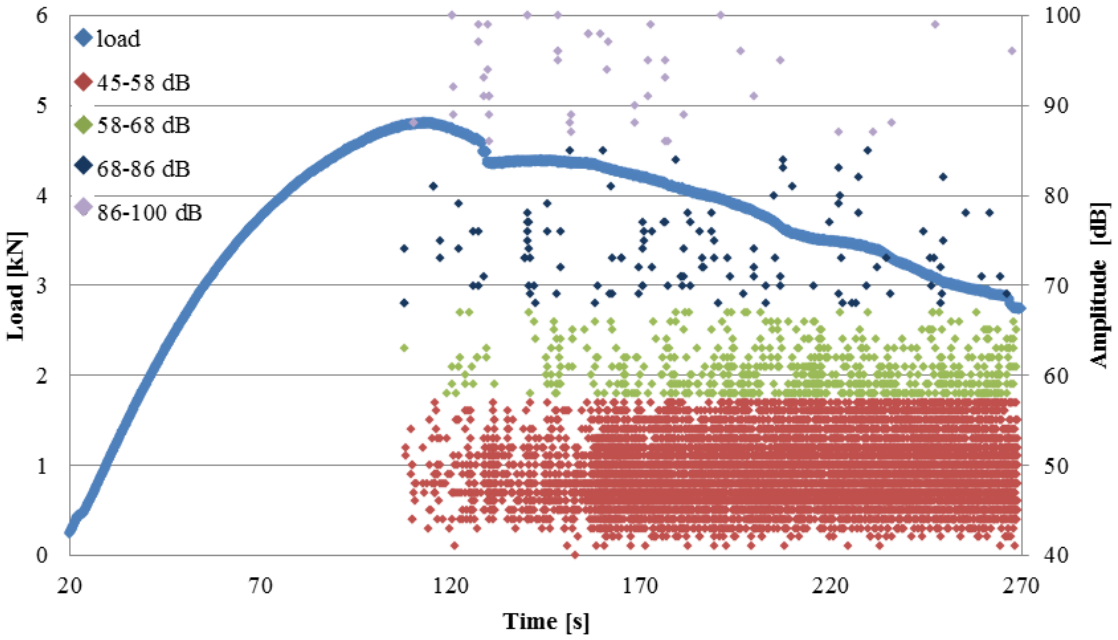

Figure 7.6. The classification of the amplitude data according to Laksimi *et al.* [79].

Similar to the tensile test specimens, it may not be easy to identify the activated failure mechanisms by parameter based approaches (Figures 7.5 and 7.6). Therefore, the AE data for the three-point bending tests should be investigated in the frequency spectrum. Figure 7.7 reveals the dominant frequency distribution for the first specimen. The peak frequencies lie in the same frequency bands as the tension tests. According to the AE data distribution, it is possible to say that matrix cracking and fiber-matrix debonding are the initially activated failure mechanisms for the sandwich plate. Based on the load-displacement relation, one may infer that matrix micro cracking starts when the load reaches 3 kN. From 3 kN to 4.8 kN, initial micro cracks coalesce to initiate matrix cracking and local debonding. Although the structure is being damaged, the AE monitoring system fails to detect any wave at this stage. When the peak level is left behind, although the load bearing capability of the plate decreases, it can still withstand loads above 4 kN until to the point where deflection reaches 8 mm. After 170th second of the experiment, the transducers start detecting excessive amount of fiber failure originated signals.

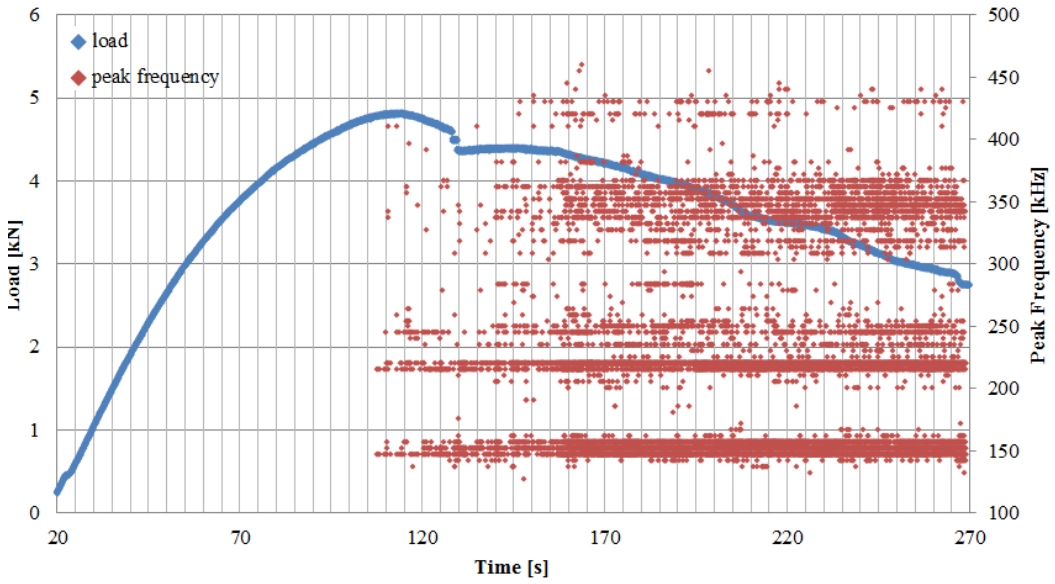

Figure 7.7. Peak frequency vs. time for the first specimen.

In order to verify the finite element model, the loading conditions corresponding to the peak level are considered. The model with no rubber bands is subjected to deflection controlled loading by setting the displacement of the middle bar, U3 to 5.70 mm. Figure 7.8 depicts the displacement of the structure under vertical loading.

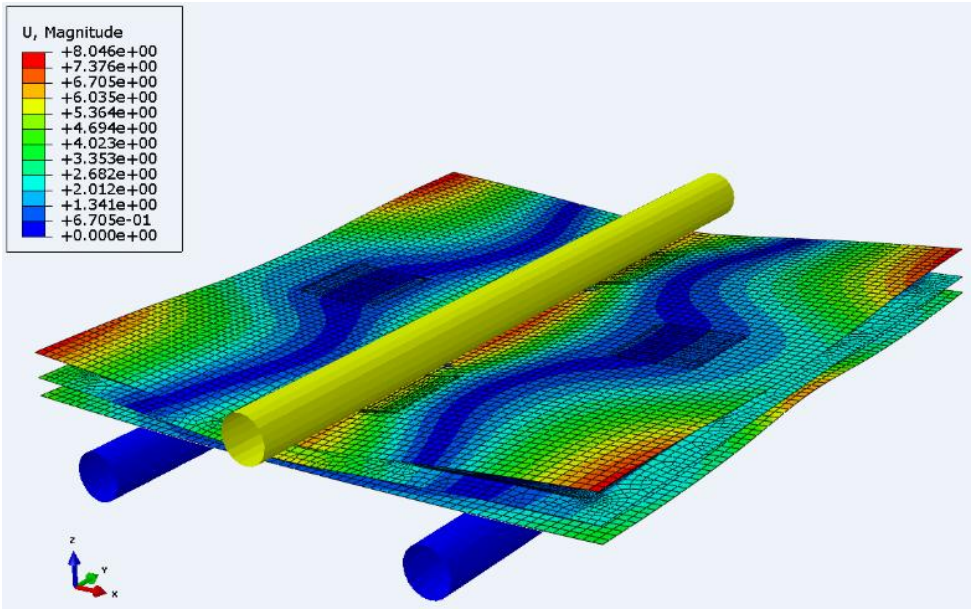

Figure 7.8. Deflection state of the model under U3=5.70 mm loading.

Since the structure consists of laminae with different orientations, the stress distribution in each lamina is different. Figure 7.9 shows the maximum in-plane principal stress distribution of the top layer of the core structure. As it is seen clearly, the line contact with the rigid bar and the rigidly attached regions of the core to the top sheet create high stress concentration. Actually, stress concentrations are not so severe. Corresponding failure index distribution of the core structure is shown in Figures 7.10 and 7.11. The regions of high stress concentration have very high failure index values; especially the borderlines of the glued surfaces. In order to predict the deflection and the load level causing failure, these stress concentrated areas have to be neglected. For this particular core design, there are two cells on the *y-z* symmetry plane which are attached to the top face sheet and there are two borderlines in x direction for each cell, and therefore there are four stress concentrated regions in the core. At one side of these borderlines, the glued surfaces on *x-y* plane lie. At the other side of these borderlines, the curved regions exist. In order to neglect the effects of severely stress concentrated areas, Tsai-Hill failure index values at all the elements on these four curved regions and the first rows of the elements at the two sides of these curved regions are not taken into account. Similarly, the elements of the top face sheet which lie within the vertical projection of the neglected areas of the core are also not taken into account.

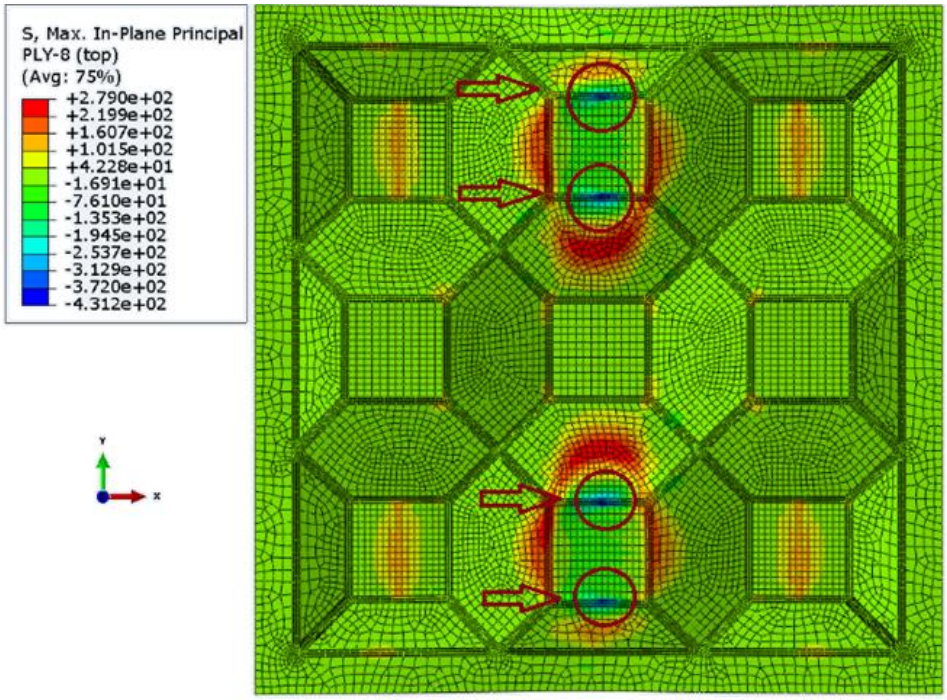

Figure 7.9. Stress concentrated regions in the core.

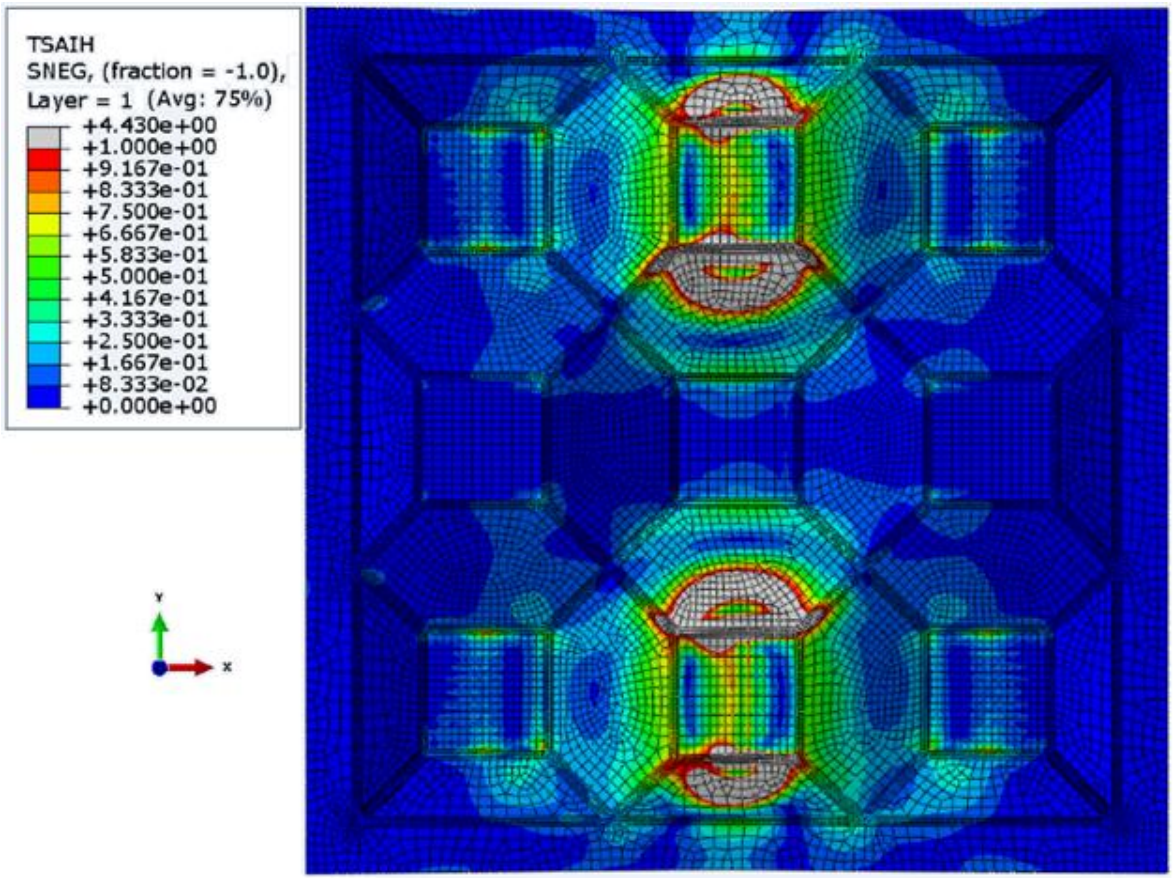

Figure 7.10. The distribution of Tsai-Hill failure index.

For the case of plate 1, the software measures the reaction force on the rigid bar as 5090 N. When it is compared with the actual test result, which is 4800 N, it can be said that the model estimates the macro mechanical behavior of the structure well. The main reason for the error is that the specimen undergoes some damage before the peak load; this changes its stiffness properties, which is not considered in the FE model. Besides, there is some scatter in the material properties. The tensile test specimens do not have exactly a uniform geometry; the thickness may not be perfectly uniform. In addition to that, there are viscoelastic effects, which are neglected. Considering these possible sources of errors, the model can be accepted as successful for preliminary failure analysis, but should be improved in the further simulations.

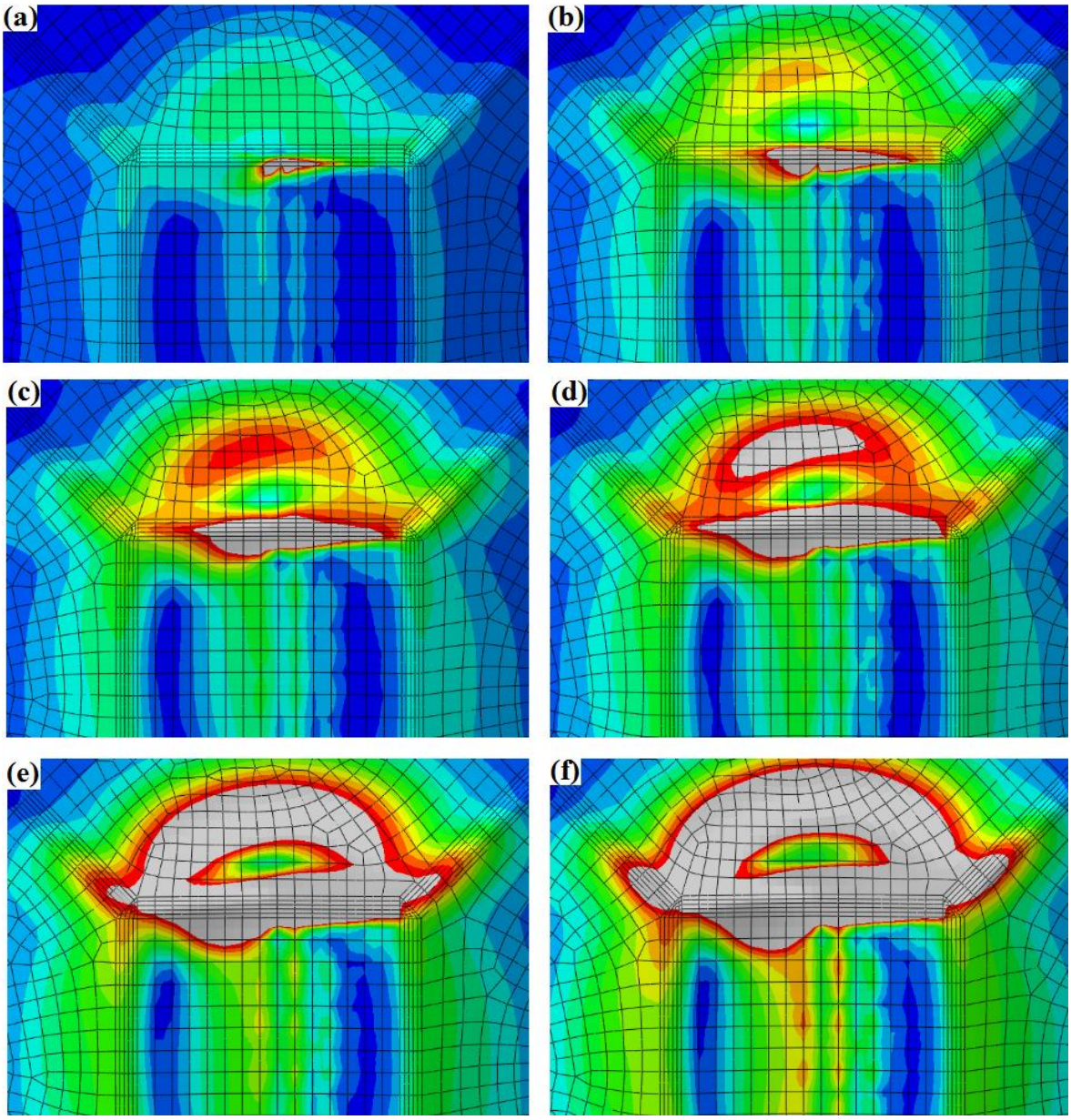

Figure 7.11. The failure index distribution when the deflection of the middle bar is (a) 1.14 mm, (b) 2.28 mm, (c) 2.85 mm, (d) 3.42 mm, (e) 4.56 mm, and (f) 5.70 mm.

The first specimen is cut into two pieces for inspection (Figure 7.12a). Comparing the distribution of the failure index predicted by the FE model and shown in Figure 7.11 and the failed regions in the specimen shown in Figure 7.12b, one may infer that the agreement between the prediction and the test results is quite satisfying.

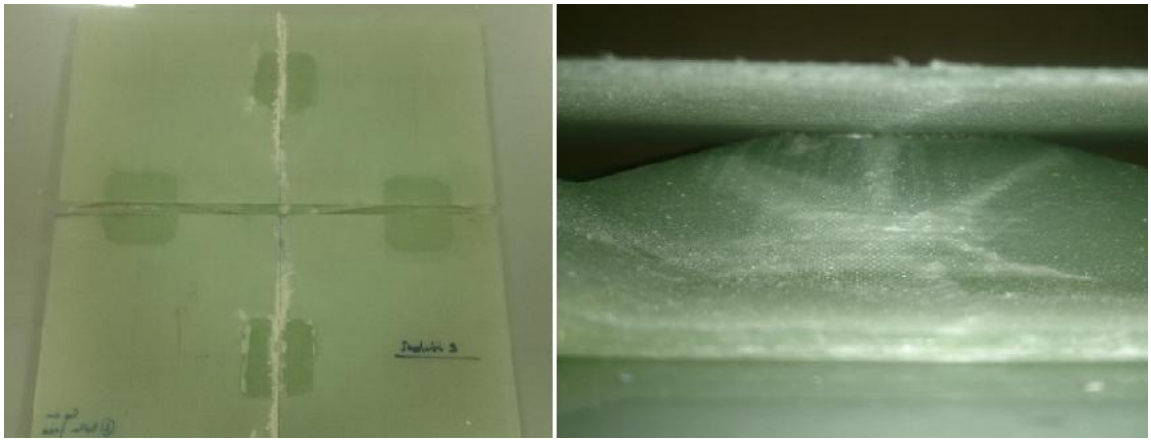

Figure 7.12. (a) Plate one in two pieces and (b) actual region.

In the subsequent two tests, in order to decrease the size of the stress concentration regions, and also provide distributed load, rubber bands are used. 3-mm thick rubber bands are placed between the bars and the plate surfaces as shown in Figure 7.13. Besides, one of the piezoelectric transducers is placed on the top face and the other one is placed on the bottom face. Both tests are deflection controlled with the rate of 1.75 mm/min. Settings of the acoustic emission equipment are chosen to be same as in the tension tests of the quasi-isotropic specimens.

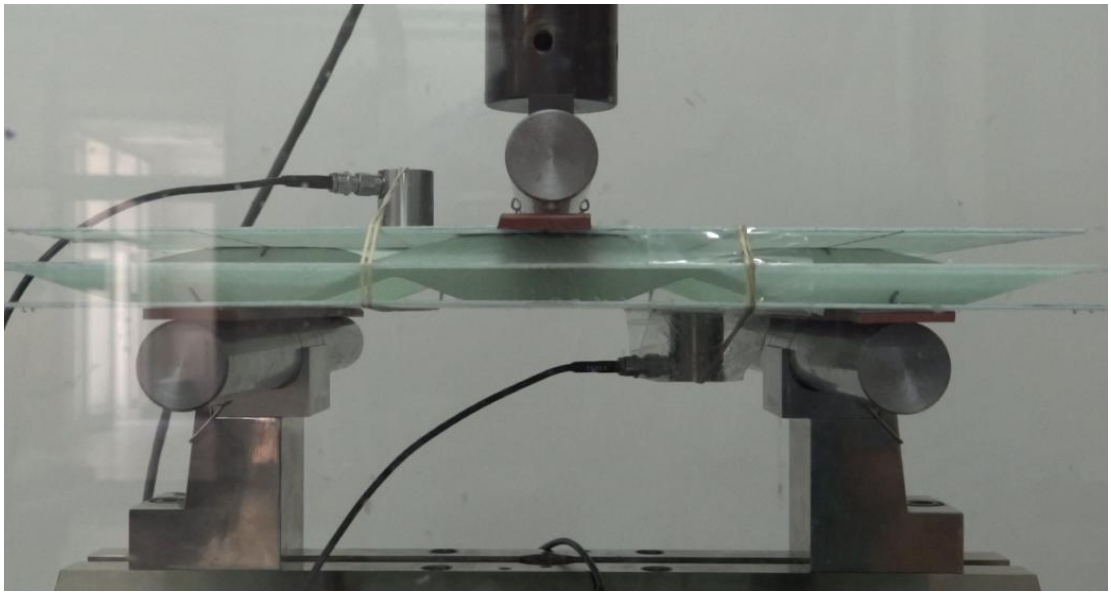

Figure 7.13. The experimental setup for the second and the third specimens.

For the second specimen, the load and deflection data are plotted in Figure 7.14, the acoustic emission data are shown in Figure 7.15, and corresponding peak frequency distributions of the detected waves are shown in Figure 7.16. The graphs shown in Figures 7.17, 7.18, and 7.19 are for the third specimen.

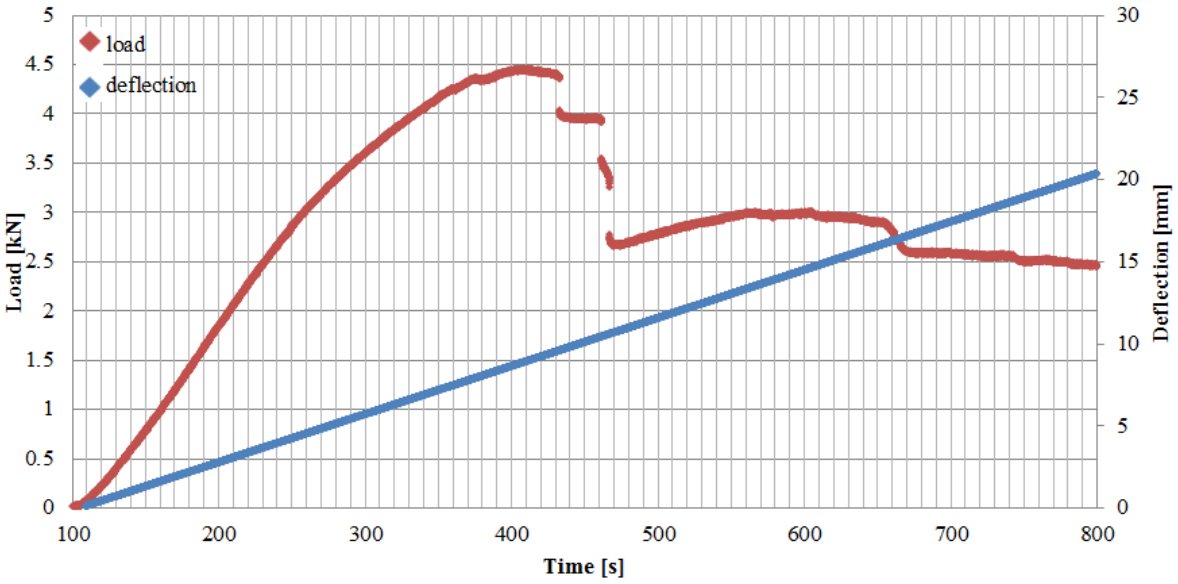

Figure 7.14. Load and deflection vs. time for the second specimen.

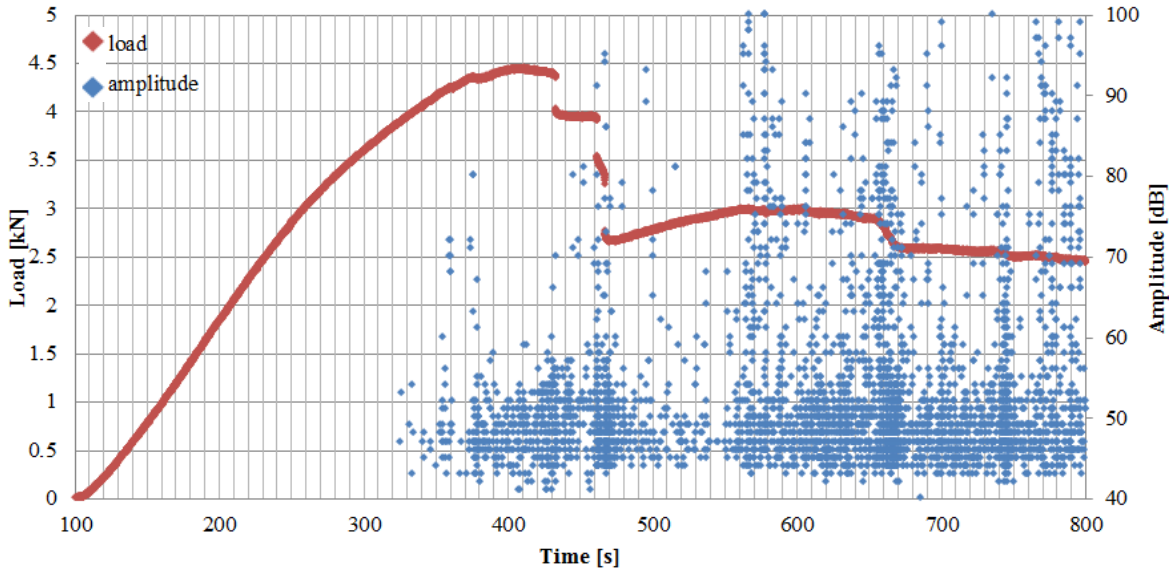

Figure 7.15. Amplitude vs. time for the second specimen.

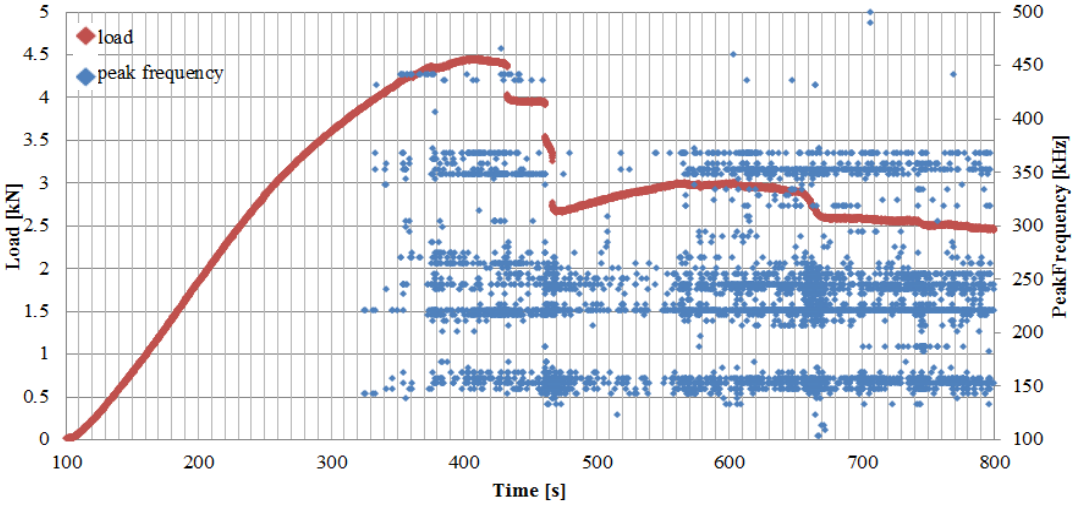

Figure 7.16. Peak frequency vs. time for the second specimen.

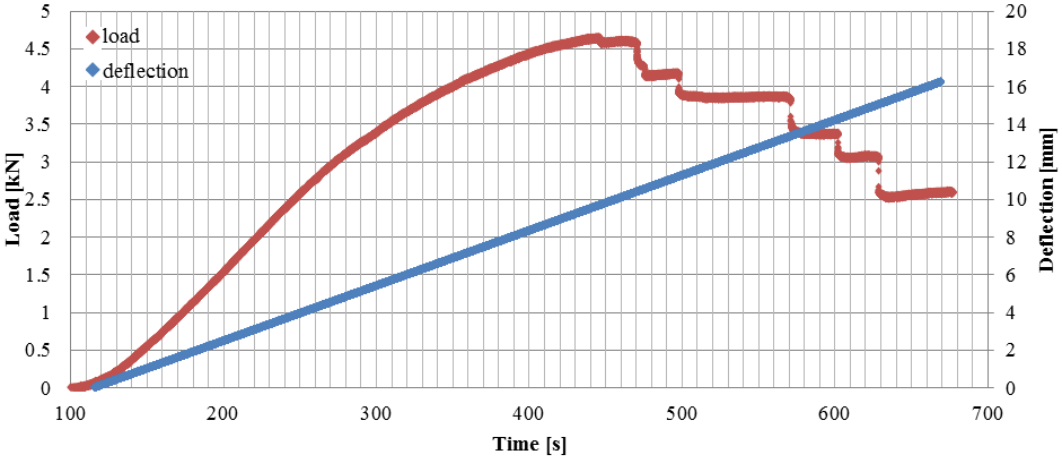

Figure 7.17. Load and deflection vs. time for the third specimen.

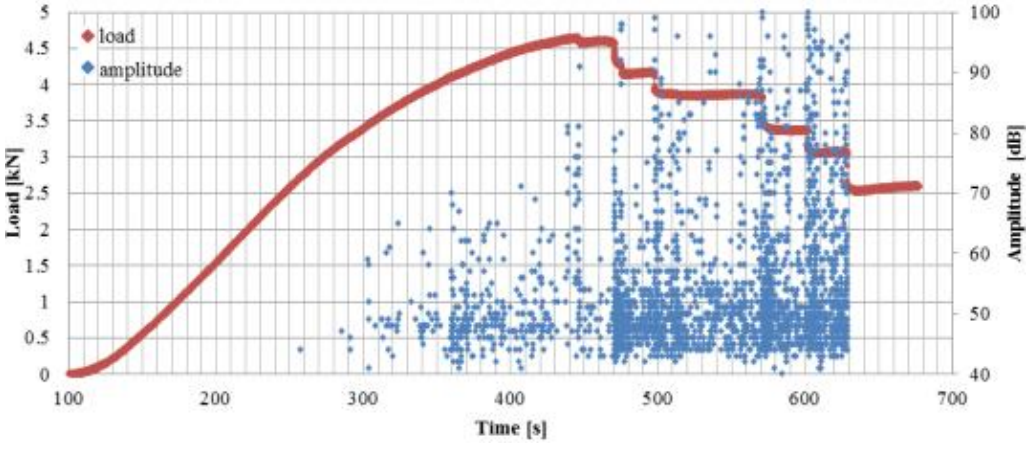

Figure 7.18. Amplitude vs. time for the third plate.

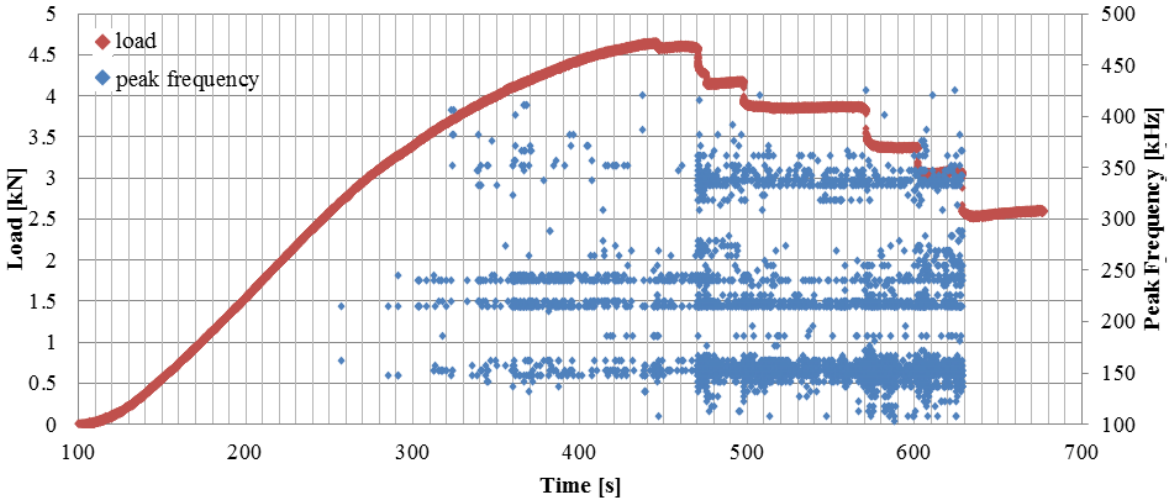

Figure 7.19. Peak frequency vs. time for the third plate.

As seen in Figure 7.14, the maximum loading of the second specimen occurs when the deflection reaches 8 mm. The peak load level reaches almost 4440 N. For the third plate, the peak load level is a little higher, around 4650 N, and the corresponding deflection is 9.5 mm. Note that for the first plate, the maximum load is reached when the deflection is 5.7 mm. The reason for the difference is the presence of the rubber bands.

Figures 7.15, 7.16, 7.18, and 7.19 reveal that placing one of the transducers on the bottom surface helps the AE system to detect earlier damages. As opposed to the first plate, the AE system manages to detect waves before the peak load level is reached. The tensile strength of the material of the specimen is higher than its compressive strength in the longitudinal direction. On the other hand, the compressive strength is higher than the tensile strength in the transverse direction. When plates 2 and 3 are subjected to the bending load, the upper regions have to withstand compressive stresses while the lower regions have to withstand tensile loads. Therefore, initial matrix cracking should be seen first at the bottom regions. The proper positioning of the transducers helps detect the initial signals. At the initial stages of the experiments, matrix related failure mechanisms are expected to occur. Similar to the previous experiments, the peak frequency values lie in the same frequency bands. An important detail is that the density of the detected waves in 350 kHz band after 560th second of the experiment for plate 2 (Figure 7.16) and 460th second of the experiment for plate 3 (Figure 7.19) are much lower than that of the previous tests. One may say that this is due to the use of rubber bands since concentrated line loads are

prevented on the face parts. In order to verify the finite element model, the loading conditions corresponding to the peak level are considered. The structural model with rubber bands is subjected to deflection controlled loading by setting the displacement of the middle bar, U3 to 8 mm. Figure 7.20 depicts the displacement of the structure under vertical loading. The maximum in-plane principal stress state of the top layer of the core is shown in Figure 7.21, with the stress concentration regions.

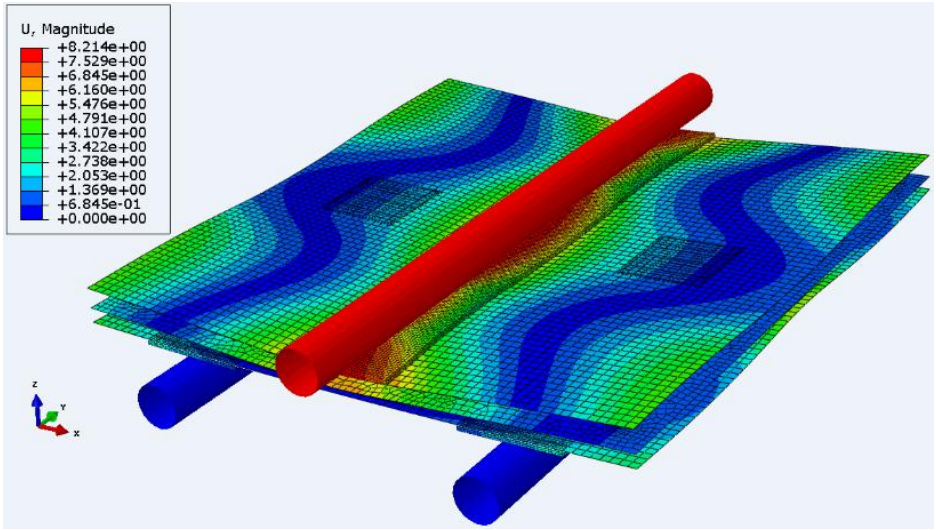

Figure 7.20. Deflection state of the model under U3=8 mm loading.

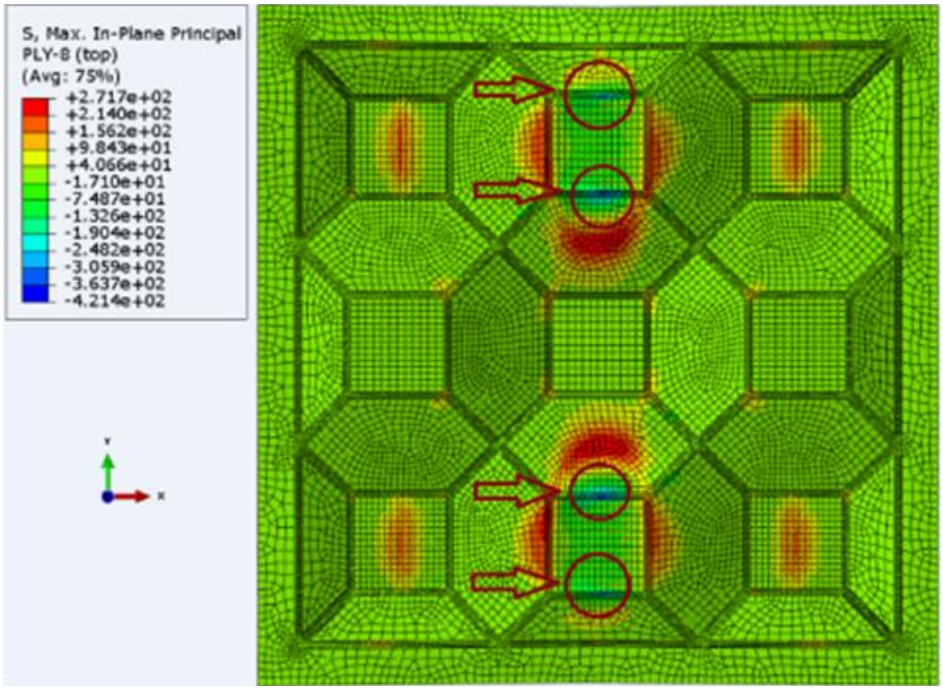

Figure 7.21. Stress concentrated regions in the core.

While the model is subjected to the maximum level of loading, the rubber band on the top deforms and transmits the load in a more distributed manner. Figure 7.22 shows the Tsai-Hill failure index distribution of the core and Figure 7.23 shows the change in the failure index field for the top layer of the core during the loading. The observed region in Figure 7.23 is the lower unit cell in Figure 7.22. The stress concentration region is located on the line in contact with the upper bar. Besides, the border lines of the rigidly attached regions of the core to the top sheet have very high stress concentration. In reality, the connection is not rigid and the edges of the glued region are not sharp.

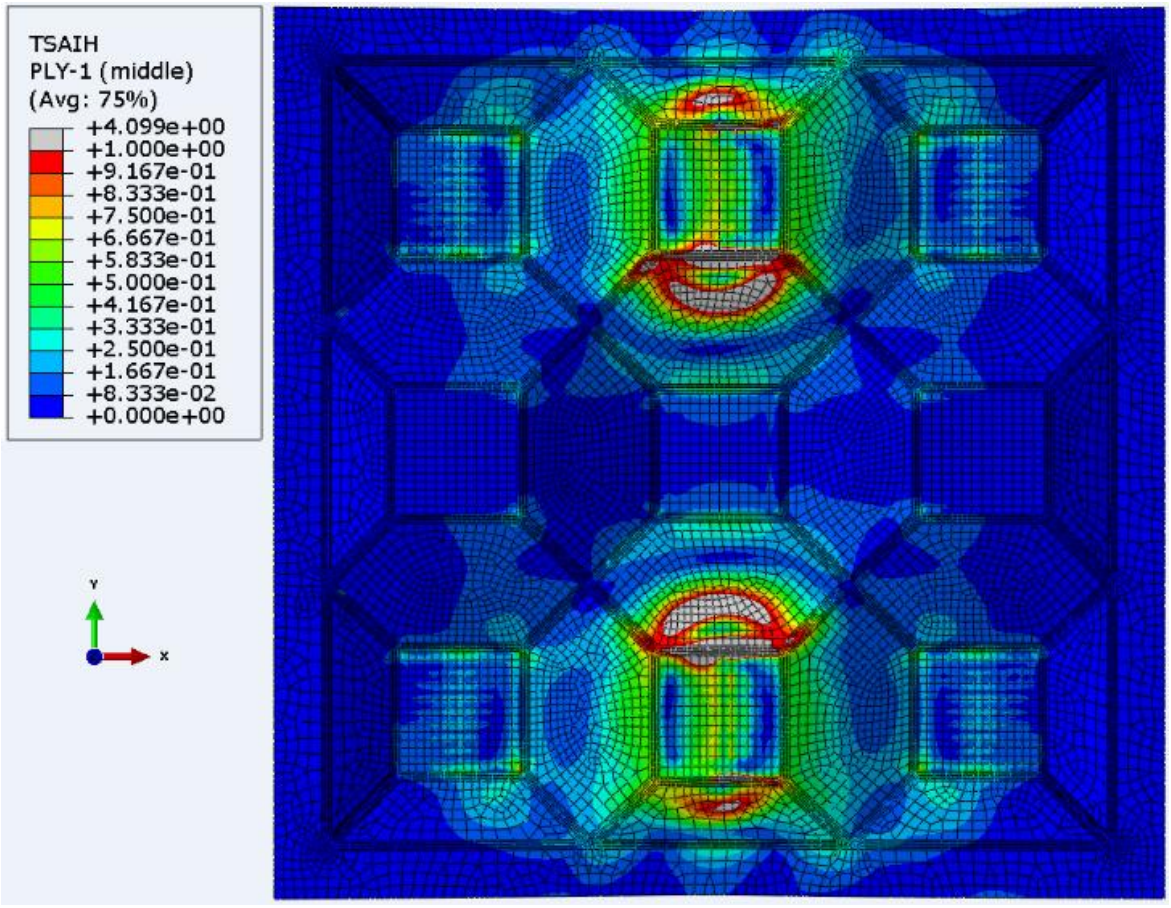

Figure 7.22. The failure index distribution of the core.

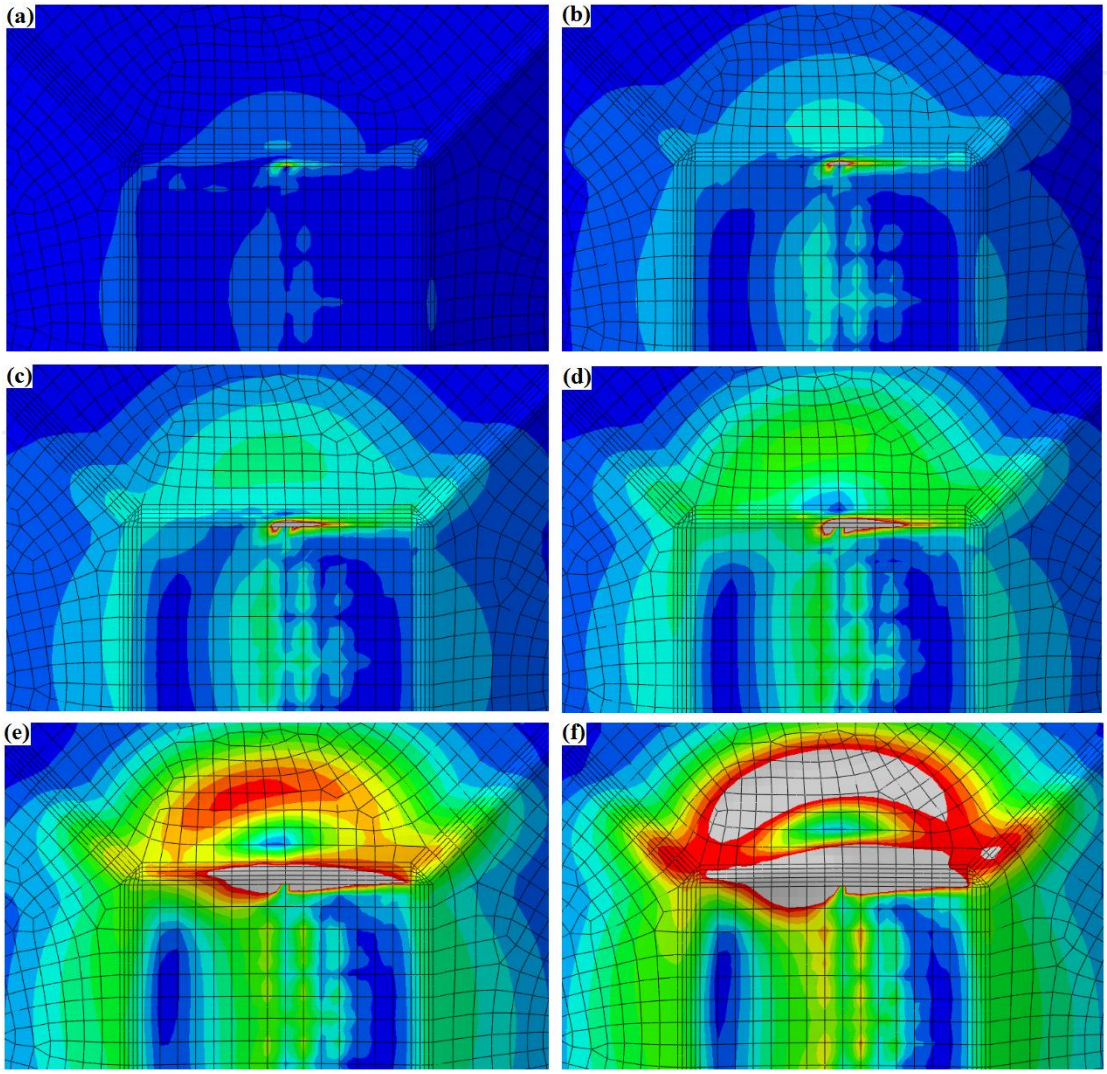

Figure 7.23. The failure index distribution for the top layer of the core at when the deflection of the middle bar is (a) 1.6 mm, (b) 3.2 mm, (c) 4 mm, (d) 4.8 mm, (e) 6.4 mm, and (d) 8 mm.

For the color scaling of Figures 7.22 and 7.23, 1.0 is selected as the upper limit. In the grey regions, the failure index is above 1.0, therefore they are assumed to have failed. An iterative study is conducted to find the deflection and the load for which the maximum failure index is equal to one. This is the case shown in Figure 7.23b, if the excessive stress concentration is not taken into account. Then, the FE model highly underestimates the failure load. As in the core part (Figure 7.21), the same problem occurs on the top part (Figure 7.24), too.

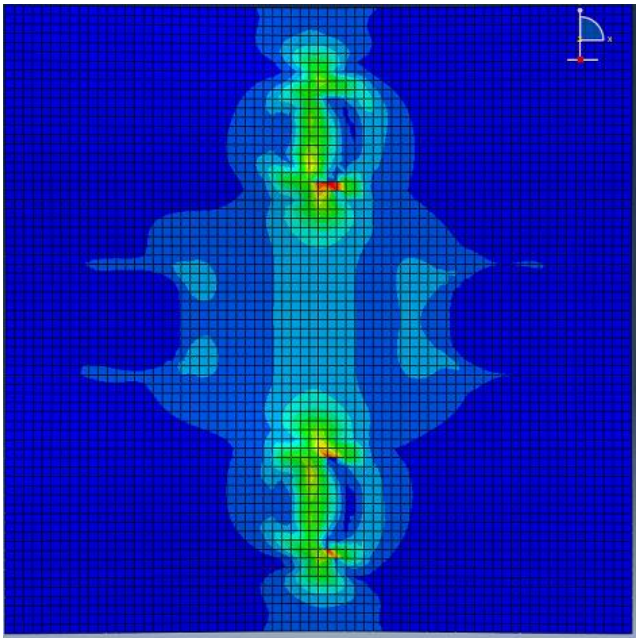

Figure 7.24. The maximum in-plane stress distribution of the face sheet, showing the stress concentration region for 8 mm deflection.

In the Python Script code, the severely stress concentrated regions should be neglected for the secant algorithm. As stated previously, there are two cells of the core on the *y*-*z* symmetry plane which are directly attached to the top face sheet and there are two borderlines parallel to the *x*-direction for each cell, and therefore there are four stress concentrated regions in the core. At one side of these borderlines, the glued surfaces on *x*-*y* plane lie. At the other side of these borderlines, the curved fillet regions exist which lie between the angulated core walls and the glued horizontal sections. In order to neglect the effects of severely stress concentrated areas, Tsai-Hill failure index values at all the elements on these four curved regions and the first rows of the elements at the two sides of these curved regions are not taken into account. Similarly, the elements of the top face sheet which lie within the vertical projection of the neglected areas of the core are also not taken into account. The failure index predictions of the FE model are assumed to be much higher than the actual values in these regions. Although, some damage may occur in these regions at low levels of load, the damage is assumed to have very small effect on the macro behavior of the specimen. As seen in Figure 7.23a, the FE model predicts failure on stress concentration regions when the deflection of the middle bar is equal to 1.6 mm. The corresponding reaction force on the middle bar is calculated as 1178 N. Note that the mechanical response of the second and the third specimens did not change at 1.2 kN load

level and the piezoelectric transducers did not detect any AE signals at the same load level (Figures 7.16 and 7.19). Therefore, neglecting those stress concentration regions for the secant algorithm is not an incorrect decision. The output of the secant algorithm is tabulated in Table 7.1. The table also gives the location of the most critical element and the section of the element where the initial failure is predicted. Along the thickness of a single ply, three integration points are defined. Therefore, there are 24 sections in a single element for the model. Each section has four integration points since S8R is the selected element type. After seven iterations, the algorithm finds that the initial failure occurs when the deflection of the middle bar reaches 5.91 mm. For the corresponding loading condition, the distribution of the failure index on the first layer of the core part (section 24) is shown in Figure 7.25. The algorithm predicts the failure on the element 14005 of the core. The 24^{th} section corresponds to the top layer of the core. For the top layer of the core, the longitudinal direction is perpendicular to the axis of the middle bar. Table 7.2 shows the longitudinal, transverse, shear and the maximum in-plane principal stress values at the integration points of the 24^{th} section (top layer) of the element 14005 of the core. As seen in Table 7.2 clearly, while the longitudinal stress is much lower than the longitudinal tensile failure strength of the lamina, the transverse stress is about to reach the transverse tensile failure strength, which is found as 75 MPa in the Section 5.3. Tsai-Hill failure criterion is an interactive failure criterion, which is incapable of describing the mode of the failure. On the other hand, it is possible to say that the corresponding sub-criterion of the maximum stress criterion (Equation 2.2) is almost satisfied, which indicates that the failure occurs due to the transverse tensile load.

Table 7.2. Output of the secant algorithm.

Iteration no:	Deflection [mm]	Maximum failure index	Location	Element number	Section
1	6	1.0429	Core	14005	24
2	4	0.6391	Core	5201	24
3	5.7876	0.9463	Core	14005	24
4	6.1001	1.0877	Core	14005	24
5	5.9063	1.0005	Core	14005	24
6	5.9051	1.0001	Core	14005	24
7	5.9052	1	Core	14005	24

Table 7.3. The longitudinal, transverse, shear and the maximum in-plane principal stress values at the integration points of the 24th section (top layer) of the element 14005 of the core.

Integration point #:	#1	#2	#3	#4
Longitudinal stress [MPa]:	151.6	151.3	115.2	116.0
Transverse stress [MPa]:	73.9	73.9	72.7	73.1
Shear stress [MPa]:	-1.8	-1.7	-1.6	-2.1
Max in-plane principal stress [MPa]:	152.2	151.3	115.0	115.1

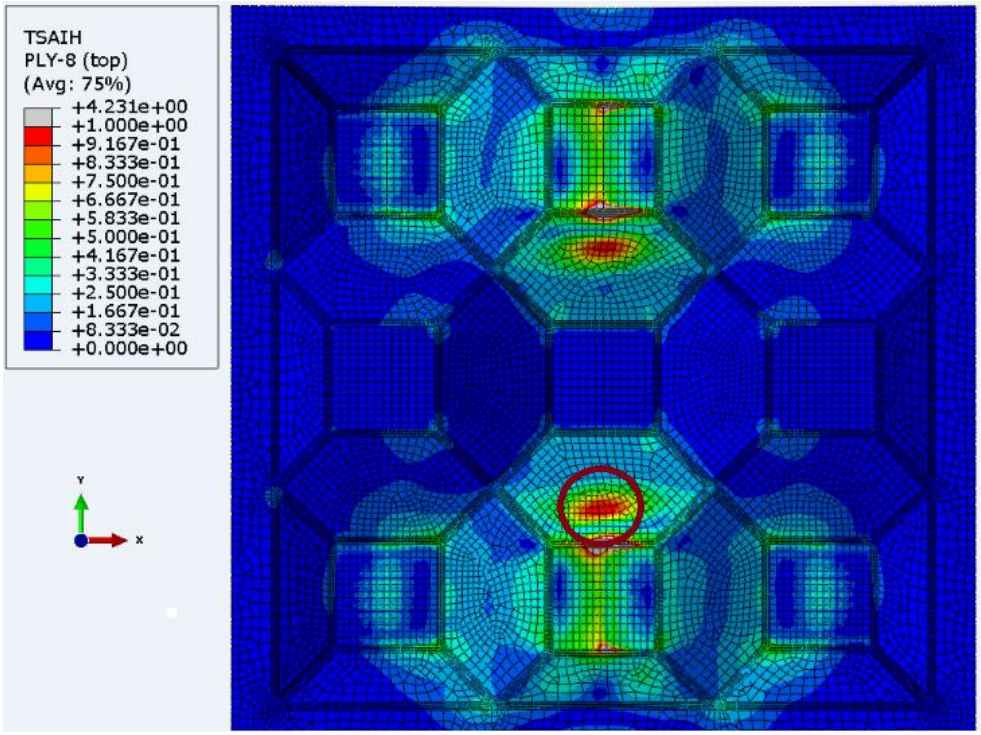

Figure 7.25. The predicted failure region.

Figure 7.26 shows the distribution of the maximum in-plane principal stress values of the centroid of the element 14005 of the core through the thickness. 0-mm position corresponds to the bottom, while 1.44 mm corresponds to the top. As seen in Figure 7.21, the top layer of the predicted failure region is in tension. The change of Tsai-Hill failure index values through the thickness of the element 14005 of the core is shown in Figure 7.27. From Figures 7.21 and 7.26, it is possible to say that the stress state at the core wall where element 14005 belongs is changing from compression at the bottommost point to tension at the topmost point, imitating the deformation under bending moments as expected, which means that the corresponding region of the core buckles outward. From

Figures 7.26 and 7.27, one can say that the failure occurs at the topmost layer under tension. Similarly, the bottommost layer is about to failure under compression. However, the failure index values at the inner layers of the core are lower than the topmost and the bottommost layers. Note that the surface quality of the manufactured core is not perfect due to the manufacturing method, and therefore the stress state predicted by the FE model is not perfectly accurate.

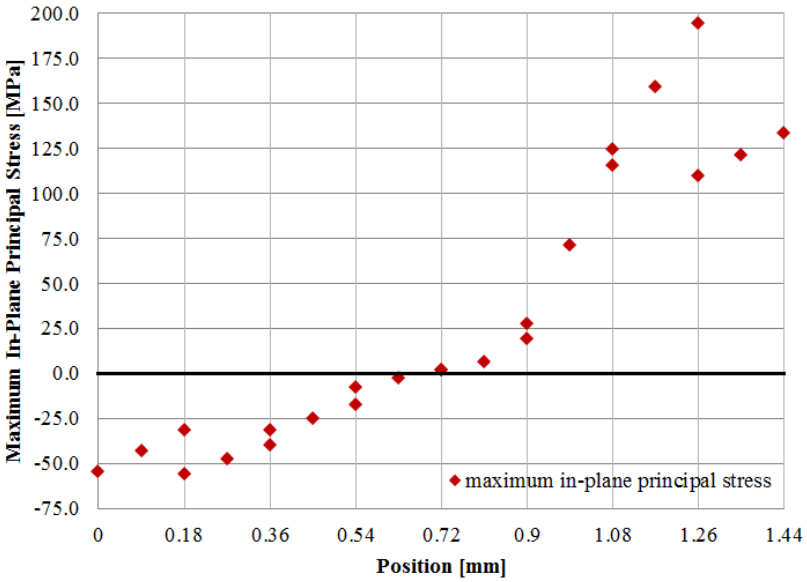

Figure 7.26. The distribution of the average maximum in-plane principal stress values of the element 14005 of the core through the thickness.

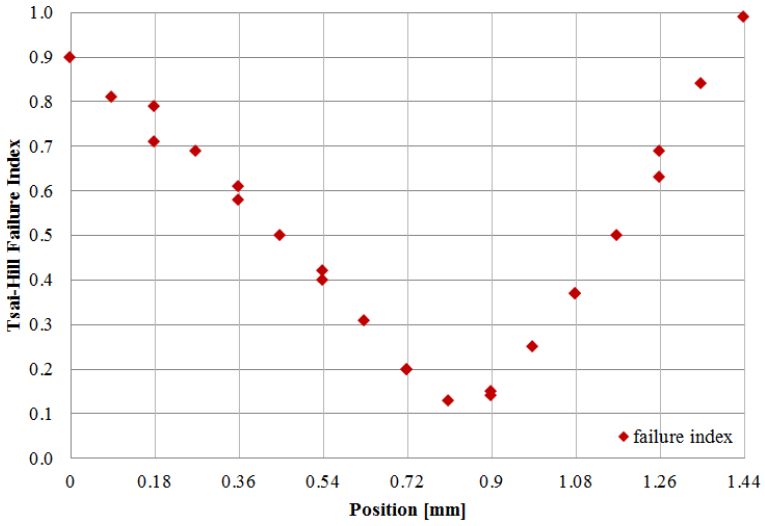

Figure 7.27. The change of Tsai-Hill failure index values through the thickness of the element 14005 of the core.

The force on the bar corresponding to the deflection of 5.91 mm is measured as 3720 N in the experiment of plate 2 and 3630 N in the experiment of plate 3. Figure 7.28 shows the distribution of the AE data for the second specimen according to the peak frequency values. The FE model predicts the initial failure when the deflection of the middle bar reaches 5.91 mm. That level of deflection was obtained at the 312nd second of the experiment conducted on the second plate, which is shown by an arrow on the plot. As seen in Figure 7.28 clearly, the AE setup started detecting acoustic waves at 320th second of the experiment of the second plate. Figure 7.29 shows the distribution of the AE data for the third specimen according to the peak frequency values. The 5.91 mm deflection of the middle bar was obtained at the 318th second of the experiment conducted on the third plate, which is shown by an arrow on the plot. The finite element model estimates the corresponding reaction force as 4590 N. Considering that viscoelastic effects and material nonlinearity are neglected in the finite element model, the accuracy of the predictions is acceptable. On the other hand, the prediction of the region for the initial failure is quite successful. As seen in Figure 7.25, the model predicts the initiation of the failure within the encircled region. With the increasing deflection values of the middle bar, the shape of the failed region resembles croissant (Figure 7.23f) and for the further deflection of the middle bar, the failed region is expected to be at exactly the same region where failure is observed as shown in Figure 7.12b.

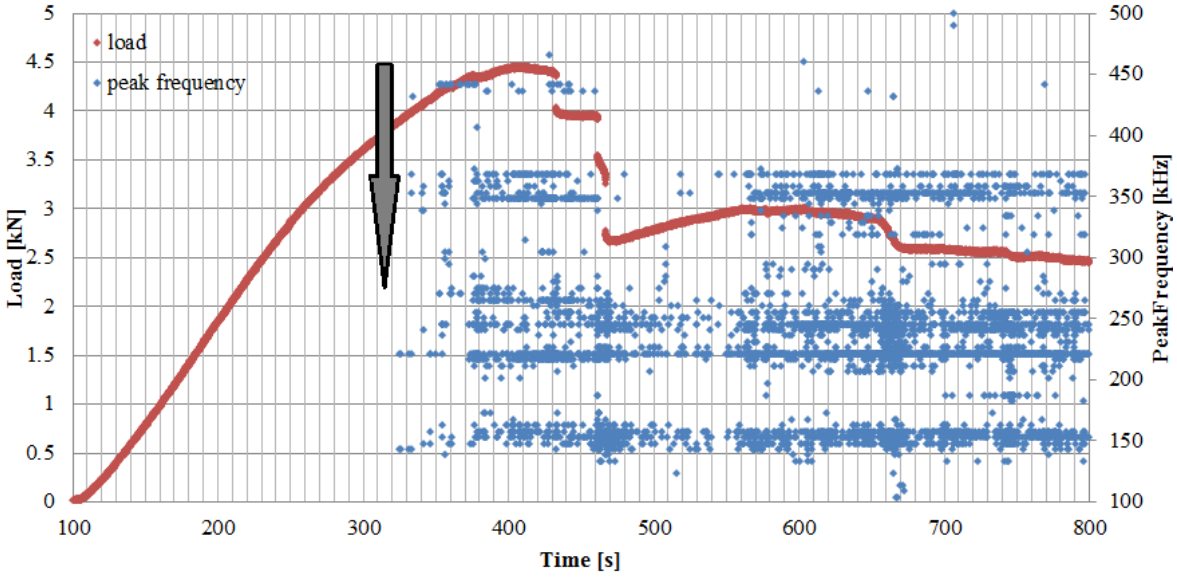

Figure 7.28. The distribution of the AE data for the second specimen according to the peak frequency values.

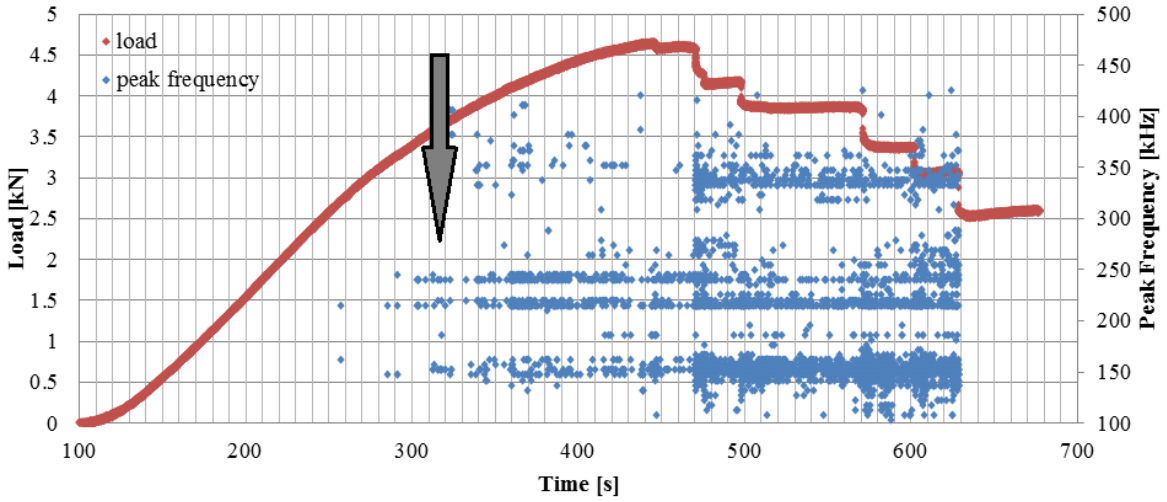

Figure 7.29. The distribution of the AE data for the third specimen according to the peak frequency values.

7.3. Comparisons

The FE model developed for the sandwich structure with the particular core design is used to investigate its advantages and disadvantages in terms of performance.

7.3.1. Stiffness Gain

In order to calculate the stiffness gain, a plain laminated plate with the same lamina thicknesses and stacking sequence is also modeled. The thicknesses of the bottom, middle and top layers are equal to 1.20 mm, 1.44 mm and 1.20 mm, respectively. Each of these segments has eight plies with the same stacking sequence, which is $[0/45/-45/90]_s$. The equivalent plate has 24 plies with the same stacking sequence $[0/45/-45/90]_{3s}$ and its thickness is equal to 3.84 mm. This is also equal to the total thickness of the bottom face, the core and the top face of the sandwich structure. The FE model of the equivalent plate is subjected to the same loading conditions by setting the deflection of the middle bar, U3, to 8.0 mm, with the use of the same rubber bands between the surfaces of the plate and the bars. Figure 7.30 shows the load vs. middle bar deflection curves of the FE model of the sandwich specimens with the rubber bands, the test data for the second and third specimens and the FE model results for an equivalent plate. One may come up with a conclusion that the agreement between the FE model of the sandwich structure with this particular core

design and the actual mechanical response of the sandwich structure is acceptable. As seen in Figure 7.30 clearly, although the sandwich structure has almost the same weight with the equivalent plate, its stiffness is approximately 4.5 times of the equivalent plate's stiffness. The stiffness gain for the sandwich structure with this particular core design is satisfying.

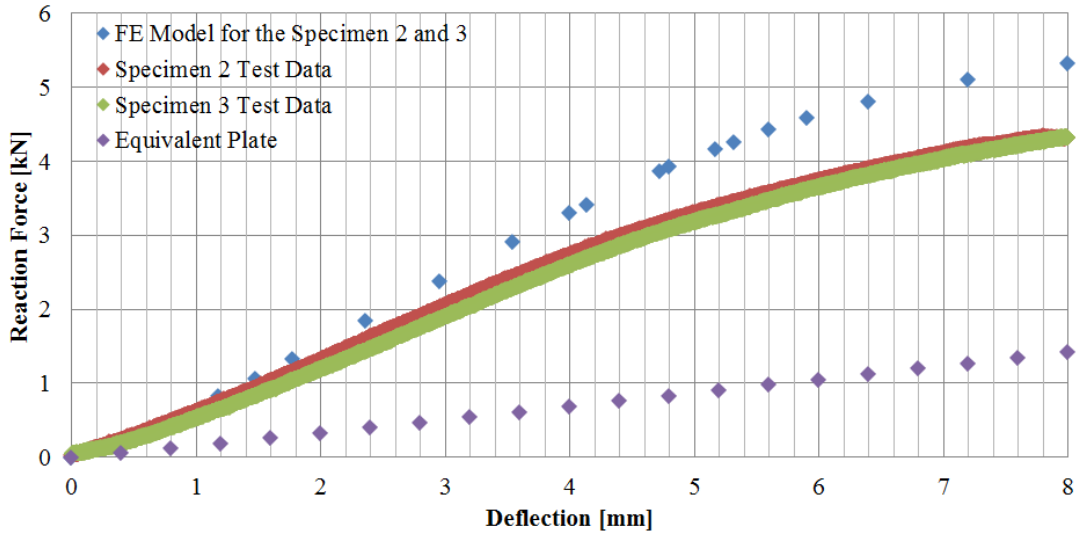

Figure 7.30. Load vs. middle bar deflection curves for the FE model of the sandwich specimens with rubber bands, the test data for the second and third specimens and the FE model of an equivalent plate.

For the sandwich specimens, the FE model predicts failure when the deflection of the middle bar reaches 5.9 mm as seen in Table 7.1. For the same loading condition, the FE model calculates the maximum failure index value as 0.21 on the top layer of the equivalent plate.

7.3.2. Unit Cell Effect

In order to observe the effect of the unit cell, a 5x3 architecture is modeled instead of a 3x3 architecture. Figure 7.31 presents the distribution of the deflection state of the sandwich structure with the same unit cell geometry, but with a wider core. Figure 7.32 shows the calculated reaction force on the middle bar vs. the deflection of the middle bar for the 3x3 and the 5x3 FE models. While keeping the distance between the rigid bars and the other dimensions of the sandwich structure the same, the length of the core is increased by adding two columns of unit cells. If a homogenous material were tested under bending,

outer regions beyond the lower bars would not influence on the mechanical response of the specimen, because these regions would be stress free. Therefore, the total length of the part should not be a parameter which affects the characteristics. However, it is observed that the flexural stiffness increases when the plate is widened as seen in Figure 7.32. One may conclude that the size of the unit cell is not small enough compared to the dimensions of the specimen and influences the mechanical response of the structure. Specimen preparation with different geometries may result in different characteristics. In order to predict the mechanical behavior of a plate with much wider size, one should consider the size effect of the unit cell.

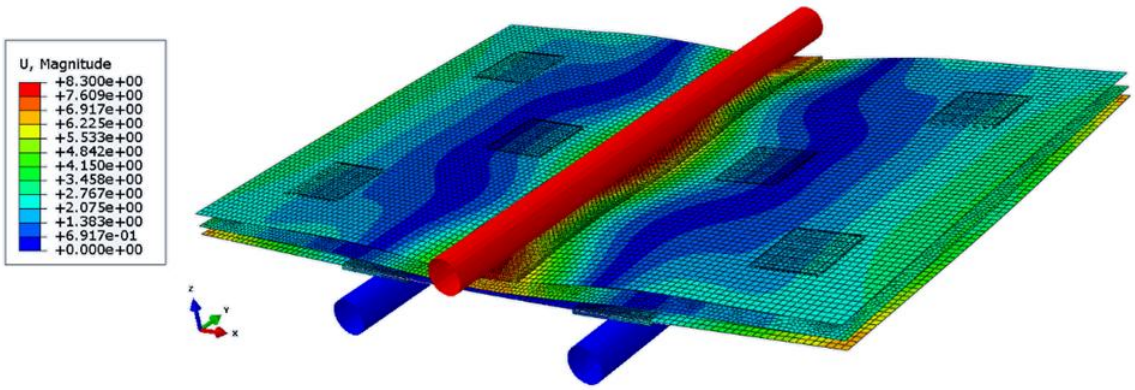

Figure 7.31. Deflection state of the sandwich structure with the same unit cell geometry and the testing conditions, but with a longer core.

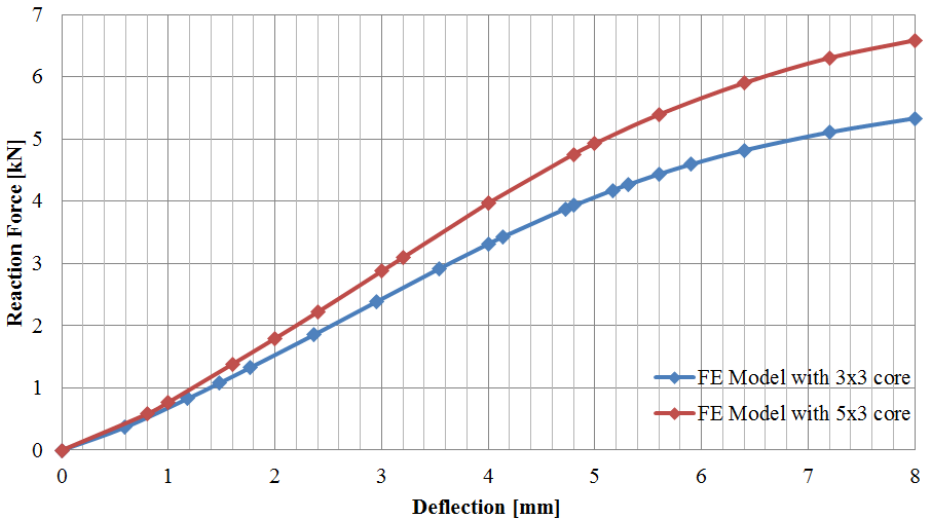

Figure 7.32. The calculated reaction force on the middle bar vs. the deflection of the middle bar for the 3x3 and the 5x3 FE models.

7.3.3. FE Simulations for Quasi-Static Crushing Test

In order to understand the mechanical behavior of the sandwich structure with the particular core design and the same stacking sequences under out-of-plane pressure, a FE model is developed which simulates the flatwise compression test. Contrary to the three-point bending tests, the model is not developed in full size. Instead, it represents a portion of a much wider plate under out-of-plane compression. For this purpose, 200 mm to 200 mm portion of the sandwich structure is modeled and symmetry boundary conditions are assigned in *x* and *y* directions. For the edges in the *x*-direction, U1, UR2, and UR3 are set to zero. Similarly, U2, UR1, and UR3 are set to zero for the edges in the *y* direction. Rigid plates are modeled and placed above and below the sandwich structure. The lower rigid plate imitates a rigid flat surface while the upper rigid plate imitates the crosshead of the compression test machine. In order to do that, the lower rigid plate is fixed by setting the displacements all degrees of freedom, U1, U2, U3, UR1, UR2, and UR3, to zero. For the upper rigid plate, only the vertical motion, U3, is allowed. The boundary conditions for the model are shown in Figure 7.33. The compression load in the *z* direction is applied through the reference point of the upper rigid bar. The maximum compression load is set to 17 kN, which corresponds to 0.425 MPa pressure. The corresponding load vs. deflection curve obtained by the FE model is depicted in Figure 7.34. Up to 0.6 mm deflection, the relation is linear, then it starts to become nonlinear.

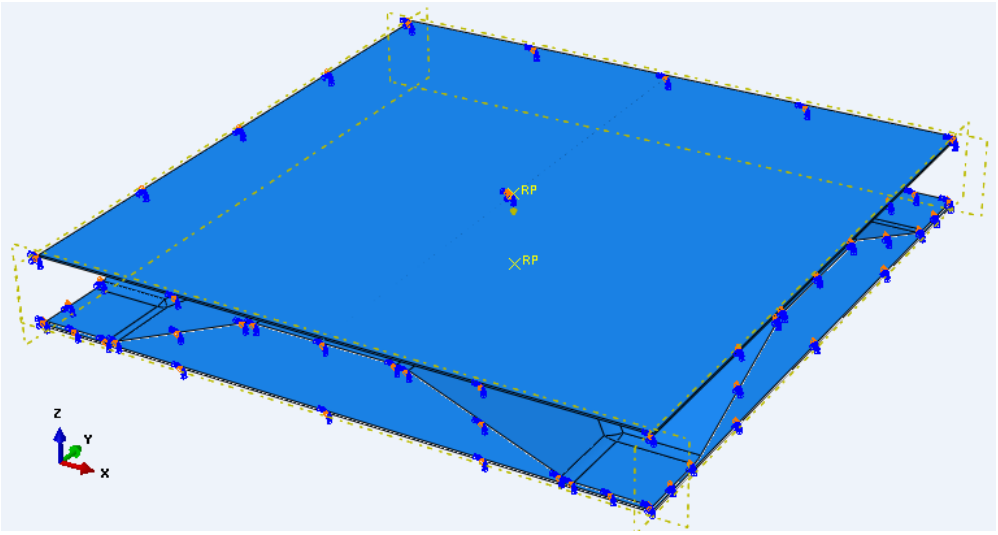

Figure 7.33. The boundary conditions of the model for the flatwise compression test.

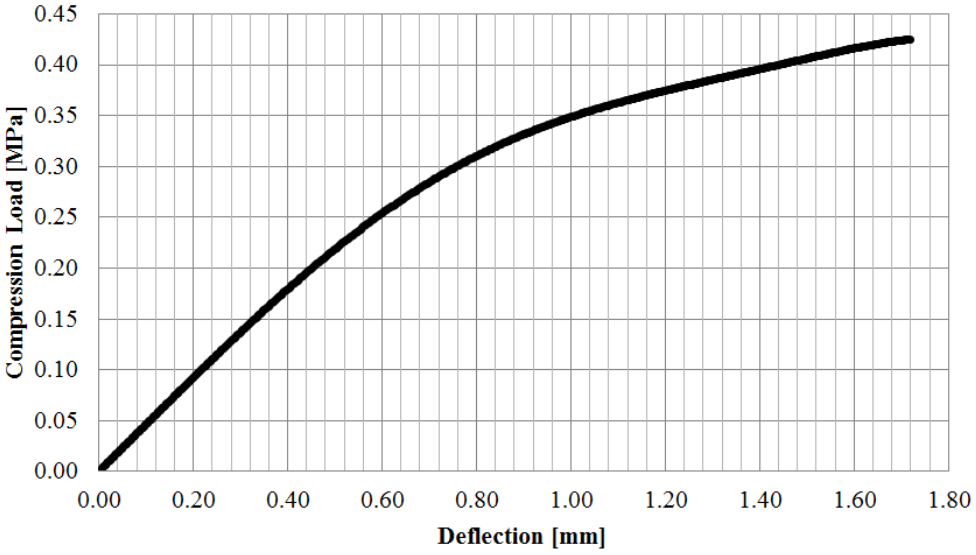

Figure 7.34. Load vs. deflection curve for the simulation of the flatwise compression test.

The compressive modulus of the sandwich plate is calculated as 11 MPa in the linear range. The weight density of the particular design is 110 kg/m^3. Compared to the honeycomb-cored sandwich structures with similar weight densities, 11 MPa is low as the compressive modulus. Therefore, use of this sandwich construction is not suitable for applications where the transverse rigidity is critical. For epoxy-based honeycomb cores, the compressive modulus changes between 15 MPa and 30 MPa. It can reach up to 80 MPa [71, 91-94]. One should note that when the honeycomb structures are subjected to flatwise compressive loads, their load bearing capabilities decrease dramatically after localized core buckling [95]. On the other hand, thick flat panels may withstand relatively high compressive loads after buckling deformation initiates, which may happen for the case of the particular core design in this study. When the pressure reaches 0.25 MPa, the compressive modulus starts to decrease. This may be the result of the geometric nonlinearity and inception of buckling deformation of the core walls. For 0.25 MPa, the upper rigid plate displaces 0.59 mm in -*z* direction. As seen in Figure 7.35, showing the vertical deflection state of the core, in some regions of the core, the displacement of the core walls starts exceeding the deflection of the upper rigid plate. This might be a sign of buckling deformation. The vertical deflection state of the core under 0.40 MPa is shown in Figure 7.36. Although the corresponding vertical displacement of the upper rigid plate in -*z* direction is only 1.44 mm, some wall regions of the core move almost 2 mm in +*z* direction and some other wall regions of the core move almost 3.67 mm in –*z* direction. One may

conclude that the core walls have already buckled and this deformation decreases the compressive modulus. In order to predict the post-buckling behavior of the sandwich structure with the particular core design, the FE model should be improved.

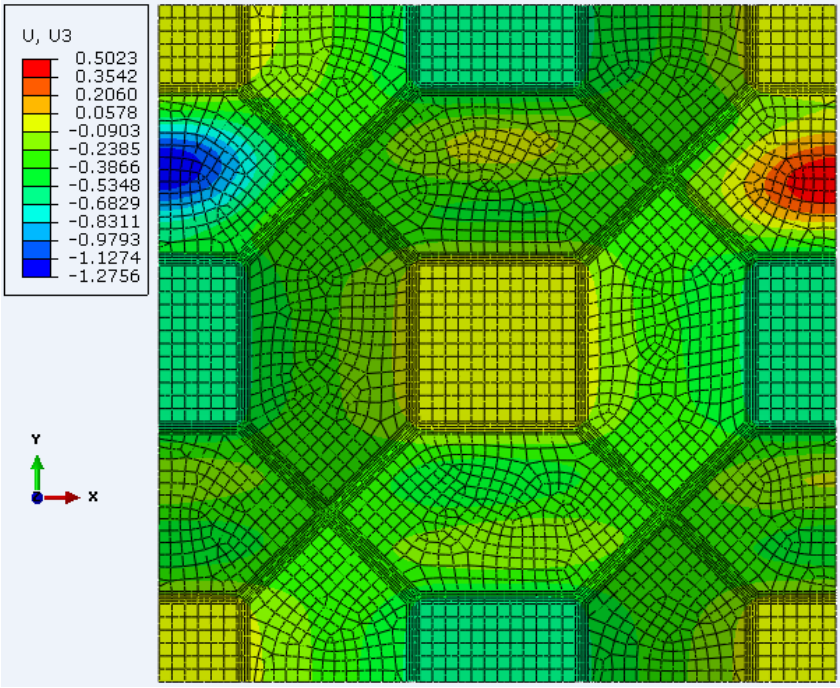

Figure 7.35. The vertical deflection state of the core under 0.25 MPa.

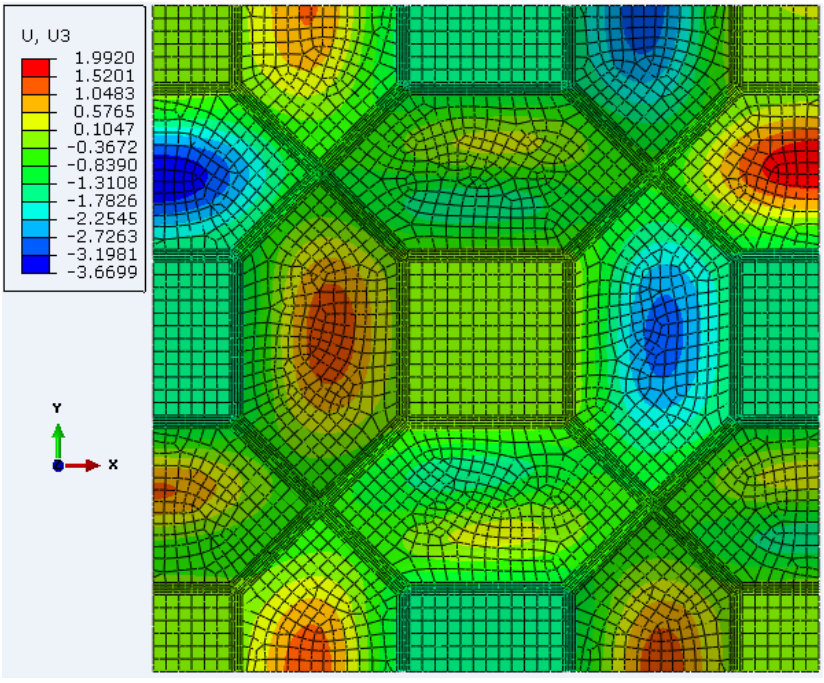

Figure 7.36. The vertical deflection state of the core under 0.4 MPa.

7.3.4. FE Simulations for Indentation Tests

In order to investigate the failure behavior of the sandwich structure with the particular core design under concentrated loads, two different indentation tests are simulated. In the first case, the indenter applies a load on a region of the face sheet where the bonded core supports the face sheet (Figure 7.37). In the second case, the indenter applies load on a region of the face sheet with no core support.

For each test simulation, rigid and blunt cylinders with three different sizes are used. For the indenters, the diameters of the contact area are 4 mm, 10 mm, and 16 mm. In the simulations, the same FE model is developed for the simulation of the transverse compression tests is used except that instead of a rigid plate on top, three different indenters are modeled as rigid parts. The indentation load is defined at the reference points of the indenters and the FE model increases the load gradually during the simulations.

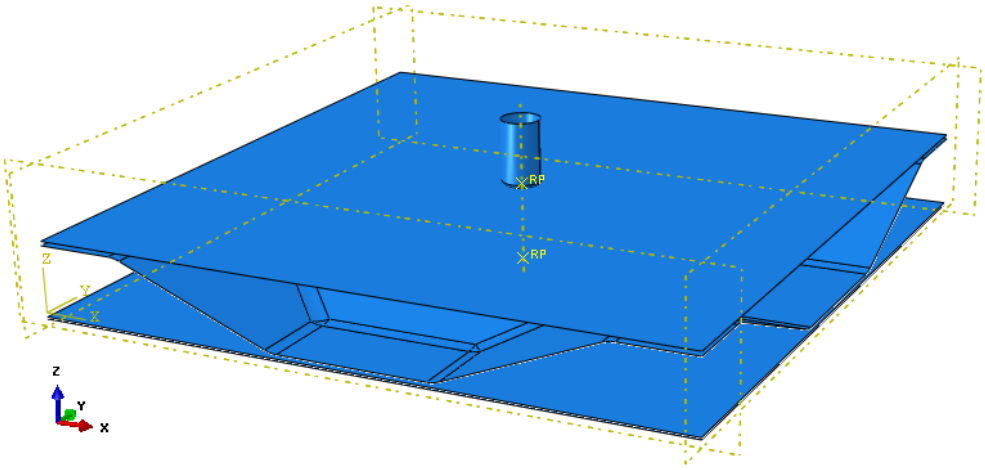

Figure 7.37. The FE model for the first case with the 10 mm of indenter diameter size.

In the first case, the indentation loads are selected as 800N, 1300N, and 1800N for the indenter one, two, and three, respectively. The corresponding load vs. indentation curves are depicted in Figure 7.38. With the indenter one, the FE model predicts failure at the bottom layer of the core beneath the indenter when the indentation load reaches 627 N and the indenter deflection is 0.62 mm. The corresponding indentation pressure is calculated as 49.9 MPa. The fibers at the bottom layer of the core are aligned with the x direction and right beneath the indenter, S11 is equal to 290 MPa, S22 is equal to 70 MPa

and Tsai-Hill failure index is equal to 1.0 for the bottom layer of the core at that region. Since the transverse tensile strength of the lamina is equal to 75 MPa, the mode of failure should be matrix cracking. Figure 7.39 shows Tsai-Hill failure index distribution at the bottom layer of the core beneath the indenter for different indentation loads. The upper limit of the scale is selected as 1.0 and the grey regions are assumed to have failed. Figure 7.39a corresponds to 627 N of indentation load. Figure 7.39b, c, and d correspond to 686 N, 766 N, and 800 N of indentation loads, respectively. As seen in Figure 7.39, although Tsai-Hill failure index exceeds 1.0 at 627 N, the affected zone is quite small compared to the size of the specimen. Therefore, the specimen is expected to withstand further loading. In order to understand the behavior of the specimen after the initiation of the failure, the FE model should be improved for a progressive failure simulation. Similarly, FE model predicts failure in the sa3me region for the second and third indenters. With the indenter two, the failure is predicted when the indentation load reaches 1160 N at 1.04 mm of the indenter deflection and with the indenter three, the failure is predicted when the indentation load reaches 1605 N at 1.15 mm of the indenter deflection. The corresponding indentation pressures are 14 MPa and 8 MPa with the indenter two, and three, respectively. The stress levels in the *x* and *y* directions where failures are predicted for the indenter two and three are almost same as the one for the indenter one.

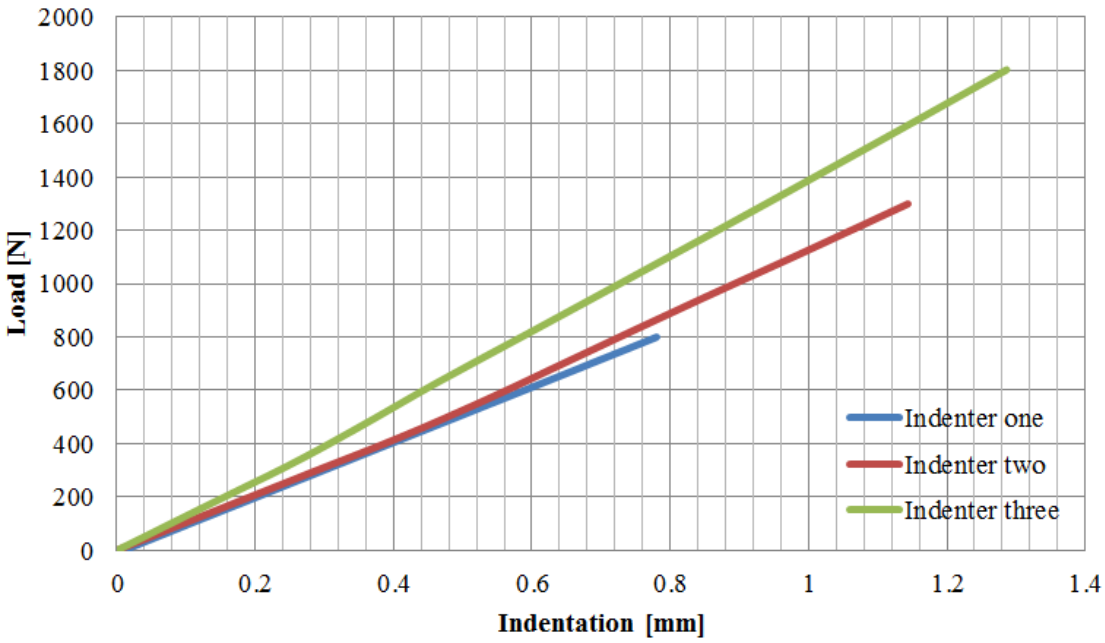

Figure 7.38. The load vs. indentation curves obtained by simulating the first indentation test with different indenters.

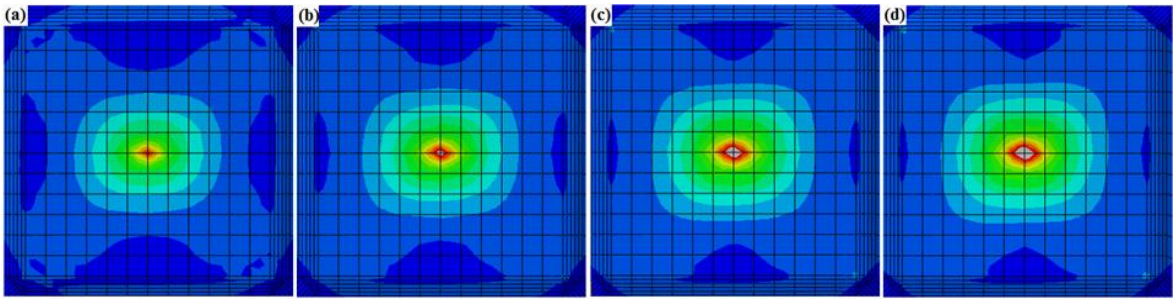

Figure 7.39. Tsai-Hill failure index distribution at the bottom layer of the core beneath the indenter for different indentation loads; (a) 627 N, (b) 686 N, (c) 766 N, and (d) 800 N.

For the second case, the indentation loads are selected as 400N, 400N and 800N for the indenter one, two, and three, respectively. The corresponding load vs. indentation curves are depicted in Figure 7.40. With the indenter one, the FE model predicts failure at the bottom layer of the top face beneath the indenter when the indentation load reaches 215 N and the indenter deflection is 3.42 mm. The corresponding indentation pressure is calculated as 17.1 MPa. The fibers at the bottom layer of the top face are aligned along the *x*-direction. Right beneath the indenter, S11 is equal to 291 MPa, S22 is equal to 69 MPa and Tsai-Hill failure index is equal to 1.0 for the bottom layer of the top face at that region. Since the transverse tensile strength of the lamina is equal to 75 MPa, the mode of failure should be matrix cracking. With the indenter two, the failure is predicted when the indentation load reaches 340 N at 4.07 mm of the indenter deflection and with the indenter three, the failure is predicted when the indentation load reaches 560 N at 4.80 mm of the indenter deflection. The corresponding indentation pressures are 4.3 MPa and 2.8 MPa with the indenter two, and three, respectively. The stress levels in *x* and *y* directions where failures are predicted for the indenter two and three are almost the same as the ones for the indenter one. Figure 7.41 shows Tsai-Hill failure index distributions at the bottom layer of the top face sheet with the same magnification when the failure occurs with three different indenters.

For the both cases with three different indenters, the predicted failure mode is matrix cracking at the bottommost layer beneath the indenter due to the tensile load in transverse direction. The affected zone of the sandwich plate deforms similar to the deformation of a large panel under transverse loads since the topmost layer is subjected to compressive loads while the bottommost layer is subjected to tensile loads. Due to the assigned stacking

sequence, the transverse stress levels for the bottommost layers exceed transverse tensile strength of the lamina. On the other hand, the localized failure of the bottommost layer due to the matrix cracking does not necessarily mean the failure of the structure since the maximum failure index level in other laminae are lower than the level at the bottommost layer. The size of the indenter also influences the failure load level.

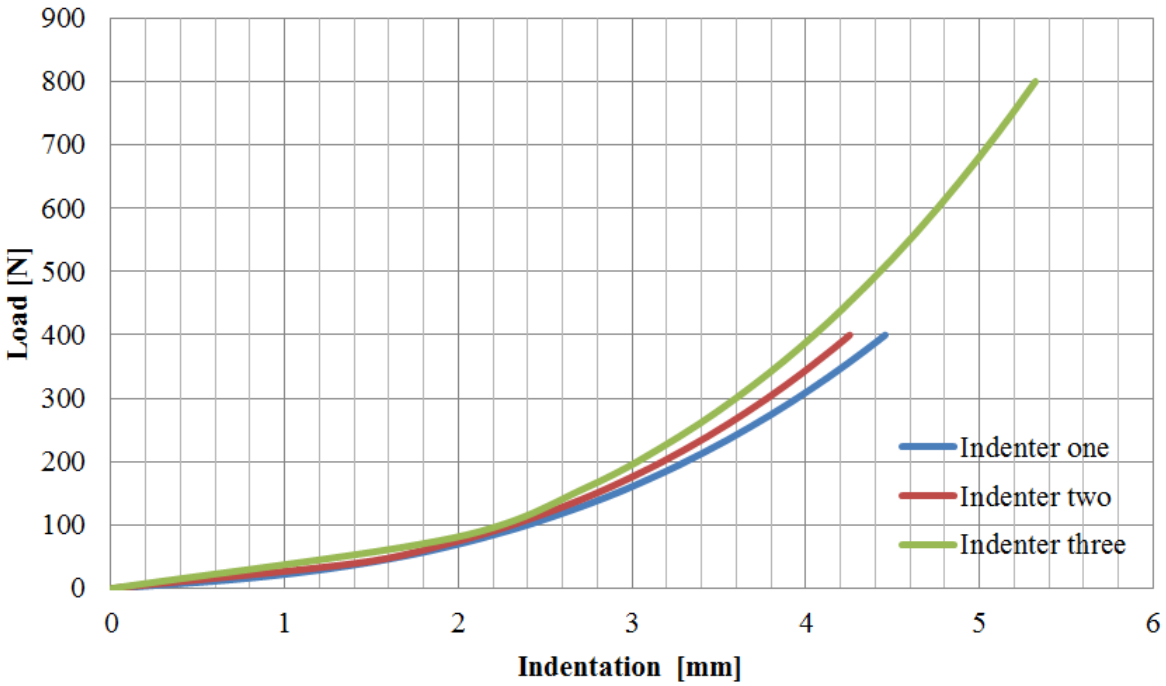

Figure 7.40. The load vs. indentation curves obtained by simulating the second indentation test with different indenters.

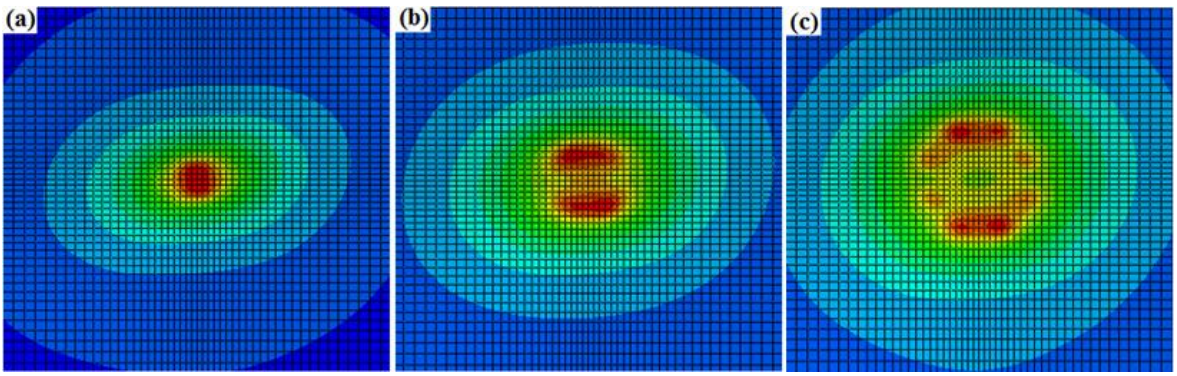

Figure 7.41. Tsai-Hill failure index distributions at the bottom layer of the top face sheet when the failure occurs in case two with (a) indenter one, (b) indenter two, and (c) indenter three.

8. CONCLUSION

In this study, the failure behavior of undulated sandwich plates with a new core design is investigated. E-glass-fiber-reinforced epoxy is selected for the components of the structure. By using micromechanics, some of the direction dependent lamina properties are determined. Strength properties are found by performing tension tests on specimens with cross-ply and quasi-isotropic layups under acoustic emission monitoring. In order to obtain properties in the principal material directions, the classical lamination theory is used. The missing properties are taken from the literature.

The failure mechanisms of glass-fiber reinforced epoxy laminates are investigated by acoustic emission monitoring method. Matrix cracking, interfacial debonding, interlaminar debonding (delamination), fiber pull-out, and fiber breakage are important failure mechanisms that lead to failure of composite structures. The collected acoustic emission data are post-processed and classified in order to correlate the data with the failure mechanisms, identify activated failure modes, and understand the failure response. Beside the parameter based approaches, fast Fourier transform (FFT) is done in order to investigate signals in the frequency domain. A Visual Basic code is written to carry out FFT and evaluate each hit datum. The frequencies of the generated acoustic waves originating from the same failure mechanism are known to lie in the same frequency band; therefore the frequency bands determined for a particular material can be used to identify the failure mode. For the glass-fiber-reinforced epoxy composite laminates tested in this study, the dominant frequencies of matrix cracking, delamination, debonding and fiber breakage are observed to be in the 140-160 kHz band, 180-230 kHz band, 230-270 kHz band, and 340-360 kHz band, respectively.

In order to understand the failure behavior under out-of-plane loading, sandwich laminates are manufactured and tested with a three-point bending under real-time acoustic emission monitoring. The collected AE data are post-processed and classified according to their dominant frequency characteristics. It is found out that under lateral forces, the sandwich plates with the unique core design can withstand loads up to 5 kN and still carry loads even after vertical deflection reaches the three times of plate thickness. This unique

design has a linear respond up to 3 kN, which is followed by matrix cracking and fiber-matrix debonding, especially in the face, which carries tensile loads. If rubber bands are placed between the bars of the three-point bending fixture and the laminate surfaces, stress concentration on the loading area may be reduced; the damage on the face sheets can be delayed. In the deflection controlled experiments, after leaving the peak load level behind, the structure are observed to withstand further deformation without catastrophic failure. After some point, extensive fiber failures are observed; then the part can carry relatively low forces.

To predict the failure behavior of the sandwich plate, a parametric Python Script code is written to model the structure and simulate three-point bending tests. As the failure criterion, Tsai-Hill failure criterion is adopted. The failure load is found by integrating the secant algorithm to the Python code. An iterative study is conducted and the outcome is compared with the experimental results. In terms of predicting the region of failure, a great agreement with the experimental results is observed. For the macroscopic behavior, the agreement is adequate for the general understanding because of the fact that the results are highly sensitive to material characteristics.

8.1. Future Work Recommendations

The developed finite element model is beneficial for predicting initial failure behavior. In order to understand the progressive failure mechanisms at sandwich plates, the model may be improved.

The geometry of the structure and the stacking sequences are given as parameters in the code for the finite element model. It is possible to change the geometry of the whole model by just changing a couple of parameters, such as size of unit length, depth of the core, number of unit cells, core wall angles, ply orientations and the code manages to create the new model with new design, successfully. Therefore, an optimization algorithm may be followed with the written Python code in order to find optimum structural design with the aforementioned core design.

APPENDIX A: VACUUM INFUSION PROCESS

Vacuum Infusion Process (VIP) is a popular technique to manufacture laminated large composite structures. The technique is based on creating vacuum pressure to drive liquid resin into a laminate. The reinforcing materials such as carbon fiber or glass fiber layers are placed dry into the mold and the vacuum is applied before introducing the resin. Achieving a complete vacuum via proper tubing and sealing is followed by suction of resin into the laminate. Vacuum infusion process provides consolidated and stronger composite laminates with higher quality and improved material properties [69].

Resin infusion methodology dates back to 1960s and open mold process had been preferred widely for many applications for decades [96]. However, thanks to evolution of vacuum infusion process from an expensive method to a commercially feasible solution, VIP has become a competitive technique and viable option for many applications in the industry. Several variations of this technique have been created over years, which led to different acronyms such as VARTM, RIFT and SCRIMP [97]. All the vacuum infusion techniques follow the same fundamental principles with some minor differences in process or technology. Basically, they all describe a methodology which is based on impregnation of dry reinforcement by liquid resin with the help of vacuum pressure. Among several acronyms, VARTM (Vacuum Assisted Resin Transfer Molding), VBRTM (Vacuum Bag Resin Transfer Molding), RIFT (Resin Injection under Flexible Tooling), SCRIMP (Seemann Composites Resin Infusion Molding Process) and VARI (Vacuum Assisted Resin Injection Process) are mostly preferred names to refer vacuum infusion process [98]. Although VARTM is defined as a modified version of resin transfer molding process, which is a closed-mold process using male and female molds to form composites under low pressures, it is commonly used to refer vacuum infusion process.

Instead of using two molds to form the composite as in RTM technique, VIP contains only a single mold or a glass surface. The surface of the mold is carefully coated by mold-release wax to prevent resin from infusing into the mold or sticking on it. In addition to that, if the wax is not used, the operator has to use force to remove the manufactured part from the mold. These actions may easily damage the produced parts and also the mold

during repetitive applications. Wax coating is followed by placement of dry reinforcement onto the mold. These reinforcing materials have to be separated from the other components of the setup by a peel ply layer. The flow rate of the viscous and soon-to-be-solidified resin may not be high enough to ensure a successful resin penetration into the whole cavities at the part under high vacuum pressure. Therefore, the resin flow is assisted by a flow mesh sheet which can unify with the part if there is no separating peel ply layer in between. Covering the reinforcement with peel ply is followed by placing flow mesh and spiral tubes. The whole area is sealed by a vacuum bag. The schematic setup is demonstrated at Figure A.1 and taken from the studies of Correira *et al.* [99].

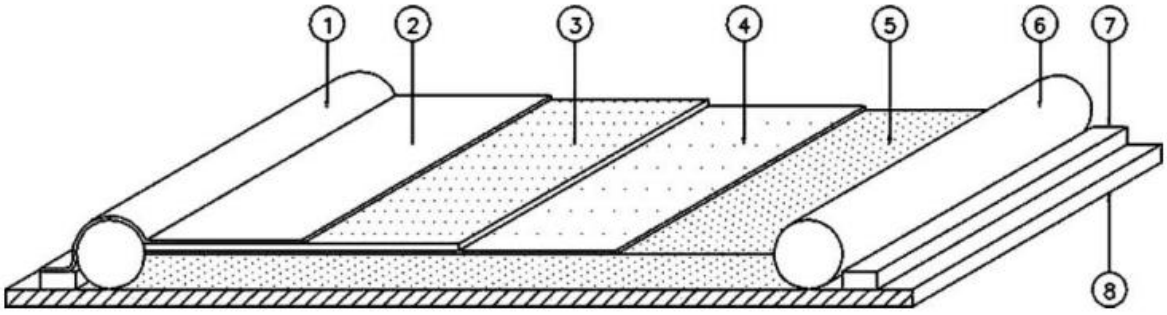

Figure A.1. 1-inlet, 2-vacuum bag, 3-flow mesh, 4-peel ply, 5-reinforcement, 6-outlet, 7-sealing tape, 8-thick glass [99].

The setup contains an inlet for the resin entrance and an outlet for the air extraction. Before letting the resin being sucked into the cavities of the reinforcement, the air is extracted from the outlet to create an initial vacuum ambient. This strategy allows the operator to check the setup for any leakage and to preform the composite. Suction of air during the resin penetration creates air entrapped regions in the composite and this may lead to wasting of the whole part. The whole process needs a careful planning and control since error correction is almost impossible.

Once the setup is checked, the resin is allowed to penetrate into the reinforcement. As seen in the illustration of the general sequences, a resin trap is placed between the vacuum pump and vacuum outlet to protect the pump from sucked out excessive resin [69] (Figure A.2). Although the amount of required resin can be approximately calculated, the operator is advised to prepare resin more than the required amount to avoid fatal air entrance.

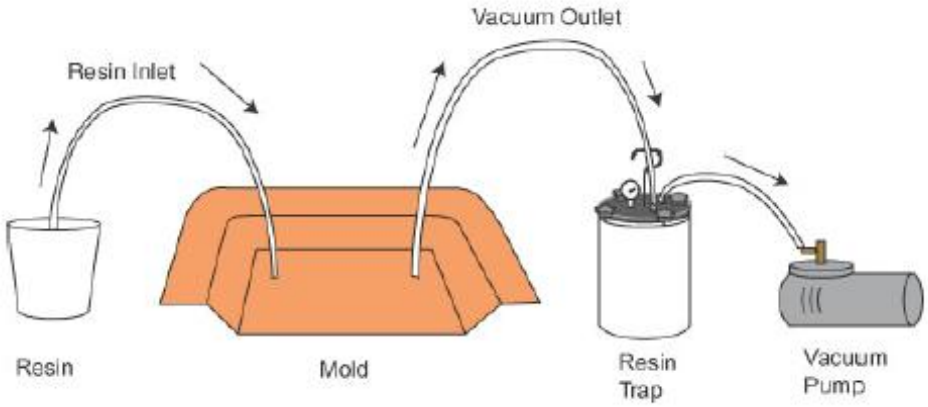

Figure A.2. The schematic representation of VIP [69].

The resin is produced by adding a hardener agent into laminating resin. Once the resin material is prepared, the mixture has a pot life before hardening. Hence, the resin should be prepared after building and testing the setup. The vacuum pump should keep working until the resin solidifies. The total curing time may vary and the final product can be subjected to heat treatment.

Vacuum infusion process has the following advantages in fabricating large composite laminates.

- VIP provides higher fiber-to-resin ratio. Increasing the fiber content in the unit volume by sucking excess resin out into the outlet improves the mechanical properties of the final product.

- Compared to open mold process, a laminate produced by VIP and consolidated with no air entrapment will have increased quality.

- The process is almost independent from the skills of operator. Any fault may easily ruin the part, but on the other hand, a successful process is able to give almost the same quality at each time. Ability to retain the quality is beneficial for repetitive applications.

- The process is suitable for different sizes and shapes. Complex geometries can be produced within one step which eliminates further bonding operations.

- The total required resin can be calculated successfully. Hence, the amount of wasted resin is kept in minimum and the usage is highly predictable.

- Initial vacuum ambient for dry reinforcement enables the operator to notice any leakage problem. Since there is no ticking resin clock against the operator, any problem can be solved before introducing liquid resin.

- It reduces styrene emissions significantly. The working conditions are cleaner and safer

- Part shrinkage and distortion are quite low.

Similar to any laminating process, Vacuum infusion process conveys some potential drawbacks such as sensitivity to leakage and preparation time. Although VIP is undeniably beneficial for better part quality with better mechanical properties compared to other production techniques, the following pitfalls need to be taken into account during the whole process:

- The place of the second mold in RTM technique is taken by vacuum bag which is a flexible membrane and its nature makes the setup sensitive to leakage.

- Since the process is irreversible, any potential error may not be corrected. Therefore, it is easy to ruin the part. This fact requires higher control and better planning of the process rather than its alternatives.

- Due to the complexity of the setup, the preparation takes longer time.

- Smooth surface can be obtained at one side only.

- Although VIP is a cleaner process, some hazardous chemicals such as cleaners, wax, resin and releasing agents are still in-use. The operator should wear gloves and provide ventilation for the room to avoid undesired consequences.

APPENDIX B: MICROMECHANICS AND CLASSICAL LAMINATE THEORY

The components of stiffness matrix are calculated by using the material constants of the lamina in designated directions. However, the lamina constants have to be calculated by following rules of mixture method. Rule of mixture is a methodology for composite materials that predicts material constants by using the properties of reinforcement and matrix material and their volumetric fractions. It is especially reliable for laminates made of unidirectional continuous fibers. Equations B.1-B.4 can be derived from the rule of mixtures [6].

$$E_1 = E_f V_f + E_m(1 - V_f) \tag{B.1}$$

$$E_2 = \frac{E_f E_m}{E_m V_f + E_f(1 - V_f)} \tag{B.2}$$

$$\frac{1}{G_{12}} = \frac{V_f}{G_f} + \frac{(1 - V_f)}{G_m} \tag{B.3}$$

$$\nu_{12} = \nu_f V_f + \nu_m(1 - V_f) \tag{B.4}$$

In Equations B.1-B.4, indices f and m refer to fiber and matrix, respectively. V represents the volumetric fractions and 1 indicates the fiber direction while 2 corresponds to transverse directions. Using these calculated material constants according to fiber 1 and 2 directions, stiffness matrix according to 1-2 axes is found by Equations B.5-B.10.

$$[Q] = \begin{bmatrix} Q_{11} & Q_{12} & 0 \\ Q_{12} & Q_{22} & 0 \\ 0 & 0 & Q_{66} \end{bmatrix} \tag{B.5}$$

$$Q_{11} = \frac{E_{11}}{1 - \nu_{12}\nu_{21}} \tag{B.6}$$

$$Q_{12} = \frac{\nu_{12}E_{22}}{1-\nu_{12}\nu_{21}} \tag{B.7}$$

$$Q_{22} = \frac{E_{22}}{1-\nu_{12}\nu_{21}} \tag{B.8}$$

$$Q_{66} = G_{12} \tag{B.9}$$

$$\nu_{12}E_{11} = \nu_{21}E_{22} \tag{B.10}$$

[Q] assumes 1 direction coincides with fiber orientation. As stated previously, these directions do not always coincide with desired axes and a transformation has to be done.

Transformation of the matrix to the different axes can be done by setting θ value, shown in Figure B.1 [3], as the angle between fiber direction and desired direction.

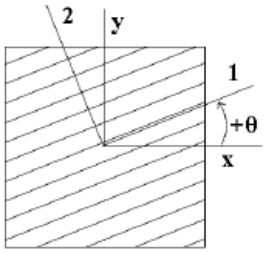

Figure B.1. Unidirectional lamina under off-axis loading [3].

$$[\bar{Q}] = \begin{bmatrix} \bar{Q}_{11} & \bar{Q}_{12} & \bar{Q}_{16} \\ \bar{Q}_{12} & \bar{Q}_{22} & \bar{Q}_{26} \\ \bar{Q}_{16} & \bar{Q}_{61} & \bar{Q}_{66} \end{bmatrix} \tag{B.11}$$

$$\bar{Q}_{11} = Q_{11}cos^4\theta + 2(Q_{12} + 2Q_{66})sin^2\theta cos^2\theta + Q_{22}sin^4\theta \tag{B.12}$$

$$\bar{Q}_{12} = Q_{11}sin^4\theta + 2(Q_{12} + 2Q_{66})sin^2\theta cos^2\theta + Q_{22}cos^4\theta \tag{B.13}$$

$$\bar{Q}_{12} = (Q_{11} + Q_{22} - 4Q_{66})sin^2\theta cos^2\theta + Q_{66}(sin^4\theta + cos^4\theta) \tag{B.14}$$

$$\bar{Q}_{66} = (Q_{11} + Q_{22} - 2Q_{12} - 2Q_{66})sin^2\theta cos^2\theta + q_{66}(sin^4\theta + cos^4\theta) \quad \text{(B.15)}$$

$$\bar{Q}_{16} = (Q_{11} - Q_{12} - 2Q_{66})sin\theta cos^3\theta + (Q_{12} - Q_{22} + 2Q_{66})cos\theta sin^3\theta \quad \text{(B.16)}$$

$$\bar{Q}_{26} = (Q_{11} - Q_{12} - 2Q_{66})cos\theta sin^3\theta + (Q_{12} - Q_{22} + 2Q_{66})sin\theta cos^3\theta \quad \text{(B.17)}$$

For instance, in the case of [0/90] layup, [Q], is same for both laminas. If direction 1 is set to 0^o direction and direction 2 is set to 90^o direction, the [Q] for 0^o lamina does not need any transformation in practice. Mathematically, this is setting θ as 0^o. If θ is set to 0^o, [$\bar{Q}$] of 0^o lamina will be identical with the [Q]. On the other hand, although having same [Q] with 0^o lamina, [$\bar{Q}$] of 90^o lamina has to be found by setting θ as 90^o.

When laminate plates are subjected to mechanical or thermal loads, the relation between loads and deformation is defined by classical laminate theory, abbreviated as CLT. The theory takes number of layers, thickness and fiber orientation of each individual layer and the material properties of components into account to create this relationship [6]. CLT is beneficial for calculating stress and strain values at inner layers, apparent laminate properties and details of resulting behavior of laminate such as bending or twisting in respond to loading. Figure B.2a represents a schematic drawing [3] for a laminated structure and Figure B.2b represents an example of exploded view [100].

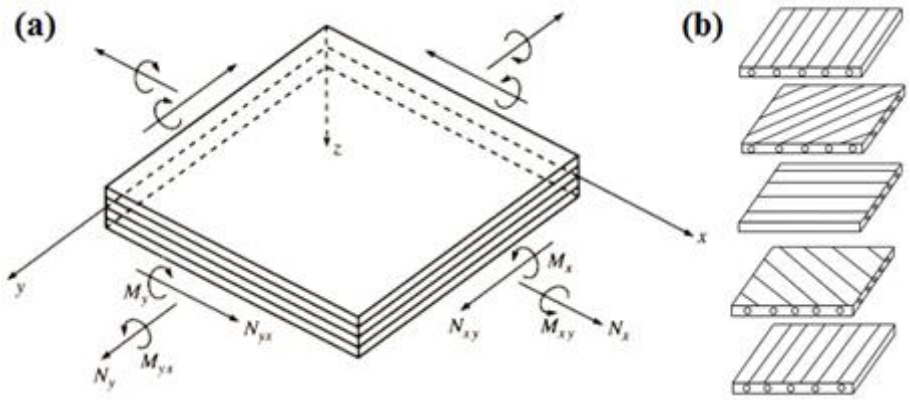

Figure B. 2. (a) The schematic drawing of a laminate [3] and (b) the exploded view of a laminate [100].

The domain of applicability of CLT includes any kind of laminate structure in terms of stacking sequences, layer thicknesses or material characteristics. On the other hand, the theory is accurate and reliable as long as observed region is far enough from the free edges because of the theoretical assumptions such as dimensional infinity.

Just like any other theory, CLT makes assumptions to predict the behavior of laminates such as neglecting interlaminar stresses [3]. These assumptions may influence the theoretical calculations and the results can deviate from the reality. The basic assumptions are listed below [68]:

- The laminate structure consists of arbitrary number of individually orthotropic layers which are bonded to each other perfectly. The principal axes of the layers lie within such planes that are all parallel with each other.

- The thickness of the whole laminate structure is much smaller than other physical dimensions which validates plane stress model.

- Kirchhoff hypothesis is valid. Normals remain straight, unstretched and normal.

- Laminas are bonded to each other perfectly. Therefore, there is no gap between laminates and no relative lamina motion, in other words no slip, occurs.

- Deformation in *x*, *y* and *z* directions are smaller than thickness of the whole laminate.

- Tangential displacements *u* and *v* are linear functions of the *z* coordinate.

- Hooke's Law is obeyed by each layer.

- The thickness of the laminate does not change along the width and length.

- In-plane strains ε_x, ε_y and γ_{xy} are small compared to unity.

- Transverse shear strains, τ_{xz} and τ_{yz} vanish on the plate surfaces.

- Transverse shear strains, γ_{xz} and γ_{yz}, are negligible.

- Transverse normal strain, ε_z is negligible.

- Body forces are not included.

A laminate structure consists of a stack of anisotropic layers which have various orientations relative to laminate axes. To understand the behavior of a laminate structure, macro-mechanical behavior of a single lamina has to be studied in the first place.

For the case of this thesis study, laminate structures are obtained by impregnating dry reinforcement with soon-to-be-solidified liquid matrix material. The production methodology and the procedure are discussed in VIP section. The strength of an individual reinforcing layer comes from the continuous fibers which are held together by solidified matrix. The lamina structure can be illustrated as Figure B.3 [100].

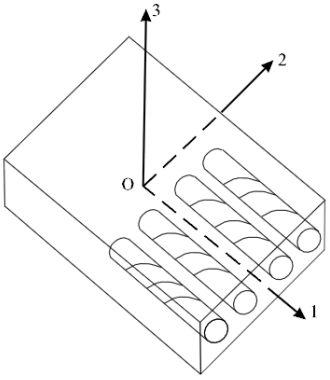

Figure B.3. A schematic drawing of a unidirectional lamina [100].

Since the thickness of lamina is too small compared to its width and length, plane-stress model is valid. Unidirectional isotropic fibers embedded in isotropic matrix create a transversely orthotropic structure of which stress-strain relation is shown in Equation B.18. All the formulas are taken from the references [6] and [100].

$$\begin{Bmatrix} \sigma_1 \\ \sigma_2 \\ \tau_{12} \end{Bmatrix} = \begin{bmatrix} Q_{11} & Q_{12} & 0 \\ Q_{12} & Q_{22} & 0 \\ 0 & 0 & 2Q_{66} \end{bmatrix} \begin{Bmatrix} \varepsilon_{11} \\ \varepsilon_{22} \\ \gamma_{12} \end{Bmatrix} \tag{B.18}$$

The [Q] in Equation B.18 is called reduced stiffness matrix which defines the stress-strain relation of the lamina in terms of modulus of elasticity, shear modulus and Poisson's ratio values in lamina axes. These values depend on the properties of reinforcement and matrix material. The lamina axes do not need to coincide with fiber directions, too. Therefore, the arrangement of components has to be taken into consideration. To avoid confusion, the stiffness matrix [Q] of the lamina where 1 and 2 correspond to fiber direction and transverse direction respectively should be found in the first place and then should be transformed to the desired axes, for instance to the laminate axes. This operation gives transformed reduced stiffness matrix [$\bar{Q}$].

A laminate structure consists of arbitrary numbers of laminas in different orientations. Once reduced stiffness matrices of each lamina are determined relative to the laminate axes, they have to be combined together to define the overall behavior of the laminate structure. A schematic representation of the geometry of an N-layered laminate is shown in Figure B.4 [100].

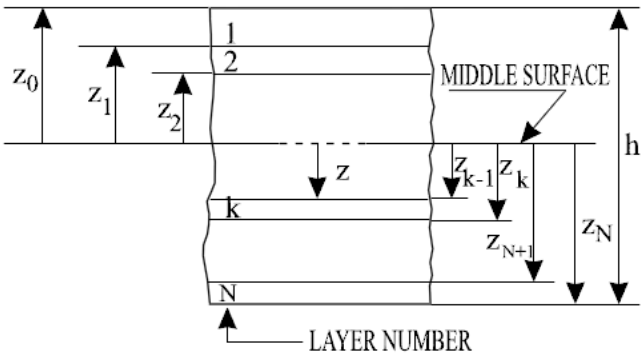

Figure B.4. A schematic representation of the geometry of an N-layered laminate [100].

Equation B.8 defines the behavior of a single lamina. For a laminate structure, this equation has to be satisfied for each layer. If k denotes kth lamina in an N-layered laminate, Equation B.19 holds.

$$\begin{bmatrix}\sigma_x\\ \sigma_y\\ \sigma_{xy}\end{bmatrix}_k = \begin{bmatrix}\bar{Q}_{11} & \bar{Q}_{12} & \bar{Q}_{16}\\ \bar{Q}_{12} & \bar{Q}_{22} & \bar{Q}_{26}\\ \bar{Q}_{16} & \bar{Q}_{61} & \bar{Q}_{66}\end{bmatrix}_k \begin{bmatrix}\varepsilon_x\\ \varepsilon_y\\ \gamma_{xy}\end{bmatrix}_k \tag{B.19}$$

CLT enables defining the stress-strain relation and the mechanical behavior of each lamina in terms of mid-surface strains and curvatures, as formulized in Equation B.20.

$$\begin{bmatrix}\sigma_x\\ \sigma_y\\ \tau_{xy}\end{bmatrix}_k = \begin{bmatrix}\bar{Q}_{11} & \bar{Q}_{12} & \bar{Q}_{16}\\ \bar{Q}_{12} & \bar{Q}_{22} & \bar{Q}_{26}\\ \bar{Q}_{16} & \bar{Q}_{61} & \bar{Q}_{66}\end{bmatrix}_k \left[\begin{bmatrix}\varepsilon_x^0\\ \varepsilon_y^0\\ \gamma_{xy}^0\end{bmatrix} + z\begin{bmatrix}\kappa_x\\ \kappa_y\\ \kappa_z\end{bmatrix}\right] \tag{B.20}$$

In Equation B.20, *z* is the distance from mid-plane. For each layer, the uppermost and the lowermost levels set such a range that when *z* lies in it, the corresponding [*Q*] has to be written in this equation. On the other hand, strain values belong to mid-plane and remain unchanged. κ is a term which defines curvatures of mid-plane.

$$\varepsilon_x^o = \frac{\partial u^o}{\partial x} \tag{B.21}$$

$$\varepsilon_y^o = \frac{\partial v^o}{\partial y} \tag{B.22}$$

$$\gamma_{yx}^o = \frac{\partial u^o}{\partial y} + \frac{\partial v^o}{\partial x} \tag{B.23}$$

$$\kappa_x = -\frac{\partial^2 w}{\partial x^2} \tag{B.24}$$

$$\kappa_x = -\frac{\partial^2 w}{\partial y^2} \tag{B.25}$$

$$\kappa_x = -2\frac{\partial^2 w}{\partial x \partial y} \tag{B.26}$$

If the thickness of a laminate is defined as *h*, it is convenient to define *N*, force per unit length, and *M*, moment per unite length, values illustrated in Figure B.2, with Equations B.27 and B.28, respectively.

$$N_{\alpha\beta} = N_{\beta\alpha} = \int_{-\frac{h}{2}}^{\frac{h}{2}} \sigma_{\alpha\beta} dz \quad \alpha, \beta = 1, 2 \tag{B.27}$$

$$M_{\alpha\beta} = M_{\beta\alpha} = \int_{-\frac{h}{2}}^{\frac{h}{2}} x_3 \sigma_{\alpha\beta} dz \quad \alpha, \beta = 1, 2 \tag{B.28}$$

The integrals can be divided into parts to express the behavior of each layer separately which enables putting Equation B.20 into Equations B.27 and B.28. Therefore, *N* and *M* can be expressed in terms of mid-plane strains, curvatures and transformed stiffness matrices of the structure.

$$[N] = \begin{bmatrix} N_{11} \\ N_{22} \\ N_{12} \end{bmatrix} = \sum_{k=1}^{N} \int_{z_{k-1}}^{z_k} \begin{bmatrix} \sigma_{11} \\ \sigma_{12} \\ \sigma_{22} \end{bmatrix}_k dz \tag{B.29}$$

$$[M] = \begin{bmatrix} M_{11} \\ M_{22} \\ M_{12} \end{bmatrix} = \sum_{k=1}^{N} \int_{z_{k-1}}^{z_k} z \begin{bmatrix} \sigma_{11} \\ \sigma_{12} \\ \sigma_{22} \end{bmatrix}_k dz \tag{B.30}$$

$$[N] = \left\{ \sum_{k=1}^{N} [\bar{Q}]_k \int_{z_{k-1}}^{z_k} dz \right\} [e] + \left\{ \sum_{k=1}^{N} [\bar{Q}]_k \int_{z_{k-1}}^{z_k} z dz \right\} [k] \tag{B.31}$$

$$[M] = \left\{ \sum_{k=1}^{N} [\bar{Q}]_k \int_{z_{k-1}}^{z_k} z dz \right\} [e] + \left\{ \sum_{k=1}^{N} [\bar{Q}]_k \int_{z_{k-1}}^{z_k} z^2 dz \right\} [k] \tag{B.32}$$

For the simplicity, Equations B.31 and B.32 can be written as

$$\begin{Bmatrix} N_x \\ N_y \\ N_{xy} \end{Bmatrix} = \begin{bmatrix} A_{11} & A_{12} & A_{16} \\ A_{12} & A_{22} & A_{26} \\ A_{16} & A_{26} & A_{66} \end{bmatrix} \begin{Bmatrix} \varepsilon_x^0 \\ \varepsilon_y^0 \\ \gamma_{xy}^0 \end{Bmatrix} + \begin{bmatrix} B_{11} & B_{12} & B_{16} \\ B_{12} & B_{22} & B_{26} \\ B_{16} & B_{26} & B_{66} \end{bmatrix} \begin{Bmatrix} \kappa_x \\ \kappa_y \\ \kappa_{xy} \end{Bmatrix} \tag{B.33}$$

$$\begin{Bmatrix} M_x \\ M_y \\ M_{xy} \end{Bmatrix} = \begin{bmatrix} B_{11} & B_{12} & B_{16} \\ B_{12} & B_{22} & B_{26} \\ B_{16} & B_{26} & B_{66} \end{bmatrix} \begin{Bmatrix} \varepsilon_x^0 \\ \varepsilon_y^0 \\ \gamma_{xy}^0 \end{Bmatrix} + \begin{bmatrix} D_{11} & D_{12} & D_{16} \\ D_{12} & D_{22} & D_{26} \\ D_{16} & D_{26} & D_{66} \end{bmatrix} \begin{Bmatrix} \kappa_x \\ \kappa_y \\ \kappa_{xy} \end{Bmatrix} \tag{B.34}$$

where;

$$A_{ij} = \sum_{k=1}^{N} \left(\bar{Q}_{ij}\right)_k (z_k - z_{k-1}) \tag{B.35}$$

$$B_{ij} = \frac{1}{2} \sum_{k=1}^{N} \left(\bar{Q}_{ij}\right)_k (z_k^2 - z_{k-1}^2) \tag{B.36}$$

$$D_{ij} = \frac{1}{3} \sum_{k=1}^{N} \left(\bar{Q}_{ij}\right)_k (z_k^3 - z_{k-1}^3) \tag{B.37}$$

Equations B.33 and B.34 define the mechanical behavior of fiber reinforced laminate composites. Furthermore, [*A*], [*B*] and [*D*] are very useful to predict the behavior. [*A*] is called extensional stiffness matrix, [*B*] is called coupling stiffness matrix and [*D*] is called bending stiffness matrix. The components of these matrices are directly related to fiber orientations and stacking sequences. For instance, in case of mid-plane symmetry, all the components of [*B*] should be equal to zero. Therefore, in the existence of in-plane traction, no coupling effect such as warping is expected. Although in most cases warping or twisting effects are not desired and designers try to avoid having non-null coupling matrix, these effects can also be beneficial for some applications such as propeller blade designs.

For the case of this thesis study, thermal loadings and moisture effects are not taken into account since there is not any significant change at temperature and moisture before and during the tests. For further studies, the effects can be simply added to Equations B.34 and B.35 if there are non-negligible forces caused by temperature or humidity.

APPENDIX C: ACOUSTIC EMISSION MONITORING

If an object is subjected to load, various failure mechanisms can be activated according to the material type and the loading conditions. From the beginning to the final fracture, different failure mechanisms may become activated successively or simultaneously while each failure mechanism leaves different footprints on the part. In addition to those permanent footprints, failure mechanisms may give unique signals while in action [101]. Microstructural changes in the material cause strain-energy release and it results in stress-wave propagation. Therefore, a real-time measuring may help to identify the type of activated failure mechanism by evaluating these signals. Acoustic emission monitoring technique is simply based one evaluation of these signals [73].

Acoustic emission monitoring is a real-time evaluation process of failure mechanism triggered waves. Acoustic emission is a term which is used for the short and fast release of energy in the form of a transient elastic wave [102]. These waves are detected by highly sensitive piezoelectric transducers and converted into electric signals. The electric signals are amplified and sent to the data acquisition software. This method is capable of giving information about failure processes. The software records the time when the transducers detect the stress wave and its intensity. By using multiple transducers, it is also possible to locate the source of the signal, the location of damage in other words. These data can be correlated with a specific type of failure mechanisms.

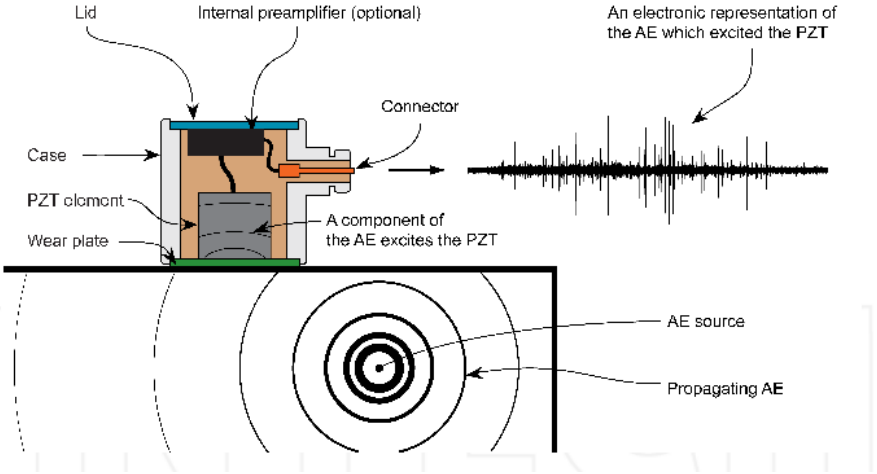

Figure C.1: Acoustic emission monitoring [103].

Figure C.1 illustrates an event for a specimen under tensile loading, detected by acoustic emission real-time measurement [103]. Figure C.2 illustrates a typical waveform that a transducer detects [103].

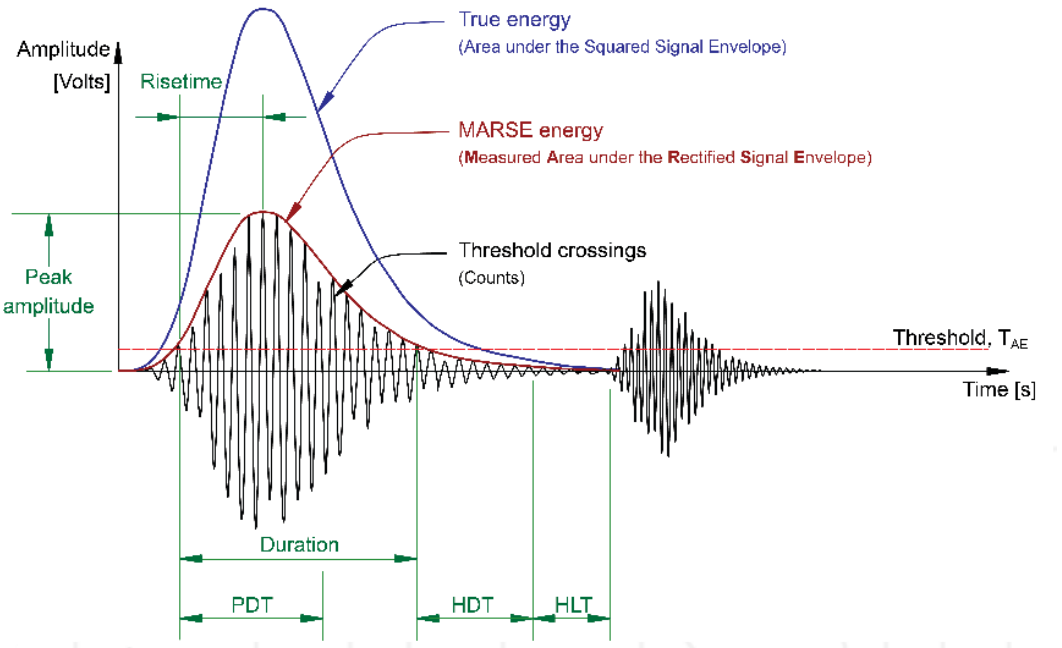

Figure C.2. A typical waveform [103].

Peak Amplitude: It is the maximum voltage measured during detection. It can be transformed into decibel scale. This value is highly important for the evaluation process. A failure mechanism creates such waveforms that peak voltage values usually lie in the same span of the scale.

Threshold: The piezoelectric transducers are highly sensitive devices which can detect background noises easily. Therefore, assigning a threshold for voltage is important to filter a significant amount of noise. However, this value has to be set wisely. Signals with lower amplitudes will not be recorded and if a stress-wave lies below the threshold, it will be missed.

Rise Time: It is the duration between the first threshold crossing of the wave and reaching its peak.

Duration: It is the duration between the first and last threshold crossings of the wave. According to the failure mechanism, the duration of the wave is expected to vary. Therefore, it is accepted as an important value for the evaluation process.

Counts: The total number of threshold crossings between the first and the last ones.

Hit: When the wave is detected by a transducer, the collected data represents a single event which is named as hit.

Peak Definition Time (PDT): This parameter specifies the allowable time to detect and determine the peak amplitude of the hit. In case of setting a too high value, incorrect measurements can be done. PDT should be set as low as possible while considering the fact that too low value may result in wrong peak identification [74].

Hit Definition Time (HDT): For each threshold crossing, the software waits for a period of time to detect another threshold crossing. If it detects another, it keeps recording the data under the same hit. If no crossing detected during this period, the last crossing is set as the end of that hit. This time period is specified by HDT. Any following threshold crossing will be the beginning of another hit. If HDT is set too high, it is possible to record two or more different events under one hit. On the contrary, if it is set too low, the software may divide one event into multiple hits [74].

Hit Lockout Time (HLT): It defines the minimum duration of time required to detect next hit. It simply enables the system to filter reflections and late arriving components of wave. On the other hand, it may prevent the detection of a possible AE event within that period of time.

APPENDIX D: TENSION TEST STANDARD

Figure D.1 is taken from ASTM D3039 test standard and describes part tolerances [70].

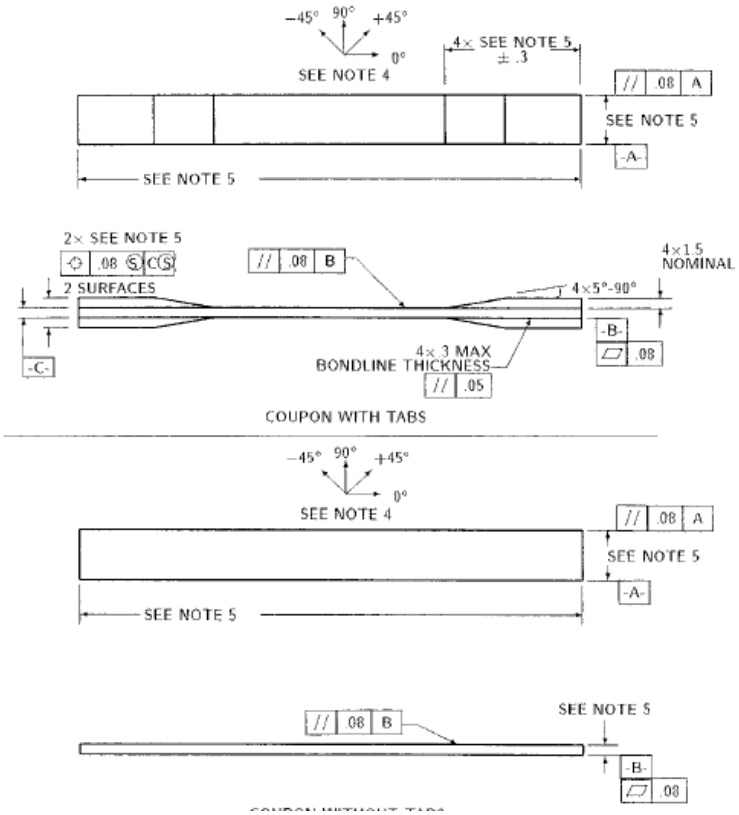

Figure D.1. Dimensional tolerances for tension specimens [70].

Table D.1. Geometrical recommendation [70].

Fiber orientation:	Width [mm]	Overall length [mm]	Thickness [mm]	Tab length [mm]	Tab thickness [mm]	Tab bevel angle
0^o unidirectional	15	250	1	56	1.5	7 or 90^o
90^o unidirectional	25	175	2	25	1.5	90^o
Balanced and symmetric	25	250	2.5	Emery cloth	-	-
Random-discontinuous	25	250	2.5	Emery cloth	-	-

Table D.1 gives geometric recommendations. Table D.2 describes geometrical requirements [70].

Table D.2. Geometrical requirements [70].

Parameter	Requirement
Coupon Requirements:	
Shape	Constant rectangular cross-section
Minimum length	Gripping + 2 times width + gage length
Specimen width	As needed
Specimen width tolerance	±1% of width
Specimen thickness	As needed
Specimen thickness tolerance	±4% of thickness
Specimen flatness	Flat with light finger pressure
Tab Requirements:	
Tab material	As needed
Fiber orientation (composite tabs)	As needed
Tab thickness	As needed
Tab thickness variation between	±1% tab thickness
Tabs:	
Tab bevel angle	5 to 90^{o}, inclusive
Tab step at bevel to specimen	Feathered without damaging specimen

Figure D.2 illustrates the classification of failure modes.

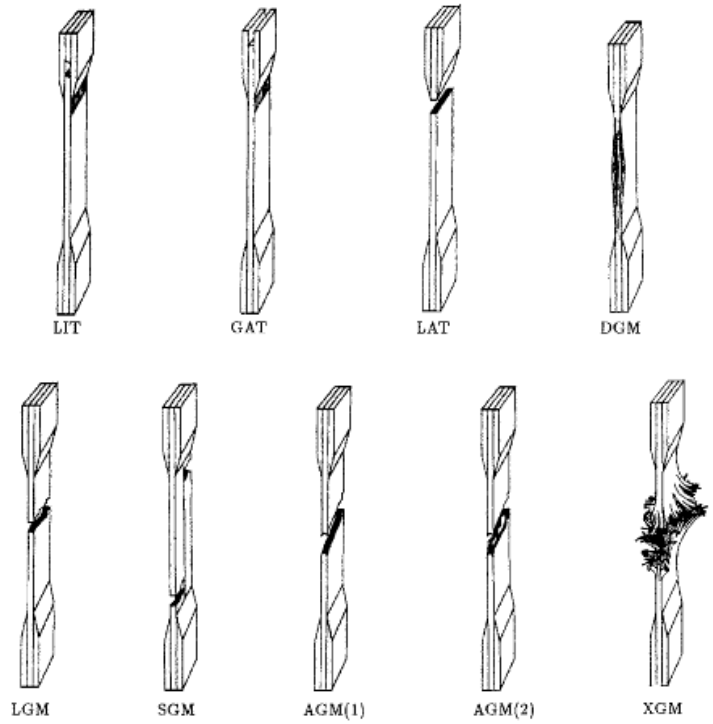

First Character

Failure Type	Code
Angled	A
edge Delamination	D
Grip/tab	G
Lateral	L
Multi-mode	M(xyz)
long. Splitting	S
eXplosive	X
Other	O

Second Character

Failure Area	Code
Inside grip/tab	I
At grip/tab	A
<1W from grip/tab	W
Gage	G
Multiple areas	M
Various	V
Unknown	U

Third Character

Failure Location	Code
Bottom	B
Top	T
Left	L
Right	R
Middle	M
Various	V
Unknown	U

Figure D.2. The classification of failure modes [70].

REFERENCES

1. Hassan, M. Z., *The Low Velocıty Impact Response of Sandwıch Structures*, Ph.D. Thesis, University of Liverpool, 2002.

2. Petras, A., *Design of Sandwich Structures*, Ph.D. Thesis, Cambridge University, 1998.

3. Çalışkan, S., *Mechanical Properties of Non-Crimp Fabric (NCF) Fiberglass Reinforced Composite Materials Manufactured by Using Vacuum Infusion Process*, M.S. Thesis, Boğaziçi University, 2009.

4. Cuadra, J., *Damage Quantification in Fiber Reinforced Polymer Composites Using a Hybrid Non-Destructive Testing Approach*, M.S. Thesis, Drexel University, 2012.

5. Jones, R. M., *Mechanics of Composite Materials, Second Edition*, Taylor & Francis, 1999.

6. Vinson, J. R., *Behavior of Sandwich Structures of Isotropic and Composite Materials*, Technomic, 1999.

7. Buitrago, B. L., C. Santiuste, S. Sánchez-Sáez, E. Barbero, and C. Navarro, "Modeling of Composite Sandwich Structures with Honeycomb Core Subjected to High-Velocity Impact", *Composite Structures*, Vol. 92, pp. 2090-2096, 2010.

8. Sypeck, D. and H. N. G. Wadley, "Cellular Metal Truss Core Sandwich Structures", *Advanced Engineering Materials*, Vol. 4, pp. 759-764, 2002.

9. *Best Practice Guide for Sandwich Structures in Marine Applications*, NewRail, University of Newcastle upon Tyne, 2013.

10. Nallagula, S., *Behavior and Flexure Analysis of Balsa Wood Core Sandwich Composites: Experimental, Analytical and Finite Element Approaches*, M.S. Thesis, University of New Orleans, 2006.

11. Paik, J. K., A. K. Thayamballi, and G. S. Kim, "The Strength Characteristics of Aluminum Honeycomb Sandwich Panels", *Thin-Walled Structures*, Vol. 35, pp. 205-231, 1999.

12. Yan, L. L., B. Han, B. Yu, C. Q. Chen, Q. C. Zhang, and T. J. Lu, "Three-Point Bending of Sandwich Beams with Aluminum Foam-Filled Corrugated Cores", *Materials and Design*, Vol. 60, pp. 510-519, 2014.

13. Navarro, P., "Analytical Modeling of Indentation of Composite Sandwich Beam", *Composite Structures*, Vol. 100, pp. 79-88, 2013.

14. Deshpande, V. S. and N. A. Fleck, "Collapse of Truss Core Sandwich Beams in 3-Point Bending", *International Journal of Solids and Structures*, Vol. 35, pp. 6275-6305, 2001.

15. Fan, H., L. Yang, F. Sun, and D. Fang, "Compression and Bending Performances of Carbon Fiber Reinforced Lattice-Core Sandwich Composites", *Composites: Part A*, Vol. 52, pp. 118-125, 2013.

16. Chung, J. and A. M. Waas, "Compressive Response and Failure of Circular Cell Polycarbonate Honeycombs Under In-Plane Uniaxial Stresses", *Transactions of the ASME*, Vol. 121, pp. 494-502, 1999.

17. Chung, J. and A. M. Waas, "Compressive Response of Circular Cell Polycarbonate Honeycombs Under In-Plane Biaxial Static and Dynamic Loading. Part I: Experiments" *International Journal of Impact Engineering*, Vol. 27, pp. 729-754, 2002.

18. Daniel, I. M., E. E. Gdoutos, J. L. Abot, and K. Wang, "Deformation and Failure of Composite Sandwich Structures", *Journal of Thermoplastic Composite Materials*, Vol. 16, pp. 345-364, 2003.

19. Kim, J. and S. R. Swanson, "Design of Sandwich Structures for Concentrated Loading", *Composite Structures*, Vol. 52, pp. 365-373, 2001.

20. Kim, J. and S. R. Swanson, "Design of Sandwich Structures Under Contact Loading", *Composite Structures*, Vol. 59, pp. 403-413, 2003.

21. Aminanda, Y., B. Castanie, J. J. Barrau, and P. Thevenet, "Experimental Analysis and Modeling of the Crushing of Honeycomb Cores", *Applied Composite Materials*, Vol. 12, pp. 213-227, 2005.

22. Vadakke, V. and L. A. Carlson, "Experimental Investigation of Compression Failure of Sandwich Specimens with Face/Core Debond", *Composites: Part B*, Vol. 35, pp. 583-590, 2004.

23. Othman, A. R. and D. C. Barton, "Failure Initiation and Propagation Characteristics of Honeycomb Sandwich Composites", *Composite Structures*, Vol. 85, pp. 126-138, 2008.

24. Kim, J. and S. R. Swanson, "Failure Modes and Optimization of Sandwich Structures for Load Resistance", *Journal of Composite Materials*, Vol. 37, pp. 649-667, 2003.

25. Lim, T. S., C. S. Lee, and D. G. Lee, "Failure Modes of Foam Core Sandwich Beams Under Static and Impact Loads", *Journal of Composite Materials*, Vol. 38, pp. 1639-1662, 2004.

26. Petras, A. and M. P. F. Sutcliffe, "Indentation Failure Analysis of Sandwich Beams", *Composite Structures*, Vol. 50, pp. 311-318, 2000.

27. Gdoutos, E. E., I. M. Daniel, and K. A. Wang, "Indentation Failure in Composite Sandwich Structures", *Experimental Mechanics*, Vol. 42, pp. 426-431, 2002.

28. Petras, A. and M. P. F. Sutcliffe, "Indentation Resistance of Sandwich Beams", *Composite Structures*, Vol. 46, pp. 413-424, 1999.

29. Giglio, M., A. Manes, and A. Gillioli, "Investigations on Sandwich Core Properties Through an Experimental–Numerical Approach", *Composites: Part B*, Vol. 43, pp. 361-374, 2012.

30. Rathbun, H. J., Z. Wei, M. Y. He, F. W. Zok, A. G. Evans, D. J. Sypeck, and H. N. G. Wadley, "Measurement and Simulation of the Performance of a Lightweight Metallic Sandwich Structure with a Tetrahedral Truss Core", *Transactions of the ASME*, Vol. 71, pp. 368-374, 2004.

31. George, T., V. S. Deshpande, and H. N. G. Wadley, "Mechanical Response of Carbon Fiber Composite Sandwich Panels with Pyramidal Truss Cores", *Composites: Part A*, Vol. 47, pp. 31-40, 2013.

32. Aktay, L., A. F. Johnson, and B. H. Kröplin, "Numerical Modeling of Honeycomb Core Crush Behaviour", *Engineering Fracture Mechanics*, Vol. 75, pp. 2616-2630, 2008.

33. Staal, R. A., G. D. Mallinson, K. Jayaraman, and D. P. W. Horrigan, "Predicting Failure Loads of Undamaged Sandwich Honeycomb Panels Subject to Bending", *Journal of Sandwich Structures and Materials*, Vol. 11, pp. 73-104, 2009.

34. Brooks, R., K. A. Brown, N. A. Warrior, and P. P. Kulandaivel, "Predictive Modeling of the Impact Response of Thermoplastic Composite Sandwich Structures", *Journal of Sandwich Structures and Materials*, Vol. 12, pp. 449-476, 2010.

35. Reyes, G., "Static and Low Velocity Impact Behavior of Composite Sandwich Panels with an Aluminum Foam Core", *Journal of Composite Materials*, Vol. 42, pp. 1659-1670, 2008.

36. Zenkert, D., A. Shipsha, and K. Persson, "Static Indentation and Unloading Response of Sandwich Beams", *Composites: Part B*, Vol. 35, pp. 511-522, 2004.

37. Li, M., L. Wu, L. Ma, B. Wang, and Z. Guan, "Structural Response of All-Composite Pyramidal Truss Core Sandwich Columns in End Compression", *Composite Structures*, Vol. 93, pp. 1964-1972, 2011.

38. Foo, C. C., G. B. Chai, and L. K. Seah, "A Model to Predict Low-Velocity Impact Response and Damage in Sandwich Composites", *Composite Science and Technology*, Vol. 68, pp. 1348-1356, 2008.

39. Ivanez, I., E. Barbero, and S. Sanchez-Saez, "Analytical Study of the Low-Velocity Impact Response of Composite Sandwich Beams", *Composite Structures*, Vol. 111, pp. 459-467, 2014.

40. Crupi, V., G. Epasto, and E. Guglielmino, "Collapse Modes in Aluminium Honeycomb Sandwich Panels Under Bending and Impact Loading", *International Journal of Impact Engineering*, Vol. 43, pp. 6-15, 2012.

41. Manes, A., A. Gilioli, C. Sbarufatti, and M. Giglio, "Experimental and Numerical Investigations of Low Velocity Impact on Sandwich Panels", *Composite Structures*, Vol. 99, pp. 8-18, 2013.

42. Gdoutos, E. E., I. M. Daniel, K. A. Wang, and J. L. Abot, "Nonlinear Behavior of Composite Sandwich Beams in Three-Point Bending", *Experimental Mechanics*, Vol. 41, pp. 182-189, 2001.

43. Giglio, M., A. Gilioli, and A. Manes, "Numerical Investigation of a Three Point Bending Test on Sandwich Panels with Aluminum Skins and Nomex™ Honeycomb Core", *Computational Material Science*, Vol. 56, pp. 69-78, 2012.

44. Ivanez, I. and S. Sanchez-Saez, "Numerical Modelling of the Low-Velocity Impact Response of Composite Sandwich Beams with Honeycomb Core", *Composite Structures*, Vol. 106, pp. 716-723, 2013.

45. Aktay, L., A. F. Johnson, and M. Holzapfel, "Prediction of Impact Damage on Sandwich Composite Panels", *Computational Material Science*, Vol. 32, pp. 252-260, 2005.

46. Romanoff, J. and P. Varsta, "Bending Response of Web-Core Sandwich Plates", *Composite Structures*, Vol. 81, pp. 292-302, 2007.

47. Østergaard, R. C., "Buckling Driven Debonding in Sandwich Columns", *International Journal of Solids and Structures*, Vol. 45, pp. 1264-1282, 2008.

48. Frostig, Y., "Buckling of Sandwich Panels With a Flexible Core-High-Order Theory", *International Journal of Solids and Structures*, Vol. 35, pp. 183-204, 1998.

49. Qiao, P., and M. Yang, "Impact Analysis of Fiber Reinforced Polymer Honeycomb Composite Sandwich Beams", *Composites: Part B*, Vol. 38, pp. 739-750, 2007.

50. Lee, S. M. and T. K. Tsotsis, "Indentation Failure Behavior of Honeycomb Sandwich Panels", *Composites Science and Technology*, Vol. 60, pp. 1147-1159, 2000.

51. Lin, T. C., T. J. Chen, and J. S. Huang, "In-Plane Elastic Constants and Strengths of Circular Cell Honeycombs", *Composites Science and Technology*, Vol. 72, pp. 1380-1386, 2012.

52. Caner, C. F. and Z. P. Bazant, "Size Effect on Strength of Laminate-Foam Sandwich Plates: Finite Element Analysis with Interface Fracture", *Composites: Part B*, Vol. 40, pp. 337-348, 2009.

53. Petras, A. and M. P. F. Sutcliffe, "Failure Mode Maps for Honeycomb Sandwich Panels", *Composite Structures*, Vol. 44, pp. 237-252, 1999.

54. Wadee, M. A. and A. Blackmore, "Delamination from Localized Instabilities in Compression Sandwich Panels", *Journal of the Mechanics and Physics of Solids*, Vol. 49, pp. 1281-1299, 2001.

55. Guinta, G., A. Catapano, and S. Belouettar, "Failure Indentation Analysis of Composite Sandwich Plates via Hierarchical Models", *Journal of Sandwich Structures and Materials*, Vol. 15, pp. 45-70, 2012.

56. Gdoutos, E. E. and I. M. Daniel, "Failure Modes of Composite Sandwich Beams", *Journal of Theoretical and Applied Mechanics*, Vol. 35, pp. 105-118, 2008.

57. Wicks, N. and J. W. Hutchinson, "Performance of Sandwich Plates with Truss Cores", *Mechanics of Materials*, Vol. 36, pp. 739-751, 2004.

58. Galletti, G. G., C. Vinquist, and O. S. Es-Said, "Theoretical Design and Analysis of a Honeycomb Panel Sandwich Structure Loaded in Pure Bending", *Engineering Failure Analysis*, Vol. 15, pp. 555-562, 2008.

59. Rejab, M. R. M. and W. J. Cantwell, "The Mechanical Behavior of Corrugated-Core Sandwich Panels", *Composites: Part B*, Vol. 47, pp. 267-277, 2013.

60. Anderson, T. L., *Fracture Mechanics Fundamentals and Applications, Third Edition*, Taylor & Francis, 2005.

61. Summerscales, J., "Composites Design and Manufacture: Strength, Failure Mechanisms, Fractography, Failure Criteria, Fracture Mechanics", 2014, http://www.tech.plym.ac.uk/sme/MATS324/MATS324A4%20fracture.htm, [Accessed July 2014].

62. Brauer, D. S., C. Russel, S. Vogt, J. Weisser, and M. Schnabelrauch, "Degradable Phosphate Glass Fiber Reinforced Polymer Matrices: Mechanical Properties and Cell Response", *Journal of Materials Science: Materials in Medicine*, Vol. 19, pp. 121-127, 2008.

63. Budiansky, B. and N. Fleck, "Compressive Kinking of Fiber Composites: A Topical Review", *Applied Mechanics Reviews*, Vol. 47, pp. 246-250, 1994.

64. Karbhari, V., *Non-Destructive Evaluation (NDE) of Polymer Matrix Composites, First Edition,* Woodhead Publishing, 2013.

65. Tsai, S. W., D. Gay, and S. V. Hoa, *Composite Materials Design and Applications*, Crc Press, 2003.

66. Choo, V. K. S., *Fundamentals of Composite Materials*, Knowen Academic Press, Inc. Dover, Delaware, 1990.

67. Tsai, S. W., "Strength Theories of Filamentary Structures", *in Fundamental Aspects of Fiber Reinforced Plastic Composites*, Conference Proceedings, Dayton, Ohio, 1966.

68. Gibson, R. F., *Principles of Composite Materials Mechanics*, McGraw-Hill, Inc., 1994.

69. FibreGlast® Developments Corporation, "Vacuum Infusion - The Equipment and Process of Resin Infusion", http://cdn.fibreglast.com/downloads/vacuuminfusion.pdf, [Accessed February 2014].

70. *Standard Test Method for Tensile Properties of Polymer Matrix Composite Materials*, ASTM International.

71. HEXION® Specialty Chemicals, "Laminating Resin MGS® L 285 Hardeners MGS® 285, 286, 287 Technical Information", 2006, http://www.metyx.com/Uploads/GenelDosya/301201393220901.pdf, [Accessed September 2013].

72. Bohse, J., "Damage Analysis of Polymer Matrix Composites by Acoustic Emission Testing", *Proceedings of the 26th European Conference on Acoustic Emission Testing*, 2004.

73. Aramugam, V., S. B. Kumar, C. Santulli, and A. J. Stanley, "Effect of Fiber Orientation in Uni-Directional Glass Epoxy Laminate Using Acoustic Emission Monitoring", *Acta Metallurgica Sinica*, Vol. 24, pp. 351-364, 2011

74. Barsoum, F. F., J. Suleman, A. Korcak, and E. V. K. Hill, "Acoustic Emission Monitoring and Fatigue Life Prediction in Axially Loaded Notched Steel Specimens", *Journal of Acoustic Emission*, Vol. 27, pp. 40-63, 2009.

75. Masmoudi, S., A. E. Mahi, S. Turki, and R. E. Guerjouma, "Mechanical Behavior and Health Monitoring by Acoustic Emission of Unidirectional and Cross-Ply Laminates Integrated by Piezoelectric Implant", *Applied Acoustics*, Vol. 86, pp. 118-125, 2014.

76. *FFT Tutorial*, University of Rhode Island Department of Electrical and Computer Engineering, March 2014.

77. Wadim, J. R., *Acoustic Emission Applications*, Dunegan Endevco, San Juan Capistrano, CA, 1978.

78. Gong, X. L., A. Laksimi, and M. L. Benzeghagh, "Nouvelle Approche de L'émission Acoustique et son Application à L'identification des Mécanismes D'endommagement dans les Matériaux Composites", *Revue Des Composites et des Matériaux Avancés*, Vol. 8, pp. 179-205, 1998.

79. Segard, E., S. Benmedakhene, A. Laksimi, and D. Lai, "Damage Analysis and the Fibre-Matrix Effect in Polypropylene Reinforced by Short Glass Fibres Above Glass Transition Temperature", *Composite Structures*, Vol. 60, pp. 67-72, 2003.

80. Mechraoui, S. E., A. Laksimi, and S. Benmedakhene, "Reliability of Damage Mechanism Localisation by Acoustic Emission on Glass/Epoxy Composite Material Plate", *Composite Structures*, Vol. 94, pp. 1483-1494, 2012.

81. Aramugam, V., K. C. Suresh, C. Santulli, F. Sarasini, and S. A. Joseph, "A Global Method for the Identification of Failure Modes in Fiberglass Using Acoustic Emission", *Journal of Testing and Evaluation*, Vol. 39, No. 5.

82. Bussiba, A., M. Kupiec, S. Ifergane, R. Piat, and T. Böhlke, “Damage Evolution and Fracture Events Sequence in Various Composites by Acoustic Emission Technique”, *Composites Science and Technology*, Vol. 68, pp. 1144-1145, 2008.

83. Asokan, R., V. Aramugam, C. Santulli, S. B. Kumar, and A. J. Stanley, “Investigation of the Strength of the Failure Modes in GFRP Laminates Using Acoustic Emission Monitoring”, *Journal of Reinforced Plastics and Composites*, Vol. 31, pp. 1226-1235, 2012.

84. Groot, P. J., P. A. M. Wijnen, and R. B. F. Janssen, “Real-Time Frequency Determination of Acoustic Emission for Different Fracture Mechanisms in Carbon/Epoxy Composites”, *Composites Science and Technology,* Vol. 55, pp. 405-412, 1995.

85. Fotouhi, M., P. B. Dastjerdi, and M. Ahmadi, “Acoustic Emission Based Method to Characterize Glass/Epoxy Composite Damages During 3-Point Bending Test”, *International Journal of Material Science,* Vol. 4, Issue 1, pp. 22-30, 2014.

86. Aramugam, V., S. Sajith, and A. J. Stanley, “Acoustic Emission Characterization of Failure Modes in GFRP Laminates Under Mode I Delamination”, *Journal of Nondestructive Evaluation*, Vol. 30, Issue 3, pp. 213-219, 2011.

87. INSTRON®, “8801 Servohydraulic Fatigue Testing System”, www.instron.com, [Accessed June 2014].

88. Reifsnider, K. L., E. G. Henneke, W. W. Stinchcomb, and J. C. Duke, “Damage Mechanics and NDE of Composite Laminates”, *Mechanics of Composite Materials: Recent Advances*, pp. 399-420, 1983.

89. Makris, A., C. Ramault, D. Van Hemelrijck, E. Lamkanfi, and W. Van Paepegem, "Biaxial Failure Envelopes for Glass Fibre Reinforced Composite Laminates", *Proceedings of the SEM Annual Conference*, 2009.

90. Mashayekhi, M., “Element Selection Criteria”, http://mashayekhi.iut.ac.ir/sites/mashayekhi.iut.ac.ir/files/u32/presentation10.pdf, [Accessed May 2014].

91. Nidaplast® Honeycomb Cores, “Nida 8/GB Technical Data”, 2003, http://www.boatcraftnsw.com.au/nidaplast/Nidaplast%208%20gb,%20v3.pdf, [Accessed July 2014].

92. CEL Components, “Polypropylene Honeycomb Core PP8.80 / PP8-80T30 / PP8-80T30F75”, http://www.honeycombpanels.eu/img_ins/schede/polipropileneP880uk.pdf, [Accessed July 2014].

93. Nidaplast® Honeycomb Cores, “Nidaplast® 8 Range”, http://www.impag.co.uk/pdfs/nidaplast.pdf, [Accessed July 2014].

94. ThermHex® Honeycomb Cores, “The New Generation of Lightweight Core Materials”, 2013, http://www.thermhex.nl/en/images/ThermHex_Folder_engl_E2013_copy.pdf, [Accessed July 2014].

95. Giglio, M., A. Gilioli, and A. Manes, “A Numerical Investigation on Significant Parameters Influencing the Flatwise Compressive Behaviour of a Nomex™ Honeycomb”, *Procedia Engineering*, Vol. 10, pp. 3441-3446, 2011.

96. Leggett, M., *Vacuum Resin Infusion – A Brief History*, Oceania Composites Engineering,

97. Song, X., *Vacuum Assisted Resin Transfer Molding (VARTM): Model Development and Verification*, Ph.D. Thesis, Virginia Polytechnic Institute and State University, 2003.

98. Anonymous, “Laminators Take Cover”, *Reinforced Plastics*, Vol. 47, Issue 9, pp. 47-49, 2003.

99. Correira, N. C., F. Robitaille, A. C. Long, C. D. Rudd, P. Simacek, and S. G. Advani, "Analysis of the Vacuum Infusion Moulding Process: I. Analytical Formulation", *Composites: Part A*, Vol. 36, pp. 1645-1656, 2005.

100. Cristescu, N. D., *Mechanics of Elastic Composites*, Chapman and Hall/CRC, 2003.

101. Gutkin, R., C. J. Green, S. Vangrattanachai, S. T. Pinho, P. Robinson, and P. T. Curtis, "On Acoustic Emission for Failure Investigation in CFRP: Pattern Recognition and Peak Frequency Analyses", *Mechanical Systems and Signal Processing*, Vol. 25, pp. 1393-1407, 2011.

102. Vallen, H., "AE Testing, Fundamentals, Equipment, Applications", *E-Journal of Nondestructive Testing*, Vol. 7, No. 9, 2002.

103. Unnþórsson, R., "Hit Detection and Determination in AE Bursts, Acoustic Emission - Research and Applications", 2013, http://www.intechopen.com/books/acousticemission-research-and-applications/hit-detection-and-determination-in-ae-burst, [Accessed April 2014].